Università degli Studi di Catania
Scuola Superiore di Catania

International Ph.D. in
Nuclear and Particle Astrophysics
XXIV cycle

Statistical methods for the search of high energy neutrinos from galactic sources in KM3NeT and ANTARES telescopes

Ph.D. candidate:
Valentina Giordano

Supervisor: Prof. Antonio Insolia

Ph.D. coordinator: Prof. Umberto Lombardo

A long time ago in a galaxy far,
far away. . .

Star Wars - A New Hope (1977)
directed by George Lucas

A Gianmarco, Enrico e Teresa

Contents

Introduction **v**

1 Physics of cosmic rays and γ astronomy **1**
1.1 Cosmic rays . . . 2
1.1.1 Spectrum of cosmic rays . . . 2
1.1.2 Shock acceleration . . . 5
1.2 Cosmic photons and γ-ray astronomy . . . 7
1.2.1 Leptonic process . . . 9
1.2.2 Hadronic process . . . 10
1.3 Neutrino astronomy . . . 13
1.3.1 Extra-galactic sources . . . 14
1.3.2 Galactic sources . . . 19
1.4 Galactic sources of interest . . . 22
1.4.1 Super Nova Remnant RXJ1713.3946 . . . 23
1.4.2 The Fermi Bubbles . . . 26

2 High Energy neutrino detection **31**
2.1 Physics of neutrinos . . . 31
2.1.1 The "solar neutrino problem" . . . 32
2.1.2 Oscillations of neutrinos . . . 34
2.2 Detection principle . . . 37
2.2.1 Neutral current reactions . . . 38
2.2.2 Charged current reactions . . . 38
2.3 Muon neutrinos detection . . . 44
2.3.1 Cherenkov radiation . . . 45

2.3.2 Physical background . . . 46
2.3.3 Environmental background in the telescope . . . 47
2.3.4 Light transmission properties . . . 49
2.4 Cherenkov high energy neutrino detectors . . . 50
2.4.1 Icecube and AMANDA . . . 51
2.4.2 NEMO . . . 52
2.4.3 The ANTARES neutrino telescope . . . 52
2.4.4 Other detection techniques . . . 54

3 The KM3NeT high energy neutrino telescope 56
3.1 Optical modules . . . 59
3.2 Data acquisition system (DAQ) . . . 61
3.2.1 Trigger . . . 61
3.3 Calibration . . . 62
3.4 Positioning system . . . 64

4 Monte Carlo simulation and analysis tools 65
4.1 The detector geometry . . . 66
4.2 Generation of neutrino events . . . 67
4.2.1 Neutrino fluxes and event weights . . . 69
4.3 Generation of atmospheric muons . . . 72
4.4 Propagation of particles and light production . . . 74
4.4.1 Photon table generation . . . 75
4.4.2 Optical Module hit distributions . . . 76
4.4.3 `KM3MC` . . . 77
4.5 Generation of optical background: `MODK40` . . . 78
4.6 Track reconstruction: `RECO` . . . 79
4.6.1 Pre-selection of hits . . . 80
4.6.2 Prefit . . . 81
4.6.3 PDF . . . 82
4.6.4 M-estimator . . . 83
4.6.5 Maximum likelihood fit with original PDF . . . 84
4.6.6 Maximum likelihood with improved PDF . . . 84

5 Statistical methods in the search of cosmic neutrino sources 87
5.1 Effective areas . . . 87
5.1.1 Effective volumes . . . 88

5.1.2 Neutrino effective areas . . . 89
5.1.3 Muon effective areas . . . 89
5.2 Sensitivity studies . . . 90
5.2.1 Binned Methods . . . 91
5.2.2 Model Rejection Factor (MRF) . . . 92
5.2.3 Model Discovery Potential (MDP) . . . 93
5.2.4 MDP and MRF optimization . . . 95
5.3 Unbinned methods for the discovery of cosmic neutrino sources . . . 97
5.3.1 Monte Carlo samples . . . 98
5.3.2 The unbinned algorithm . . . 102

6 Fixed point-like and extended sources searches 107
6.1 Point-like sources analysed with KM3NeT telescope . . . 108
6.1.1 Likelihood-ratio distributions . . . 108
6.1.2 Discovery Potential . . . 110
6.1.3 Analysis for a point-like source at $\delta = -60°$ . . . 112
6.1.4 Analysis for RXJ1713.3946 . . . 114
6.2 The Fermi Bubbles analysed with the ANTARES telescope . . . 116
6.2.1 Selection of Runs . . . 118
6.2.2 Data-MonteCarlo comparison . . . 120
6.2.3 Results . . . 123
6.2.4 Unbinned calculations . . . 124

7 Conclusions 129

Bibliography 132

Introduction

The understanding of the violent side of the Universe is a major challenge in astroparticle physics. Indeed observations of the diffuse photon flux at the Earth indicate that the energy content in X and gamma-rays, produced by violent phenomena, is comparable to that associated low energy phenomena. However the comprehension of the High Energy (HE) Universe is very limited.
The messengers of the high energy Universe are hadrons (protons and heavier nuclei), gamma rays and neutrinos. Moreover, since some astrophysical objects such as Super Novae and Gamma Ray Bursts are connected to the acceleration of huge macroscopic masses, gravitational waves are also expected to play an important role. Each of these probes reveals peculiar behaviours of cosmic sources but only an astronomy based on observation of astrophysical objects with different techniques will allow to get a deeper insight on the HE Universe and on the mechanisms responsible for the production of high energy particles. In particular neutrinos interacts only weakly with matter with respect to protons and gammas, and they can travel through the Universe without being deflected or absorbed. However, large detectors are needed to compensate the low interaction cross section; this is also the reason why they have not been used in astronomy until very recently.
In 1960, Markov proposed a possible way to detect high-energy neutrinos using huge volumes of natural material such as ice o deep seawater. Muon neutrinos produced in astrophysical objects would interact via charged current with one of the nucleons of the surrounding medium. In the range of energies up to 100 GeV the detection of muon neutrinos is the golden channel for neutrino astronomy for an high-scale neutrino detector . Neutrino charged current interaction would induce a muon

that emits Cherenkov photons in the ice or water, to be detected by a lattice of photomultipliers installed in the medium. At energies above TeV, muons resulting from charged current interactions can travel kilometres and are almost co-linear with the parent neutrinos. Given the low cross section of the νN interaction and the predicted astrophysical neutrino fluxes, the typical size of the detector should be of km^3.
Currently the world's largest neutrino detector is Icecube [1], encompassing a cubic kilometer of ice and located in the South Pole. IceCube searches for neutrinos from the most violent astrophysical sources: events like exploding stars, gamma ray bursts, and cataclysmic phenomena involving black holes and neutron stars. In the northern hemisphere, the ANTARES [2] high-energy neutrino telescope is an array of photomultipliers tubes distributed over 12 lines installed in the Mediterranean Sea at a depth of about 2500 meters, 40 km off the coast of Toulon (France). The detector has been operated in partial configurations since March 2006 and was completed in May 2008. The main goal of the experiment is the search for high-energy neutrinos from astrophysical sources. A neutrino telescope in the northern hemisphere includes the Galactic Centre in its field of view and is complementary to the IceCube Antarctic telescope. It is also meant to be a first step towards a kilometer-cube neutrino observatory in the Northern Hemisphere. Concerning this point, the KM3NeT consortium is aiming at the construction of a cubic-kilometre-scale neutrino telescope with an integrated platform for Earth and Deep sea sciences [3].
KM3NeT profits from the experience accumulated within the three pilot neutrino telescope projects operating in the Mediterranean Sea (ANTARES, NEMO, and NESTOR [4]), whose members participate in the consortium together with members from other institutions, including ocean science laboratories. The NEMO collaboration has lead since several years an activity of research and deployment for a Cherenkov neutrino telescope located at a depth of about 3500 metres , 85 km off the coast of Capo Passero (Sicily,Italy) [67].
In this thesis, the results of statistical methods for the search of very-high energy cosmic neutrinos from point-like and extended sources will be presented.
In particular two galactic gamma-ray sources that are good candidates as high energy neutrino sources will be analysed: the Super Nova Rem-

nant RXJ1713-3946 and the Fermi Bubbles.
RXJ1713.7-3946, was discovered in soft X-rays in 1996 and in 2003 HESS provided a unique gamma-ray image of the remnants on arcminute scales up to several tens of TeV.
Furthermore, the discovery of the Fermi Bubbles from an analysis of the Fermi-LAT data of 2010 is opening new interesting discussions about the origin of these structures of the Milky Way.
Neutrino events are simulated through the simulation code developed by the ANTARES collaboration and modified for the KM3NeT detector. The analysis on the performances of the detector has been performed with two statistical methods : the binned and the unbinned search methods. A comparison between these two methods will be presented.

The thesis is organized as follows:

- In chapter 1, the physics of cosmic rays and the gamma astronomy will be presented. A special section will be dedicated only to the neutrino astronomy focusing on the Fermi Bubbles and to the RXJ1713.7-3946, since these two sources will be analysed in the last chapter.
- In chapter 2 the main features of neutrino physics is shortly reported. The interaction of neutrinos with matter and the techniques for the detection of astrophysical neutrinos with energies between hundreds of GeV up to several EeV will be presented.
- Chapter 3 is dedicated to the description of the KM3NeT detector.
- In chapter 4 the simulation code used is presented with all of its programs constituent.
- In chapter 5 the two main statistical methods applied to the search of cosmic neutrino sources will be explained.
- In chapter 6 the main results obtained from a statistical analysis of the sources analysed are reported and compared.

Chapter 1

Physics of cosmic rays and γ astronomy

In recent years many discoveries on high energy Cosmic Rays (CRs) have been made, but many open questions still remain. This is one of the motivation for the attempts to detect cosmic neutrinos. These particles can reach very high energies so it's suggest that it could exist an astrophysical object that can accelerate them up to high energies. However, the sources of the CRs cannot be directly identified, because their directions are randomized by their inter-galactic magnetic fields. One way of identifying CR sources is via detection of neutrinos produced by interaction of CR in or around the source.
Section 1.1 contains a brief discussion of CRs and the mechanism by which they may be accelerated. This is relevant because the question of the CR origin is one of the main motivations for the search for point sources of high energy cosmic neutrinos, but also because the CR spectra at the source are an ingredient for models of neutrino production.
In section 1.2 the gamma-ray astronomy is presented ad one of the points of relevance for the next field of research, the neutrino astronomy ; treated in section 1.3 focusing on candidate neutrino sources. Finally the last section 1.4 will treat two of the most important candidate of neutrino sources in our galaxy; these will be part of the analysis in the last chapter. A more extensive discussion of CRs and neutrino production can be found in references [5] and [6].

1.1 Cosmic rays

Cosmic rays (CR) were discovered in 1912 by V. Hess [7]. Using three golden electrometers he measured the amount of radiation up to an altitude of 5300 meters in a free balloon flight. He found that the level of radiation increased with altitude, showing that some kind of radiation enters the atmosphere from above. This contradicts the hypothesis that the flux of ionizing particles arises from Earth's radioactive rocks exclusively. He gave the name of "cosmic radiation" to this phenomenon. Hess received the Nobel Prize in Physics in 1936 for his discovery. Depending on energies of cosmic rays several detection techniques have been developed:

- $10^9 eV < E < 10^{12} eV$ with direct measurement through atmospheric balloon or satellites, that also provide the most relevant information about the composition of CRs.
- $10^{12} eV < E < 10^{17} eV$ with direct measurement (energy limited) through array detectors: studies on extensive air showers (EAS) that arrive at the Earth.
- $10^{17} eV < E < 10^{21} eV$ with indirect measurement through giant array detectors.

Above energies of $\sim 10^{14}$ eV, due to the low flux of cosmic rays, measurements are accessible only from big infrastructures located on the ground. Detector arrays detect showers of secondary particles created by interaction of primary CRs and distributed in a large area.

1.1.1 Spectrum of cosmic rays

The measured flux of high energy protons and nuclei impinging on the Earth's atmosphere is shown in figure 1.1. The energies of the particles span many orders of magnitude, up to energies above 10^{20} eV. The differential flux can be described by a power law:

$$\frac{dN}{dE} \propto E^{-\gamma} \tag{1.1}$$

where γ is the spectral index. The measured value of changes from about 2.7 to about 3.0 at an energy of roughly 3×10^{15} eV. This feature is

known as the "knee" of the spectrum. At energies of about 3×10^{18} eV, the spectral index changes again to a value of about 2.7. This feature is known as the "ankle". Almost 90% of all the incoming cosmic

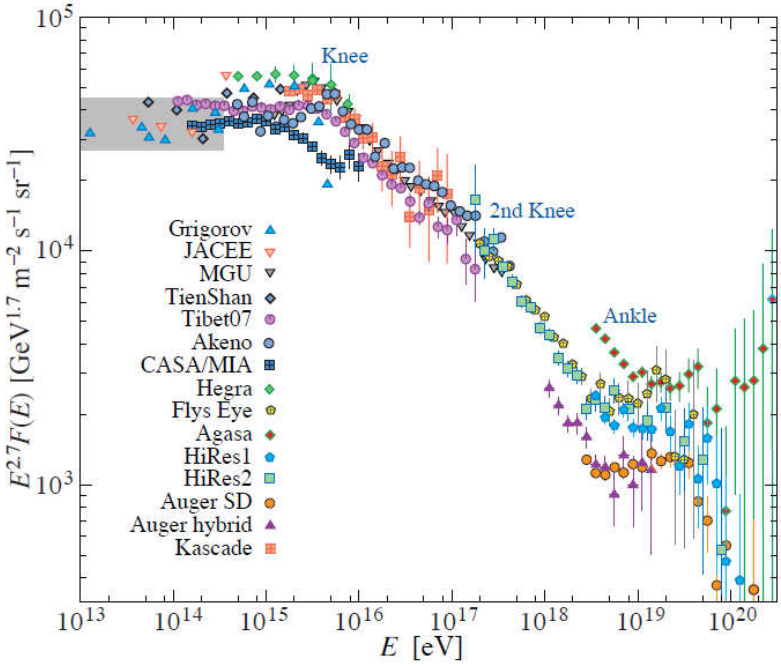

Figure 1.1: The all-particle spectrum from air shower measurements. The shaded area shows the range of the the direct cosmic ray spectrum measurements.

ray particles are simple protons, with nearly 10% being helium nuclei (alpha particles), and slightly under 1% are heavier elements, electrons (beta particles), or gamma ray photons.
The arrival direction at the Earth of CR is randomised by the Galactic ($B \simeq 3\mu G$) and intergalactic ($\sim$ nG) magnetic fields. The gyro-radius of a nucleus having charge Z and energy E (in eV) is:

$$R_{giro}(E) = \frac{E}{ZB_{galactic}} \simeq 3 \times 10^{16} \frac{E}{Z} [pc] \tag{1.2}$$

R_{gyro} is comparable with the thickness of the Galactic disk (about 200 *pc*) for a proton with $E \simeq 10^{18}$eV. This means that pinpointing of charged CR sources is possible only with protons having $E > 10^{19}$ eV.
Beyond 3×10^{15} eV, the spectral index changes and becomes more hard. The knee of the CR spectrum is still an open question and different models have been proposed to explain this particular shape [10].

Some models expect a maximum energy for the CR, due to the iterative scattering processes involved in the acceleration sites. The maximum energy depends on the nucleus charge Ze, leading the prediction of a different cutoff for every nucleus type. As a consequence, CR composition is expected to be proton-rich before the knee, and iron-rich after. After the ankle, where is a flattening in the spectrum, it is generally assumed that CRs have extragalactic origin. No galactic source class is energetic enough for the production of particles at such high energies, and the gyro-radius of the particles becomes too large and they escape from the galaxy already at lower energies. In addition, at energies of about 10^{20} eV , the particle diffusion is low compared to the travelling path through the Galaxy [11]. The observed particles point in this case back to their original source. The observed events are isotropically distributed, which is only possible for travelling lengths longer than the diameter of the galaxy. In figure 1.2 (is the so called "Hillas plot") several dimensions of candidate sources of acceleration of CRs are depicted in function of their magnetic fields.
Above 6×10^{19} eV the CR flux is expected to be suppressed by the Greisen-Zatsepin- Kuzmin (GZK) effect [12]. The cut-off in the flux is caused by the photo-interaction of protons with the 2.7 K Cosmic Microwave Background radiation (CMBR). Indeed the cross-section of the proton photo-pion interaction $p + \gamma_{CMBR} \longrightarrow N + \pi$ is about $100 \mu barn$ and the average CMBR density is $n_{CMBR} \simeq 400 photons/cm^3$, the absorption length of high energetic protons in the Universe is roughly

$$L_{p,CMBR} \simeq (\sigma_{p\gamma} \times n_{CMBR})^{-1} < 50 Mpc \tag{1.3}$$

well shorter than the distance between cosmological sources and Earth. The observation of a suppression in the ultra high energy region of the CR energy spectrum is confirmed both by HIRES [13] and Auger [14], while in the AGASA data [15], now under revision, the suppression was not observed. However, in the most recent analysis of the Auger data, including all the events collected up to now, the interpretation of the Ultra High Energy Cosmic Ray spectrum in terms of GZK effect can be established.

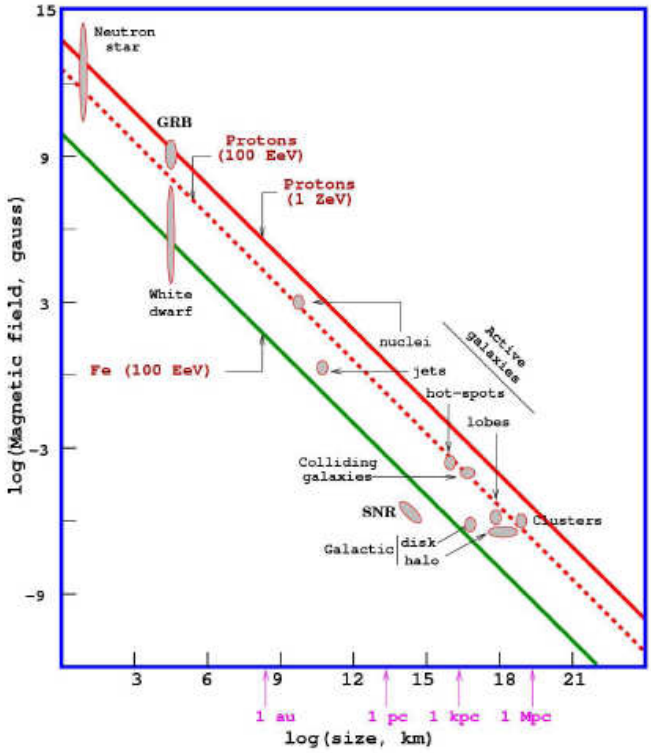

Figure 1.2: Proposed sites for cosmic ray acceleration related to their likely dimension. The lines shows the magnetic field strength vs. gyroradii for protons (dashed red) and iron (green) for a limit of 100 EeV CR containment in the sources. The solid red is the magnetic field strength vs. gyroradii for protons for a limit of ZeV.

1.1.2 Shock acceleration

The mechanism most likely responsible for accelerating particles up to observed CR energies is known as "shock acceleration" or "first order Fermi acceleration" (see [5]). The "Fermi mechanism" can be a plausible hypothesis for the acceleration of CRs [8, 9]. This process occurs when two plasmas collide, forming a shock at the boundary. In this model, particles are magnetically confined to the source and they are elastically scattered by magnetic irregularities that are frozen into the plasma. On both sides of the shock front, the scattering will result in an isotropic velocity distribution of the particle with respect to the local medium.

Figure 1.3 depicts the situation in the 'lab' frame, where the shock propagates through the stationary interstellar medium (ISM) with velocity

V_s. The velocity u of the matter behind the shock is related to the shock velocity by hydrodynamics. In case the shock speed is much larger

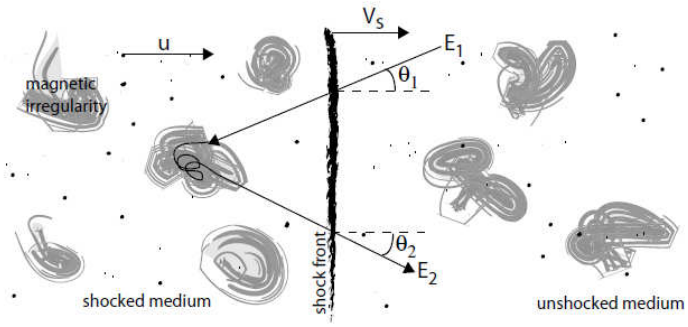

Figure 1.3: Shock acceleration mechanism. A particle moves from the unshocked medium, which is at rest in this picture, into the shocked medium, where it elastically scatters on the irregular magnetic fields. When returning back to the unshocked medium, the particle has gained a fraction of its original energy.

than the speed of sound in the plasma, the relation is [16]:

$$u = \frac{3}{4} V_s \tag{1.4}$$

When a relativistic particle with energy E_1 crosses the shock front from the unshocked to the shocked medium at an angle θ_1, its energy in the rest frame of the shocked medium is $E_1' = \Gamma E_1 (1 + \frac{u}{c} \cos\theta_1)$ where $\Gamma = (1 - \frac{u^2}{c^2})^{-\frac{1}{2}}$. This energy will not change in the elastic scattering. When the particle enters the unshocked medium again, under an angle θ_2' as measured from the shocked medium, its energy is

$$E_2 = \Gamma^2 E_1 (1 + \frac{u}{c} \cos\theta_1)(1 + \frac{u}{c} \cos\theta_2') \tag{1.5}$$

For isotopic fluxes, average values of $\cos\theta_1$ and $\cos\theta_2'$ for particle crossing the shock front are $\langle \cos\theta_1 \rangle = \langle \cos\theta_2' \rangle = 2/3$. The average fractional energy increase ϵ is thus given by

$$\epsilon \equiv \left\langle \frac{\Delta E}{E} \right\rangle = \frac{E_2 - E_1}{E_1} = \frac{4}{3} \frac{u}{c} = \frac{V_s}{c} \tag{1.6}$$

where the second order terms are neglected. Thus, the energy of the particle is increased by a constant factor every time it goes back

and forth over the shock front. Particles are thrown away from the shock region together with the shocked material with velocity $V_s/4$. The number of particles escaping from the source per unit time and area is therefore $\rho V_s/4$, where ρ is the density of cosmic rays. The flux of particles crossing the shock back into the unshocked medium follows from the projection of an isotropic flux on the plane of the shock front. It is given by $c\rho/4$. The probability that a particle escapes from the shock region by advection instead of crossing back into the unshocked medium, is therefore $P_{esc} = V_s/c$. The combination of a constant increase in energy ϵ with a constant escape probability P_{esc}, gives rise to a power law spectrum:

$$\frac{dN}{dE} \propto E^{-\gamma} = E^{-1+\frac{\ln(1-P_{esc})}{\ln(1+\epsilon)}} \tag{1.7}$$

The values of P_{esc} and ϵ derived above are both much smaller than one and lead to a value for the spectral index of $\gamma = 2$. More detailed calculations indicate that values between 2.1 and 2.4 may be more realistic [17]. Nevertheless, many models of neutrino production assume a 'generic' spectrum of protons proportional to E^{-2}. The acceleration stops when the particles can no longer be confined to the source region by the magnetic field, when the energy loss via synchrotron radiation or inelastic interactions becomes comparable to the energy gain from the acceleration process, or when the shock decays.
The observed CR spectrum is steeper than the typical spectra predicted by the shock acceleration mechanism. This can be explained by models of CR propagation through the galaxy, which predict that high energy CRs have a higher probability to escape from the Galactic magnetic field. The remaining particles therefore have a steeper spectrum.
For extra-Galactic sources, the steepness of the observed spectrum is influenced by redshift and the GZK effect [12]. The expected shape of the spectrum at very high energies therefore depends on the distribution of CR sources in the universe.

1.2 Cosmic photons and γ-ray astronomy

The recent results of the γ-ray telescopes have identified the nature, location and energy spectrum of numerous sources.

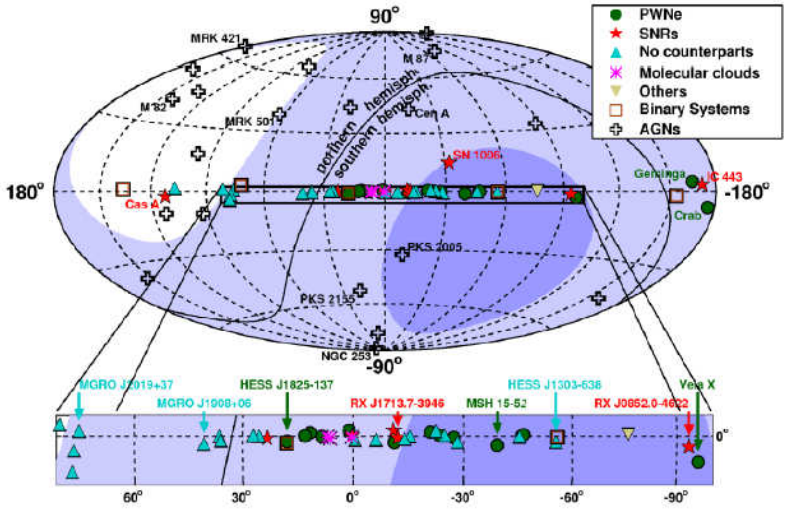

Figure 1.4: HESS catalogue of γ-ray sources. The visibility of the KM3NeT telescope is indicated by violet colours: light indicates a visibility less than 6 h per day , and dark indicates a visibility greater than 18 h per day. The solid line represents the equator.

The γ-rays are emitted in the acceleration of cosmic rays. The process of the electromagnetic emission can be originate by leptonic, hadronic or both of the processes (sections 1.2.1 - 1.2.2). The Energetic Gamma-Ray Experiment Telescope (EGRET) detected in the 1990s photons in the MeV ÷ GeV range[19]. The last EGRET catalogue contains 271 detections with high significance; it can be seen that apart from extragalactic objects like Active Galactic Nuclei or galactic Pulsars, most of the other sources have not been identified. Following its launch in June 2008, the Fermi Gamma-ray Space Telescope (Fermi) began a sky survey in August [27] . The Large Area Telescope (LAT) on Fermi in 3 months produced a deeper and better-resolved map of the γ-ray sky than any previous space mission. In figure 1.5 the 335 most significant γ-ray sources with energies above 100 MeV are shown; most of them are in the galactic plane.
Since gamma ray fluxes at energies greater than 100 GeV are very low, groundbased detectors are needed. High energy γ-rays are absorbed when reaching the Earth atmosphere, and the absorption process originates a cascade of high energy relativistic secondary particles. These

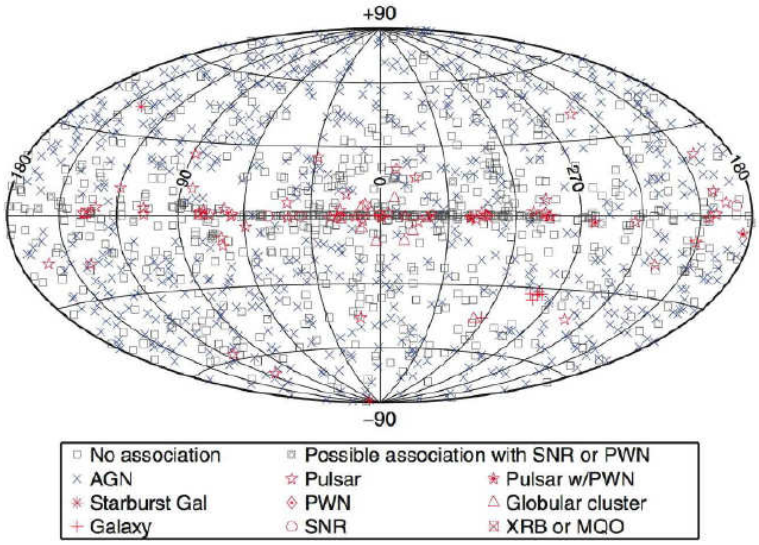

Figure 1.5: First Fermi-LAT catalogue of the 1451 γ-ray sources (Galactic coordinates). The colours are chosen to highlight the associated (with other catalogues) and non-blazar source [28].

particles will eventually emit Cherenkov radiation, at a characteristic angle in the visible and UV range, which can be detected at ground level by means of telescopes that collect the light towards photomultipliers. This method, the Imaging Air-Cherenkov Technique (IACT), can provide the direction and energy informations of the primary photon. Pioneering ground based γ-ray experiments proved the feasibility of the IACT, such as Whipple , HEGRA [24], CANGAROO [29] and CAT [30]. At present, the new generation apparatus are the HESS [25] and VERITAS [31] telescope arrays and the MAGIC telescope. These IACT telescopes have provided a catalogue of TeV γ-ray sources. Of particular interest (mainly for a neutrino detector placed in the North hemisphere) is the great population of TeVγ-ray sources in the galactic centre region discovered by the H.E.S.S. telescope (see figure 1.4). The mean free path travelled by photons is limited by interactions with the infra-red, microwave and radio background photons (figure 1.6).

1.2.1 Leptonic process

In the leptonic process, the photons are emitted by the electrons. The energy spectrum of these photons is characterized by two bumps

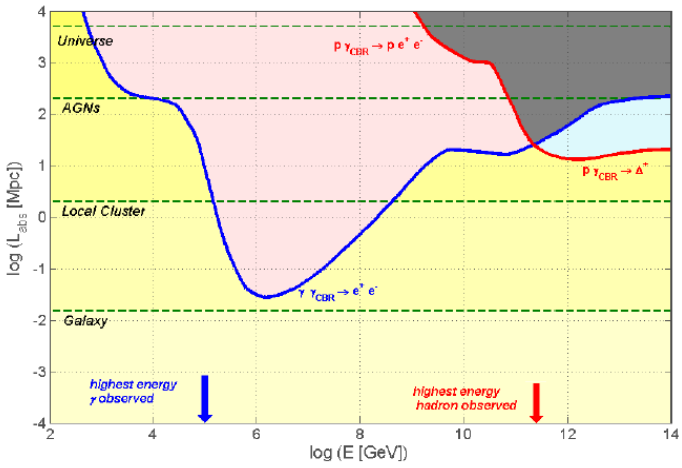

Figure 1.6: Absorption length of protons and gammas in the Universe as a function of particle energy. The grey shaded area indicates the region not accessible to proton and gamma astronomy.

(Figure 1.7). The low energy bump is due to the synchrotron radiation of the electrons accelerating in the magnetic fields. Equation 1.8 evaluates the decrease of the energy of these electrons.

$$-\frac{dE}{dT} = \frac{2}{3}\frac{ev}{mc}4E^2B^2 \tag{1.8}$$

where e, v and m are the electric charge, the velocity and the mass of the electron[1] respectively, c is the speed of light[2] , E and B are the electric and magnetic fields. The high energy bump is due to the inverse-Compton scattering (ICS) of photons produced within the jets or outside the jets.

1.2.2 Hadronic process

The shock acceleration mechanism reviewed in section 1.1.2 is only valid for charged particles. Particles electrically neutral such as photons or neutrinos are the decay products of accelerated charged particles. Both leptonic and hadronic particles can be accelerated in cosmic accelerators. It is assumed that black holes accelerate electrons, since synchrotron radiation observations indicate so. On the other hand, we

[1] $e = 1.602 \times 10^{-19}$C, $m = 9.109 \times 10^{-31}$kg
[2] $c = 2.99792458 \times 10^{8}$m s^{-1}

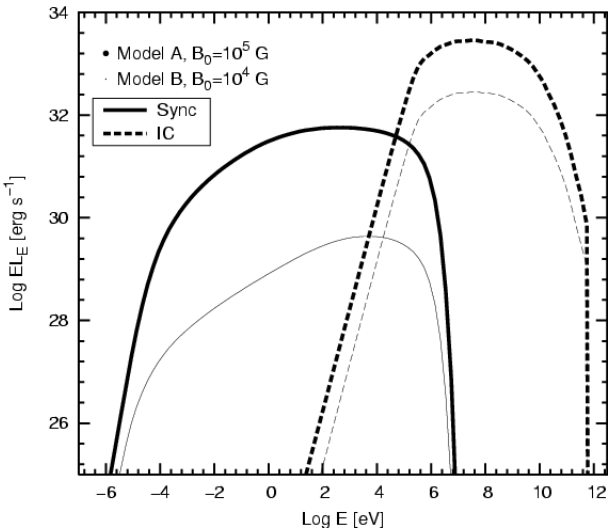

Figure 1.7: The energy spectrum of the photons by leptonic scenarios (Synchrotron and inverse Compton emission)

know that protons should be accelerated because they are detected as CR. Both models, the leptonic model and the hadronic model should coexist in parallel, but only the hadronic acceleration predicts the neutrino emission. Accelerated protons will interact in the surroundings of the CR emitter with photons predominantly via the Δ^+ resonance.

$$\begin{aligned} p + \gamma &\longrightarrow \Delta^+ \longrightarrow \pi^0 + p \\ p + \gamma &\longrightarrow \Delta^+ \longrightarrow \pi^+ + n \end{aligned} \tag{1.9}$$

Protons will also interact in *pp* and *pn* interactions. Charged pions and neutral pions will decay into neutrinos and γ-rays respectively. Therefore, the energy escaping from the source is distributed between CR, γ-rays and neutrinos. This implies that the observed CR flux will limit the expected neutrino flux, since the neutrino energy generation rate will never exceed the generation rate of high energy protons. The upper bound derived from a generic CR source is of:

$$E^2\Phi \leqslant (2 \cdot 10^{-8}\xi) GeV\, cm^{-2} s^{-1} sr^{-1} \tag{1.10}$$

where $\xi \simeq 1$ and depends on the model of the redshift energy loss of neutrinos.

The equation 1.10 is often referred to as the Waxman-Bahcall flux [18]. Waxman and Bahcall referred to this flux as a bound because, in reality,

more energy is transferred to the neutron than to the charged pion in the source. On the other hand, high energy photons can be produced in both leptonic and hadronic models. In figure 1.8, is shown at the present knowledge the sensitivity flux on extra-galactic neutrino production of several detectors with the upper bound of Waxman and Bahcall limit (WB), the latest measure of this limit comes from Icecube that adjusts the limit flux to $\approx 10^{-8} GeV cm^{-2} s^{-1}$. The most impor-

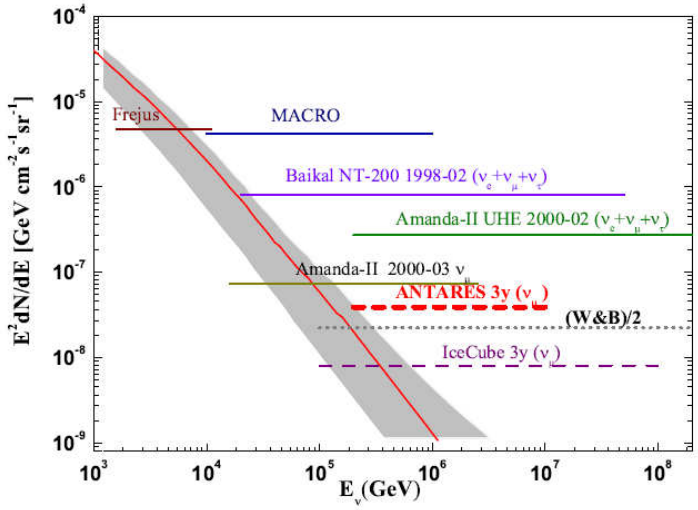

Figure 1.8: Sensitivities and upper limits for a E^{-2} diffuse high energy neutrino flux. Experimental upper limits are indicated as solid lines, the ANTARES [2] and IceCube [1] 90% C.L. sensitivities with dashed lines. The Frejus, MACRO, Amanda-II 2000-2003 limits refers to ν_μ. The Baikal and Amanda-II UHE 2000-2002 refers to all-flavours neutrinos. For reference, the Waxman and Bahcall limit [18],taking into account neutrino oscillations, for transparent sources is also shown.

tant processes to produce high energy γ-rays are the Inverse Compton (IC) scattering, and the neutral pion decay following *pp* interaction. IC γ-rays are produced in the interactions of energetic particles with the ambient background fields, the CMB, and the diffuse Galactic radiation of star light. This process is very efficient in producing γ-ray photons since low energy photons are found in all astrophysical objects. Multi-TeV electrons producing γ-ray of TeV energies via IC, produce as well synchrotron radiation of X-ray energies. Therefore, measurements of the synchrotron X-ray flux can derive an IC γ-ray expected flux value. The relationship between the γ-ray acceleration and the

hadronic acceleration model is the meson-decay channel. The most important process is the decay of π^0-mesons, $pp \longrightarrow \pi^0 \longrightarrow \gamma\gamma$. The γ-ray spectrum in this case, almost repeats the parent proton spectrum. Hence the γ-ray from hadronic models have crucial information about the primary nucleon CR.

1.3 Neutrino astronomy

Models of neutrino production rely on interactions of accelerated protons (or nuclei) with photon or matter fields in or near the accelerating astrophysical objects. In these interactions, charged and neutral pions are produced by 1.9. Neutrinos are produced from the decay of charged pions :

$$\begin{aligned} \pi^+ &\longrightarrow \mu^+ + \nu_\mu \longrightarrow e^+ + \nu_e + \nu_\mu + \bar{\nu_\mu} \\ \pi^- &\longrightarrow \mu^- + \bar{\nu}_\mu \longrightarrow e^- + \bar{\nu_e} + \nu_\mu + \bar{\nu_\mu} \end{aligned} \tag{1.11}$$

Roughly speaking the threshold of the $p\gamma \longrightarrow N\pi$ reaction is $E_p = 300MeV$ in the center of mass reference frame, assuming the main contribution due to the Δ^+ resonant channel, and the pion carries about 20% of the proton energy. The expected 'hadronic' gamma flux (produced in the $\pi^0 \longrightarrow \gamma\gamma$ channel) therefore follows a E^{-2} power law, as the primary Fermi proton flux, within the energy region constrained, at low energy by the Δ^+-resonance threshold and, at high energy, by E^p_{max} achievable in the cosmic accelerator. Similarly a muon neutrino flux is produced, with a spectrum E_ν^{-2} and average energy $E_\nu \simeq 5\% E_p$. If the muon cooling time in the source is larger than the muon decay time, high energy electron neutrinos are also produced with a production ratio of 2:1 (see equation 1.11).
A class of promising hadronic sources is formed by the TeV γ-sources that have no counterpart in other wavelengths, for this reason, called "Dark Accelerators". The number of these sources is, up to date, about 20 [33]. However, also for these sources, purely electromagnetic processes cannot be definitively ruled out and only the detection of high energy neutrinos will provide the ultimate 'smoking gun' to demonstrate the occurrence of hadron acceleration processes. Moreover the horizon of $E_\gamma > 10$ TeV γ-rays (VHE) is about 100 Mpc, this limits VHE gamma telescopes to the observation of the Galaxy and of the close

Universe (see figure 1.6).
The observation of astrophysical neutrinos will, therefore, open a window on the far high-energy Universe, where Active Galactic Nuclei (AGN) and Gamma Ray Burst (GRB) emissions are expected to play a major role. As discussed above, the scenario in which astrophysical sources are the accelerators of the observed hadronic cosmic rays, is nowadays strongly supported by several γTeV-ray observations. In the following it will describe the astrophysical environments proposed as sites for cosmic ray acceleration, VHE γ-rays and neutrino production. The sources presented in the following are candidates for high energy (HE) neutrino production and, some of them, are expected to produces ν-fluxes high enough to be detected by a km3-scale detector. For clarity sake we will deal with Galactic and Extragalactic sources separately. The first one are less luminous and less powerful, but thanks to their proximity to Earth, they could generate neutrino fluxes that can be observed as point-like sources. Moreover, in the hypothesis of hadronic emissions, the detected TeV gamma fluxes, provide a rather reliable estimate of the high energy neutrino fluxes. Extragalactic sources are expected to produce neutrino fluxes extending up to Ultra High Energies, that will emerge above the atmospheric diffuse flux. The most luminous ones are also candidate for point-like observation.

1.3.1 Extra-galactic sources

One of the most interesting features of the CR energy spectrum (figure 1.1), is the observation of ultra high energy cosmic rays (UHECR) above the ankle, that calls for the presence of very powerful extragalactic cosmic accelerators. In this section we will summarize the most relevant astrophysical observations concerning extragalactic sources with special emphasis on Active Galactic Nuclei (AGN) and Gamma Ray Burst (GRB). We will also present the current status of expectations for the related high energy neutrino fluxes and expectations for the GZK neutrino fluxes.

Active Galactic Nuclei

Active Galactic Nuclei (AGN), the most luminous persistent object observed in the sky, are galaxies whose electromagnetic radiation

have luminosity of the order of 10^{46} erg/s. The standard scenario for AGNs assumes the presence of a very massive central black hole ($10^6 \div 10^8 M_\odot$[3]) swallowing huge quantities of surrounding matter from an accretion disk and two relativistic jets where particles are accelerated up to the highest energy. The commonly used classification scheme for AGNs is based on the anisotropy of their emission with respect to the observer: depending on the observation angle AGNs are classified as quasars, Seyfert Galaxies, BL Lacs, and blazars, as shown in figure 1.9. Different features of the detected photon spectrum lead to

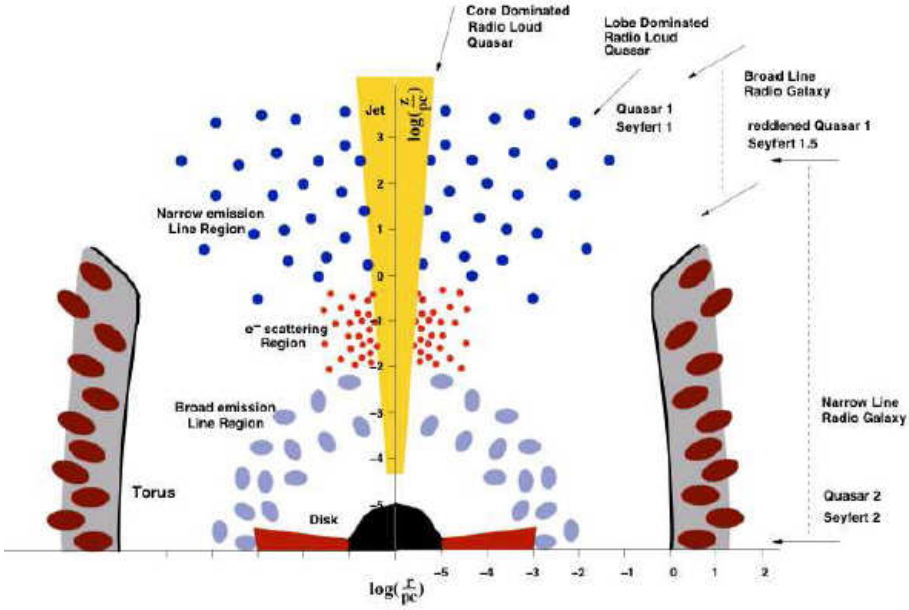

Figure 1.9: Scheme of a cylindrically symmetric AGN shown in the r-z-plane. It is indicated which objects are believed to be seen from particular directions.

more detailed classification. Although most of AGNs are radio-quiet, a particular ensemble of AGNs are Radio Galaxies where the radio emission, due to the synchrotron process, far exceed the luminosity at other wavelengths. Both radio-loud and radio-quiet AGNs are strong X-ray emitters and are considered as possible sources of UHECR and high energy neutrinos. A particularly interesting group of objects is the class of blazars showing relativistic jets almost aligned with respect to the line of sight of the observer. Indeed, the peculiar orientation of

[3]Sun mass $M_\odot = 1.9891 \times 10^{30}\ kg$

the blazars and the strongly enhanced flux of the Doppler boosted radiation allow to perform detailed multi-wavelength investigations of these objects. Several blazars have been recently observed in gamma TeV [34] and they are indeed the most numerous extra galactic objects observed in these wavelengths. Hadronic acceleration mechanisms were proposed to describe the observed AGN emissions, in this case a neutrino signal correlated to the TeV gamma rays is expected. Different hypotheses on the details of the acceleration mechanisms in AGNs, lead to different models and to fluxes that vary by substantial factors. Neutrinos can be produced by UHE proton beam dump close to the AGN core (a region optically thick both to CR and gamma rays), inside the AGN jet from protons accelerated by internal shocks or close to the radio lobes, at the end point of the jets. However, the question about the origin of the VHE gamma emission observed in blazars, namely leptonic or hadronic is still open.

Gamma Ray Burst

Gamma Ray Bursts (GRB) are among the most mysterious and violent phenomena ever observed in the Universe. A comprehensive review is reported in the reference [35], in the following only the basic features and their possible association with high energy neutrino emission are discussed. The total energy release of GRBs is huge ($\geqslant 10^{51}$ erg) though they are transient sources: their emission in hard X-ray and soft gamma photons lasting from millisecond to several hundreds of seconds, with a late afterglow in IR, radio and optical band. Historically, Gamma Ray Bursts were discovered as extremely intense gamma ray flashes in 1967 by the Vela satellites, launched by the U.S. to monitor the sky for nuclear explosions that might violate the Nuclear Test Ban Treaty. It was soon realized that GRB distribution in the sky is almost isotropic, thus suggesting an extragalactic origin, and their emission has been measured over a very broad interval of wavelength. A major step was provided in the late 90's by the Beppo-SAX satellite measurement of the X Ray afterglow that permitted to localize the GRB and to send an alert to ground based optical telescopes that succeed in identifying the host galaxy and determining its redshift, thus providing a conclusive evidence of the fact that GRB are at cosmological distances.

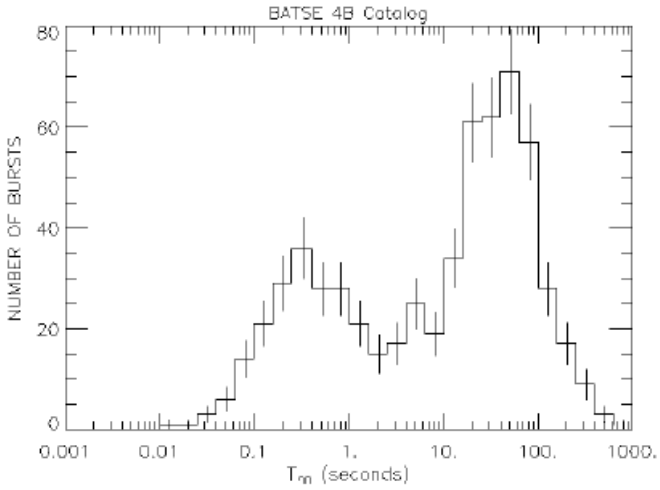

Figure 1.10: Distribution of t_{90} for 1234 GRBs in the BATSE 4B catalogue. t_{90} is defined as the time at which 90% of the signal is detected.

A subsequent important step was achieved through the HETE-2 satellite that, beside many other interesting observations, localized GRB 030329 that was the first GRB unambiguous associated with a supernova explosion [36, 37]. The launch of the SWIFT satellite [38] in November 2004 lead to further remarkable advances in the field revealing the unexplored afterglow behaviour lasting from minutes to hours, as well as the afterglow of so called "short" gamma-ray bursts (gamma emission briefer than 2 sec, described in the following) and extending the gamma-ray burst observations beyond z=6 in redshift[4] where very few astrophysical objects have been ever measured. The last frontier of GRB detection was achieved with the launch of FERMI satellite [27] in June 2008 that largely extends the observability of GRB at energy higher than 100 MeV detecting almost 250 burst/year. However, in spite of a large numbers of GBRs observed since their discovery and of the fact that their emission features have been studied into details, the nature of these objects remains mysterious to a large extent. The bulk of the emission features indicate a non-thermal process, driven by a catastrophic event involving charged particle acceleration and the conversion of huge quantities of matter into energy. GRBs are between

[4] $z = \frac{\lambda_{obs} - \lambda_{emit}}{\lambda_{emit}}$ where λ_{emit} and λ_{obs} are the emitted and observed wavelengths of an object.

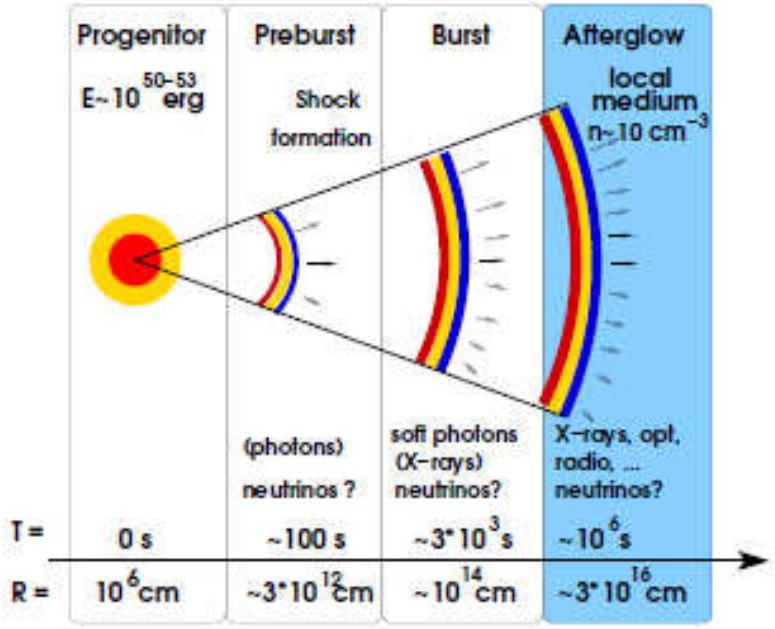

Figure 1.11: Schematic representation of the GRBs fireball model

the brightest sources, their total luminosity under the hypothesis of isotropic emission being around $L_{GRB} \simeq 10^{51}$ erg/s: these source are four orders of magnitude brighter than Active Galactic Nuclei, the most luminous steady sources in the sky , with luminosity $L_{AGN} \simeq 10^{44 \div 47}$ erg/s. While GRBs emit only for a short time, AGNs are active for long periods, so that the integrated luminosity is comparable, being about 10^{46} erg.

Figure 1.10 shows the distribution of the duration t_{90} of the bursts, the time at which 90% of the signal was recorded. As previously mentioned, two populations of bursts can be identified, classified as "short" ($t_{90} < 2$ s) and "long" bursts ($t_{90} > 2$s). The standard model for GRBs is the fireball model [39], schematically described in figure 1.11. This model does not provide any constraint on the progenitor, but yields a phenomenological description of the actual bursts observations. The basic idea is that a large amount of mass is ejected within a short time window. The plasma is later ejected in shells. At some point, the outer shells slow down and are reached by inner and younger shells, producing a shock wave that accelerates charged particles up

to very high energies: while protons can be accelerated loss-free up to very high energies ($E \simeq 10^{21}$ eV), electrons loose their energy emitting synchrotron radiation, that escapes from the shock region. This is observed as prompt emission from GRBs. Those shocks resulting from collisions are called internal shocks, while external shocks result from collisions of the shells with the interstellar medium, leading to afterglow emission. While during the prompt emission gamma-rays of energy > 100KeV are detected, afterglow emission is observed in almost all wavelengths bands.

1.3.2 Galactic sources

Ultra-relativistic charged particles produced inside our Galaxy remain trapped by the galactic magnetic field, that has a typical strength $B \simeq 3\mu Gauss$. The Larmor radius, or gyroradius, of a charged particle of atomic number Z in a magnetic field B is given by 1.2. Magnetic confinement becomes impossible when the gyroradius is comparable with the linear dimensions of the Galaxy. This corresponds to energy:

$$E \geqslant ZeBR_{halo} \simeq 2.7 \times 10^{19} Z(\frac{B}{3\mu Gauss})(\frac{R_{halo}}{10kp}) \tag{1.12}$$

Most CR particles have much lower energy and a gyroradius that is much smaller than the galactic size. The motion of these particles can be well approximated as a diffusive process controlled by the random component of the galactic magnetic field. The time needed for a CR particle to diffuse out of the galactic halo is a function of its rigidity (which is given by E/Z for ultra-relativistic particles). An important consequence is that (assuming stationary) the number $N_A(E)$ of CRs of type A and energy E in the Galaxy is:

$$N_A(E) \simeq Q_A(E)\tau(E/Z) \tag{1.13}$$

where $Q_A(E)$ is the injection rate and $\tau(E/Z)$ is the confinement time. Therefore the observed CRs spectrum has not the same energy distribution of the particles near their sources, but is distorted and steepened by confinement effects. Relative abundances of 'secondary nuclei' (such as Lithium, Beryllium and Boron) in the CRs are used to evaluate the confinement time : these nuclei are rare in the Solar System, since they

are almost absent in final phases of the stellar nucleosynthesis. On the other hand, these light elements are relatively abundant in CRs, because they are produced in the spallation of parent nuclei, like Oxygen and Carbon, each time they interact with the Interstellar Medium. In the same way Sc, Ti and V are produced in Ni and Fe spallation processes.
Given the relative abundances of these elements in our Galaxy, a confinement time $\tau_{CR} = 3 \times 10^6 yrs$ is obtained.

Super Nova Remnants

The power of the ensemble of CR sources in the Milky Way can be estimated as the ratio between the total energy of CRs in the Galaxy, divided by their average confinement time:

$$L_{CR}^{galaxy} \simeq \rho_{CR} V_{eff} / \langle \tau_{CR} \rangle \simeq 2 \times 10^{41} (erg/s) \tag{1.14}$$

where $\rho_{CR} = 1.6 eV/cm^3$ is the local CR energy density,V_{eff} is the effective volume of 170 kpc^3 and $\langle \tau_{CR} \rangle$ is the average confinement time. On the basis of this luminosity evaluation, Super Novae remnants are the most likely sources to produce galactic CRs. In addition to these energy balance considerations, in the 1970 a dynamical argument emerged in favour of the Super Nova (SN) hypothesis, when it became clear that the spherical shock waves produced in the interstellar medium by the (supersonically moving) SN ejecta, can provide the environment where charged particles are accelerated up to very high energies, generating a power law spectrum with a well defined slope $\alpha \simeq 2$: that is well compatible with the injection spectrum needed to generate the observed CRs.
The basic concept behind this theory is an extension of the ideas developed by Enrico Fermi, who in 1949 made the hypothesis that the acceleration of CRs is a stochastic process, where each CR particle acquires its high energy in many collisions with moving plasma clouds. The clouds carry (in their own rest frame) turbulent magnetic fields and act as magnetic mirrors transferring on average a positive amount of energy to the scattering particles with $\langle \Delta E \rangle / E \propto \beta^2$($\beta$ indicates the cloud velocity). This process generates a power law spectrum, with higher energy particles having performed a larger number of collisions.

The crucial new element introduced in the 1970's is the presence of the shock wave. In this updated version of the acceleration model, charged particles are accelerated by the scattering against magnetic irregularities present both upstream and down- stream of the shock front that act as Fermi's clouds. The new geometry allows for a more efficient acceleration, $\langle \Delta E \rangle / E \propto \beta$, and the (mass, momentum and energy conservation) constraints of the fluid properties across the shock determine the slope $\alpha = 2 + \epsilon$ of the accelerated particle spectrum (see section 1.1.2). Shocks are generated every time that macroscopic amounts of matter move at supersonic speed. Particularly interesting case are the jets emitted by Gamma Ray Bursts, by accretion Black Holes of stellar mass (microquasars) or by Active Galactic Nuclei. In all these objects there is in fact evidence for charged particle acceleration. In the vicinity of young Super Nova Remnant (SNR) one should find a population of relativistic hadrons (protons an nuclei) with a spectrum close to the injection one ($E^{-2+\epsilon}$) and a total energy of order of 0.2×10^{51} erg. These relativistic particles can interact with the interstellar medium around the SN producing neutral and charged pions that then decay generating photons and neutrinos with a spectrum that approximately follows the same power law of the parent proton spectrum. In 2004 the H.E.S.S. experiment observed the Super Nova Remnant RX J1713.7-3946 as a very bright source of TeV photons, as shown in figures 1.12 and 1.14. The property of the photons from this source are consistent with the expectation of the "SNR paradigm" for galactic cosmic rays. Several other young SNR have also been detected by identifying TeV photons: these observation gives support to the possibility that Super Nova Remnants are sites for CRs acceleration. This conclusion is however not unambiguous: also for the best candidate source RX J1713.7-3946 a "leptonic origin" of the radiation (syncrotron radiation and inverse Compton effect of relativistic $e^{\pm}$ on the radiation fields around the SN) cannot be entirely excluded. A recent estimation of neutrino event rates coming from these sources [40] shows that a detection seem possible in a cubic-kilometer scale neutrino telescope placed in the Northern hemisphere. This is the central point of this work and results will be shown on chapter 6.

Microquasar

Micro-quasars are one of the most promising Galactic candidates for neutrino astronomy. They are galactic X-ray binary systems composed of an accreting massive object such as a black hole or a neutron star and a companion star which provides mass to the firs one. They display relativistic radio-emitting jets, probably fed by the accretion of matter from the companion star. Micro-quasar resemble AGN (see 1.3.1), but at a much smaller scale.
The best candidates as neutrino sources are the steady micro-quasars SS433 and GX339-4. Assuming reasonable scenarios for TeV neutrino production, a km3 scale neutrino telescope in the Mediterranean sea could identify micro-quasars in a few years of data taking, with the possibility of a 5σ level detection. In case of no observation, it would strongly constrain the neutrino production models and the source parameters.

Neutrinos from the Galactic Centre

The galactic center (GC) is specially appealing for a Mediterranean neutrino telescope since it is within the sky view of a telescope located at such latitude. Early HESS observations of the GC region detected a point-like source at the gravitational centre of the Galaxy (HESS J1745-290 [41]) coincident with the supermassive black hole Sagittarius A^* and the SNR Sgr A East. In 2004, a more sensitive campaign revealed a second source, the PWN G $0.9 + 0.1$. The measured gamma-ray spectrum in the GC region is well described by a power law with index of about 2.3. The spectral index of the gamma-rays, which closely traces back the spectral index of the CRs, indicates in the Galactic centre a local CR spectrum that is much harder and denser than that as measured at Earth. It is thus likely that an additional component to the CR population is present in the Galactic Centre, above the diffuse CR concentration which fills the whole Galaxy.

1.4 Galactic sources of interest

Above all we want to focus on two important objects in the galaxy that have been analysed in our work: the SNR RXJ1713.3946 and the

Fermi-Bubbles. The analysis on these two objects will be shown in the chapter 6.

1.4.1 Super Nova Remnant RXJ1713.3946

We present observations of the young Supernova remnant (SNR) RXJ1713.7-3946[5], discovered in soft X-rays in 1996 in the ROSAT all-sky survey [42]. RX J1713.7-3946 was later extensively studied by

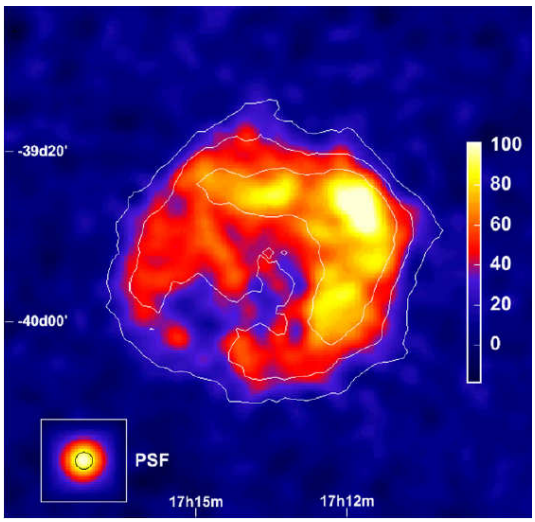

Figure 1.12: The gamma ray image of RX J1713.7-3946 obtained with the HESS telescope array in 2004. The linear color scale is in units of excess counts. The image of the source is based on a 40 h data sample. The overall statistical significance of 39σ is based on an excess of 7700 gamma-ray events. The point-spread function (PSF) of the instrument is shown in the lower left hand corner.

the ASCA, Chandra and XMM x-ray satellites and it was reported as a source of gamma-TeV emission by the CANGAROO collaboration. The first HESS probe of RX J1713.7- 3946 in 2003 confirmed this result and, more importantly, provided a unique gamma-ray image of the remnants on arcminute scales [32] (see figure 1.12). The origin of the TeV gamma-ray emission from RX J1713 has been a matter of active debate. There are two competing processes potentially responsible for the shell-like TeV gamma-ray emission from RX J1713: Inverse Compton (IC) scattering on the cosmic microwave background by relativistic

[5]also known as G347.3-0.5

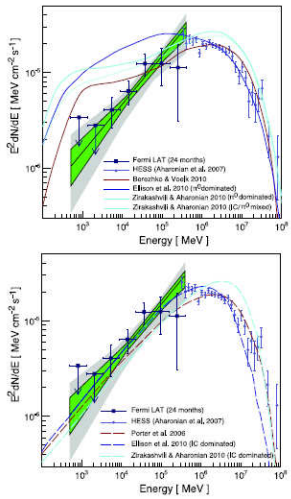

Figure 1.13: Energy spectrum of RX J1713.7-3946 in gamma rays. Shown is the Fermi-LAT detected emission in combination with the energy spectrum detected by HESS. The top panel features predictions assuming that the gamma-ray emission predominately originates from the interaction of protons with interstellar gas. The bottom panel features models where the bulk of the gamma-ray emission arises from interactions of electrons with the interstellar radiation field (leptonic models).

electrons (leptonic model) and π_0-decay gamma rays resulting mainly from inelastic collisions between relativistic protons and ambient gas nuclei (hadronic model). The last one hypothesis should make "visible" RXJ1713 also to neutrino telescopes.

This source was clearly detected in a position coincident with the SNR. It is extended with a best-fit extension of $0.55° \pm 0.04°$ matching the size of the non-thermal X-ray and TeV gamma-ray emission from the remnant. The positional coincidence and the matching extended emission allows us to identify the LAT source with the supernova remnant RXJ1713.7-3946. RXJ1713.7-3946 is a young remnant suggested to be associated with the appearance of a guest star in the constellation of Scorpius. It is located in the Galactic plane (at l = 347.3°, b = -0.5°) and at a suggested distance of 1 kpc with angular diameter of $65' \times 55'$, the size of the shell is 20 pc. This region is dominated by non-thermal activity; its X-ray emission shows a featureless spectrum interpreted to be completely dominated by X-ray synchrotron emission from ultra-relativistic electrons [43]. To compute the angular extension of RXJ1713 the extension and position of the

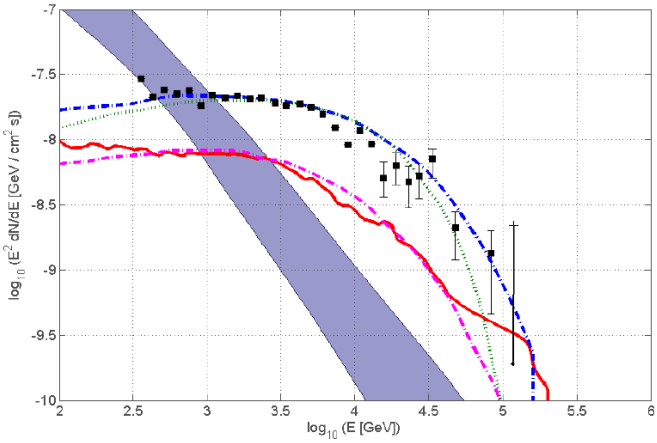

Figure 1.14: RXJ1713-3946: TeV neutrino fluxes expected calculated by Vissani et. al (red line) [20] and Amato et al. [21] (magenta dash-dotted line). The HESS data, from combined 2003, 2004 and 2005 source observations (black squares), are shown for comparison together with the hadronic-origin TeV gamma ray flux calculated by Amato et al. (blue dash- dotted line) [21] and Berezkho et al. (dark green dotted line) [22] is also shown. The solid lines delimiting the shaded area represent the expected atmospheric neutrino background for a 0.5° bin and 1° neutrino search bin respectively.

gamma-ray emission are fitted with a disk of varying radius. The emission is found to be significantly extended and the best fit position $(\alpha_{RA}, \delta) = (258.50° \pm 0.04°, -39.91° \pm 0.05°)$ is consistent with the center of SNR within 0.2° and the best-fit radius is $0.55° \pm 0.04°$. The energy spectrum of the entire remnant based on the data is shown in figure 1.13. The overall gamma ray energy spectrum was measured over more than two decades, from 190 GeV to 40 TeV. The spectrum clearly deviates from a pure power law spectrum. It can be reasonably well described by a power law with an exponential cutoff as reported in table 1.1. Trough some calculations in the hypothesis of an hadronic emission of gamma-rays[20][21], is possible estrapolate the attended flux also for HE neutrinos that came from RXJ1713. The neutrino fluxes expected in this case is shown in figure 1.14. RX J1713.7-3946 seems to be a unique object with very unusual characteristics. First, the x-ray emission does not contain a measurable thermal component. This could be an indication that the supernova explosion occurred inside the wind-blown bubble [44] with a low gas density ($n < 1 cm^{-3}$) which makes the hadronic origin of gamma rays less attractive, although does

Fit formula	Fit Parameters	χ^2
$I_0 E^{-\gamma}$	$I_0 = 20.5 \pm 0.4$, $\gamma = 2.32 \pm 0.01$	145.6
$I_0 E^{-\gamma} e^{-(\frac{E}{E_c})^\beta}$	$I_0 = 21.3 \pm 0.5$, $\gamma = 2.04 \pm 0.04$ $\beta = 1.0$, $E_c = 17.9 \pm 3.3$	39.5
	$I_0 = 34.1 \pm 2.5$, $\gamma = 1.79 \pm 0.06$, $\beta = 0.5$, $E_c = 3.7 \pm 1.0$	34.3
	$I_0 = 40.5 \pm 1.5$, $\gamma = 1.74 \pm 0.02$, $\beta = 0.45$, $E_c = 2.3 \pm 0.2$	34.2
$I_0 E^{-\gamma+\beta \cdot \log(E)}$	$I_0 = 20.6 \pm 0.5$, $\gamma = 2.02 \pm 0.04$, $\beta = -0.29 \pm 0.03$	38.8

Table 1.1: Fit results for different spectral models for the γ-ray emission of RXJ1713.3946. The fit range is chosen form 0.3 to 113 TeV. The differential flux normalization I_0 is given in units of $10^{-12} cm^{-2} s^{-1} sr^{-1} TeV$

not exclude it.

1.4.2 The Fermi Bubbles

The recent analysis on Fermi data of 2010 has shown an evidence of a new feature in Milky Way detecting gamma-rays with a hard and relatively uniform energy spectrum [45][46][48]. Observation of gamma-

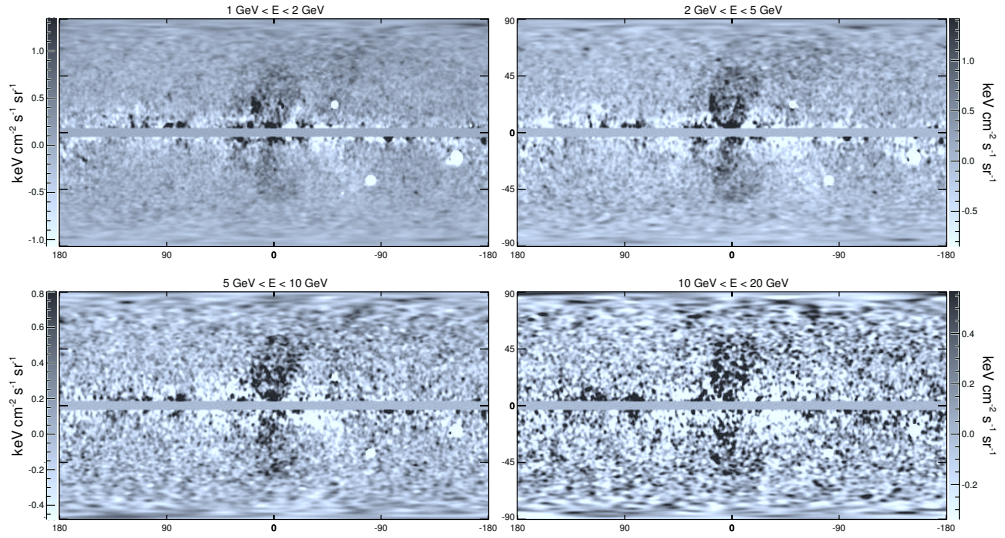

Figure 1.15: All-sky residual maps after subtracting the Fermi diffuse Galactic model from the LAT 1.6 year maps in 4 energy bins. Two bubble structures extending to $b \pm 50°$ appear above and below the GC, symmetric about the Galactic plane [45, 46].

ray emission in the inner galaxy at $E \lesssim 1 GeV$ was observed since 80s

years. EGRET lacked the sensitivity and angular resolution to reveal the detailed structure of gamma-ray emission toward the inner galaxy. For energies up to 100 GeV the Fermi Gamma Ray telescope [47] has data with sufficient angular resolution. At lower energies a structure in the X-ray region, later interpreted as a superwind bubbles (SWB), was revealed by ROSAT [49] in a region of tens degrees around the Galactic Center (GC). Other experiments have confirmed the existence of a limb-brightened bipolar structures called Galactic center lobe (GLC) with origin on the GC on the degree scale. Beyond the direct evidence of shell structures, an excess in microwave[6] with spherical morphology about 4 kpc in radius toward the GC (visible up to at least $|b| \approx 30°$) [50]) has been recognised. This so called "microwave haze" has a spectrum harder than typical synchrotron emission and has been interpreted as a synchrotron emission from a hard spectrum of electron CRs. A

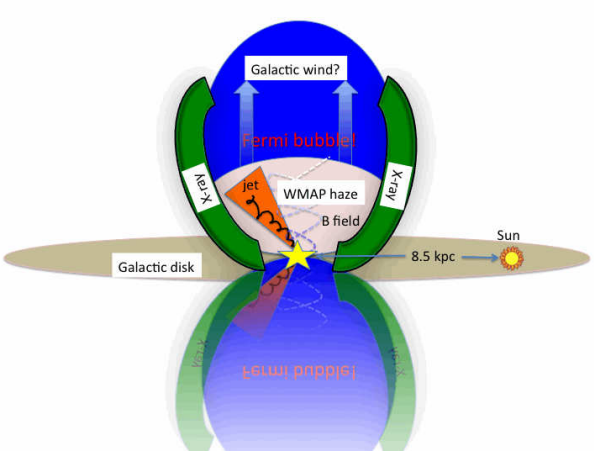

Figure 1.16: A cartoon picture to summarize the observations of the Fermi bubble structures. Two blue bubbles symmetric to the Galactic disk indicate the geometry of the gamma-ray bubbles observed by the Fermi-LAT. Morphologically, we see corresponding features in ROSAT soft X-ray maps, shown as green arcs embracing the bubbles. The WMAP haze shares the same edges as the Fermi bubbles (the pink egg inside the blue bubbles) with smaller extension in latitude. These related structures may have the same physical origin: past AGN activities or a nuclear starburst in the GC (the yellow star).

simple model, in which the electron CRs that form the haze have dif-

[6] soft synchrotron, and thermal dust emission has been removed like all the other different known emission mechanisms

fused from supernova shocks in the disk, cannot fully explain the data for standard diffusion assumptions. Besides the hard spectrum, it is difficult to form the distinctly non-disklike morphology of the haze with any population of sources concentrated in the disk (as is believed to be true of supernovae). The presence of a distinct component of

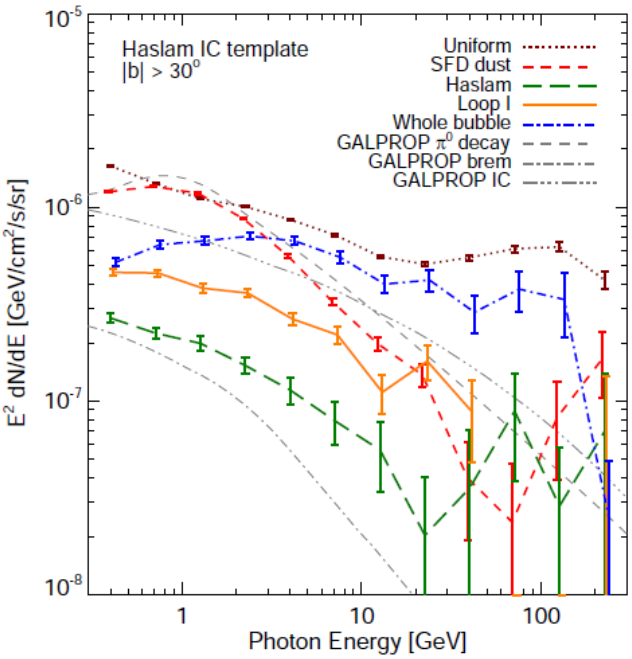

Figure 1.17: Correlation spectra for the 5-template fit employing an Haslam 408 MHz map [52] instead of the simple disk model. The SFD-correlated spectrum is shown by the red short-dashed line which roughly traces π_0 emission (the grey dashed line indicates a GALPROP [45] prediction for π_0 emission). The disk-correlated emission is shown by the green dashed line, which traces the soft IC (grey triple-dot-dashed line) and bremsstrahlung (grey dot-dashed line) component. The spectrum of the uniform emission, which traces the isotropic background (including possible CRs contamination), is shown as a dotted brown line. The solid orange line indicates the spectrum of emission correlated with Loop I (north), which has a similar spectrum to the disk-correlated emission. Finally, the blue dot-dashed line shows the spectrum correlated with the Fermi bubble template. The correlation spectra have been normalized to a reference region (see [45])

diffuse hard electron CR far off the plane has motivated proposals where the haze is generated by pulsars, other astrophysical processes, or the annihilation of dark matter. Taken together, the measurements

of several experiment [7] imply a new source of hard electrons and positrons, which may be related to the *Wilkinson Microwave Anisotropy Probe* (WMAP) haze. The coexistence of ROSAT X-ray bipolar features and the WMAP haze toward the inner Galaxy also suggests the interesting possibility of a common physical origin for these signals. If the WMAP haze is synchrotron radiation from a hard electron population located around the GC, the same CRs would also produce IC scattered gammas. Fermi-LAT skymaps constructed on 1.6 years data reveal two large gamma-ray lobes, extending 50 degrees above and below the GC, with a width of about 40 degrees in longitude and shown in figure 1.15. These two "bubble"-like structures have relatively sharp edges and are symmetric with respect to the galactic plane and the minor axis of the galactic disk, a pictorial view of these bubbles is shown in figure 1.16. The gamma-ray signal reveals similar morphology to the WMAP haze, and is also suggestive of a common origin with features in the ROSAT X-ray maps at 1.5 keV towards the GC.

The sharp edges, bilobular shape, and apparent centring on the GC of these structures suggest that they were created by some large episode of energy injection in the GC, such as a past accretion onto the central black hole, or a nuclear starburst in the last 10 Myr. It is well known that the GC hosts a massive black hole and massive clusters of recently formed stars. Either of these could potentially provide the necessary energy injection by driving large-scale galactic winds or producing energetic jets.

If the bubbles are expanding rapidly and highly accelerated protons responsible for the gamma-ray emission are trapped behind shock fronts, then sharp edges for the Fermi bubbles could occur naturally. However, in the presence of such a shock, electrons would also be accelerated, and would generally produce more gamma rays than the protons via ICS. It might be thought that the presence of a bright X-ray edge could lead to a sharp edge in the gamma-ray signal, via IC scattering of electron CRs on the X-ray photons. The energy of IC scattered photons is of order $(\Gamma_e/2)E_e$, with $\Gamma_e = 4E_eE_\gamma/m_e^2$ (where E_γ and E_e are the initial photon and electron energies, respectively, and m_e is the electron mass), and

[7] The ATIC, Fermi and HESS experiments have observed a hardening in the $e^+ + e^-$ spectrum at 20-1000 GeV [51], with an apparent steepening at 1 TeV, and the PAMELA experiment has measured a rising positron fraction above 10 GeV.

the scattering cross section is independent of the initial electron and photon energies. Thus a higher-energy photon population, leading to a larger value of Γ_e, allows IC gamma-rays at a given energy to originate from lower-energy electrons, which are much more abundant for typical electron spectra with $dN/dE \sim E^{-\gamma}$, $\gamma \gtrsim 2$. The Fermi bubbles are morphologically and spectrally distinct from both the π_0 emission and the IC and bremsstrahlung emission from the disk electrons. As shown in figure 1.17, the Fermi bubbles have a distinctly hard spectrum, $dN/dE \sim E^{-2}$, with no evidence of spatial variation across the bubbles. Theoretical models on possible high energy neutrino fluxes from the bubbles have been developed [48].

Chapter 2

High Energy neutrino detection

As shown in the previous chapter, light and neutral neutrinos are optimal probes for high energy astronomy, for example for the identification of astrophysical sources of UHE particles. To fulfil this task neutrino detectors must be design to reconstruct both the neutrino energy and direction, thus they are commonly referred as "Neutrino Telescopes". In this chapter are explained the different neutrino detection techniques and their application depending on the neutrino energy and flavour.

2.1 Physics of neutrinos

Leptons are one of the three classes of particles in the Standard Model (SM); they are spin-1/2 fermions without strong interactions. There are six known leptons, and they occur in pairs called "generations" which we write as doublets:

$$\begin{pmatrix} e^- \\ \nu_e \end{pmatrix} \begin{pmatrix} \mu^- \\ \nu_\mu \end{pmatrix} \begin{pmatrix} \tau^- \\ \nu_\tau \end{pmatrix} \\ \begin{pmatrix} e^+ \\ \bar{\nu}_e \end{pmatrix} \begin{pmatrix} \mu^+ \\ \bar{\nu}_\mu \end{pmatrix} \begin{pmatrix} \tau^+ \\ \bar{\nu}_\tau \end{pmatrix} \tag{2.1}$$

The three charged leptons (e, μ, τ) have charge $Q = \pm e$. Associated with them are the three neutral neutrinos and anti-neutrinos. The charged leptons interact via both electromagnetic and weak forces, whereas for neutrinos only weak interactions have been observed.

2.1.1 The "solar neutrino problem"

The existence of neutrinos was first postulated by Pauli in 1930 in order to understand the β-decays.

$$(Z, A) \longrightarrow (Z + 1, A) + e^- + \bar{\nu}_e \tag{2.2}$$

Looking at the energy in reaction 2.2, if the anti-neutrino is not present the reaction would be a two-body decay and the energy of emitted electron would have a unique value (neglecting the nuclear recoil energy): $E_{e^-} = \Delta M = M(Z, A) - M(Z + 1, A)$. However if anti-neutrino is present the electron energy will not be unique , but will lie in the range:

$$m_{e^-} \leqslant E_{e^-} \leqslant (\Delta M - m_{e^-}) \tag{2.3}$$

Experimentally, the observed spectrum spans the whole range 2.3 with the mass of neutrino closer to zero. Careful study of the spectrum near the end point:

$$E_{e^-} = \Delta M - m_{e^-} \tag{2.4}$$

allows an upper limit to be set on the neutrino mass. The best results come from the β-decay of tritium

$$^3H \longrightarrow ^3 He + e^- + \bar{\nu}_e \tag{2.5}$$

which gives:

$$m_{\bar{\nu}_e} < 17\ eV/c^2 \approx 3 \times 10^{-5} m_e \tag{2.6}$$

The SM assumes the neutrinos be massless; the result in 2.6 is a first hint that it could be wrong. Neutrino oscillation experiments opened a window to a previously unexplored aspect of particle physics: neutrino masses and lepton flavour mixing [53]. The first evidence of it came from the experimental evidence that atmospheric and solar neutrino fluxes were smaller than expected; this discrepancy constitues the so-called "solar neutrino problem" . Indeed the Standard Solar Model [54] predicted a certain flux of ν_e that was not confirmed by experiments. The first of these by Homestake in 1960 [55] were exploited ν_e absorption on ^{37}Cl through the reaction $^{37}Cl + \nu_e \longrightarrow ^{37} Ar + e^-$. Gallium experiments (GALLEX and GNO at Gran Sasso in Italy and SAGE at Baksan in Russia) utilize the reaction:

$$\nu_e + ^{71} Ga \longrightarrow ^{71} Ge + e^- \tag{2.7}$$

They are sensitive to the most abundant *pp* solar neutrinos. The Kamiokande experiment in Japan succeeded in real-time solar neutrino observation, utilizing neutral current $\nu_e - e^-$ scattering, in a large water-Cherenkov detector. This experiment takes advantage of the directional correlation between the incoming neutrino and the recoil electron. This feature greatly helps the clear separation of the solar-neutrino signal from the background. Later, the high-statistics Super-Kamiokande experiment [58] with a 50-kton water Cherenkov detector replaced the Kamiokande experiment. Due to the high thresholds (7 MeV in Kamiokande and 5 MeV at present in Super-Kamiokande) the experiments observe pure solar neutrinos from 2.8 reaction.

$$\begin{array}{c} p + {}^7\mathrm{Be} \longrightarrow {}^8\mathrm{B} + \gamma \\ \downarrow \\ {}^8\mathrm{Be} + e^+ + \nu_e \end{array} \tag{2.8}$$

In 1999, a new real time solar-neutrino experiment, SNO (Sudbury Neutrino Observatory), in Canada started observation. This experiment used 1000 tons of ultra-pure heavy water contained in a spherical acrylic vessel, surrounded by an ultra-pure water shield. SNO measured ^{8}B solar neutrinos via the charged-current (CC) and neutral-current (NC) reactions. The CC reaction,is sensitive only to ν_e, while the NC reaction, is sensitive to all active neutrinos. This is a key feature to solve the solar neutrino problem. If it is caused by flavour transitions such as neutrino oscillations, the solar neutrino fluxes measured by CC and NC reactions would show a significant difference. The results of experiments are shown in Table 2.1. So all of these experiments showed that probably neutrinos can change their flavour. In particular KamLAND was an experiment of 1-kton of ultra-pure liquid scintillator detector located at the old Kamiokande's site in Japan. The primary goal of the KamLAND experiment was a long-baseline (flux-weighted average distance of about 180 km) neutrino oscillation studies using $\bar{\nu}_e$'s emitted from nuclear power reactors. Also KamLAND confirmed the results of SNO.

	$^{37}Cl \longrightarrow ^{37} Ar$ (SNU)	$^{71}Ga \longrightarrow ^{71} Ge$ (SNU)
Homestake	$2.56 \pm 0.16 \pm 0.16$	-
GALLEX	-	$77.5 \pm 6.2^{+4.3}_{-4.7}$
GNO	-	$62.9 \pm 6.2^{+5.5}_{-5.3} \pm 2.5$
GNO+GALLEX	-	$69.3 \pm 4.1 \pm 3.6$
SAGE	-	$65.4^{+3.1+2.6}_{-3.0-2.8}$
SSM	$8.46^{+0.87}_{-0.88}$	$127.9^{+8.1}_{-8.2}$

Table 2.1: Results from radiochemical solar-neutrino experiments. The predictions of a recent standard solar model BPS08(GS) are also shown. The first and the second errors in the experimental results are the statistical and systematic errors, respectively. SNU (Solar Neutrino Unit) is defined as 10^{-36} neutrino captures per atom per second.

2.1.2 Oscillations of neutrinos

Oscillations of neutrinos are consequence of the presence of neutrino mixing, or lepton mixing, in vacuum.

In the formalism used to construct the SM, this means that the left-handed (LH) flavour neutrino fields which enter into the expression for lepton current in the CC weak interaction Lagrangian, are given by:

$$\nu_{lL}(x) = \sum_j U_{lj}\nu_{jL}(x) \;\; \text{with } l = e, \mu, \tau \tag{2.9}$$

where $\nu_{jL}(x)$ is the LH component of the field of neutrino ν_j possessing a mass m_j and U is the unitary neutrino mixing matrix. Equation 2.9 implies that the individual lepton charges are not conserved. All neutrino oscillation data can be described assuming 3-neutrino mixing in vacuum. The number of massive neutrinos can, in general, be bigger than three if exist sterile neutrinos and if they can mix with the other flavour neutrinos. Perhaps at the present there are no experimental evidences of more than 3 flavour neutrinos. It follows from the current data that at least 3 of the neutrinos ν_j (ν_1, ν_2, ν_3) must be light ($m_{1,2,3} \lesssim 1eV$) and must have different masses ($m_1 \neq m_2 \neq m_3$). All compelling data on neutrino oscillations can be described assuming 3-flavour neutrino mixing in vacuum. In this case U can be parametrized as

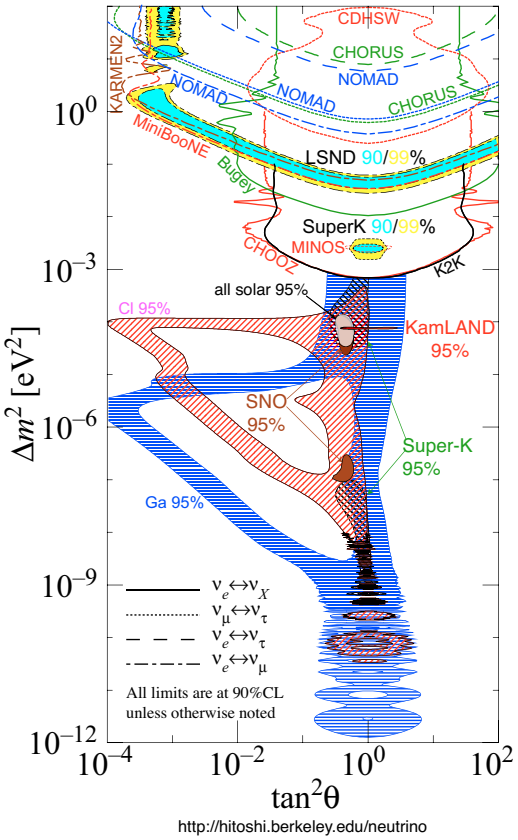

Figure 2.1: The regions of squared-mass splitting and mixing angle favoured or excluded by various experiments. References to the data used in the figure can be found at `http://hitoshi.berkeley.edu/neutrino`.

$$U = \begin{bmatrix} c_{12}c_{13} & s_{12}c_{13} & s_{13}e^{-i\delta} \\ -s_{12}c_{23} - c_{12}s_{23}s_{13}e^{i\delta} & c_{12}c_{23} - s_{12}s_{23}s_{13}e^{i\delta} & s_{23}c_{13} \\ s_{12}s_{23} - c_{12}c_{23}s_{13}e^{i\delta} & -c_{12}s_{23} - s_{12}c_{23}s_{13}e^{i\delta} & c_{23}c_{13} \end{bmatrix} \times diag(1, e^{i\frac{\alpha_{21}}{2}}, e^{i\frac{\alpha_{31}}{2}})$$

where $c_{ij} = cos\theta_{ij}$, $s_{ij} = sin\theta_{ij}$, the angles $\theta_{ij} = [0, \pi/2]$, $\delta = [0, 2\pi]$ is the Dirac CP violation phase and α_{21}, α_{23} are the two Majorana phases. The existing neutrino oscillation data (see figure 2.1) allow to determine the parameters on matrix U. Solar ν_e and the dominant atmospheric oscillation $\nu_\mu \longrightarrow \nu_\tau$ give:

1. $\Delta m^2_{21} \cong 7.65 \times 10^{-5} eV^2$
2. $sin^2\theta_{12} \cong 0.304$

3. $| \Delta m^2_{31} | \cong 2.40 \times 10^{-3} eV^2$
4. $sin^2 2\theta_{23} \cong 1$
5. $sin^2 \theta_{13} < 0.056$

These results imply that:

1. $\Delta m^2_{21} \ll | \Delta m^2_{31} |$
2. $\theta_{23} \cong \pi/4$
3. $\theta_{12} \cong \pi/5.4$
4. $\theta_{13} < \pi/13$

The oscillation data do not allow to determine the sign of $\Delta m^2_{31(32)}$. Correspondingly, two types of neutrino mass spectrum are possible:

- *with normal ordering*: $m_1 < m_2 < m_3$, $\Delta m^2_{31} > 0$, $\Delta m^2_{21} > 0$, $m_{2(3)} = (m_1^2 + \Delta m^2_{21(31)})^{1/2}$
- *with inverted ordering*: $m_3 < m_1 < m_2$, $\Delta m^2_{31} < 0$, $\Delta m^2_{21} > 0$, $m_2 = (m_3^2 + \Delta m^2_{23)})^{1/2}$, $m_1 = (m_3^2 + \Delta m^2_{23} - \Delta m^2_{21})^{1/2}$

So neutrino mass spectrum can be with :

- *normal hierarchical (NH)*: $m_1 \ll m_2 < m_3$
- *inverted hierarchical (IH)*: $m_3 \ll m_1 < m_2$
- *quasi-degenerate (QD)*: $m_1 \cong m_2 \cong m_3 \equiv m_0$, $m^2_{ij} \gg | \Delta m^2_{21,31} |$, $m_0 \gtrsim 0.10 eV$

All three types of spectrum are compatible with the existing data. For the observation of neutrinos from astrophysical sources the oscillations during the source-Earth journey, can be in general taken into account. In this case, the equipartition between the three leptonic flavours $N_{\nu_e} : N_{\nu_\mu} : N_{\nu_\tau} = 1 : 1 : 1$ is expected at the Earth.

2.2 Detection principle

The detection of high energy neutrinos is severely constrained by the fact that the neutrino interaction cross-sections are very low, therefore very large detectors are needed. Underground laboratories would be too small, so the use of large volumes of sea/lake water or antarctic ice was proposed for the first time by Markov in 1960 [59]. The basic idea for a neutrino telescope is to build a matrix of light detectors inside a transparent medium. This medium, such as deep ice or water, offers large volume of free target for neutrino interactions and provides shielding against secondary particles produced by CRs, acting as a scintillator. Moreover it allows transmission of Cherenkov photons emitted by relativistic particles produced by the neutrino interaction. High energy neutrinos interact with a nucleon N of the nucleus, via either charged current (CC) weak interactions (reactions 2.10) or neutral current (NC) weak interactions (reactions 2.11).

$$\nu_l + N \longrightarrow l + X \tag{2.10}$$

$$\nu_l + N \longrightarrow \nu_l + X \tag{2.11}$$

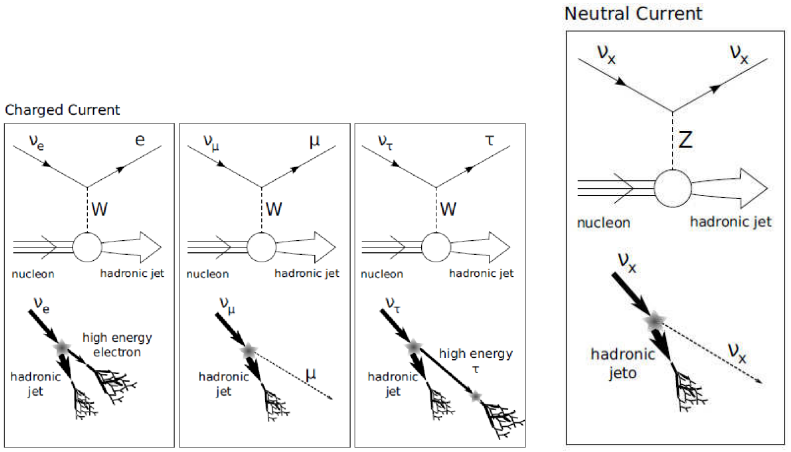

(a) *Charged current (CC)*

(b) *Neutral current (NC)*

Figure 2.2: Different types of neutrino interactions.

2.2.1 Neutral current reactions

The exchange of a neutral boson Z_0 or γ (equations 2.11) gives the same signature for all neutrino flavours. In this channel, a part of the interaction energy is always carried away unobserved by the outgoing neutrino, and therefore the error on the reconstructed energy of the primary neutrino increases accordingly. Even though electromagnetic and hadronic showers are different from each other in principle, the ν_e CC and the ν_l NC channels are not distinguishable in reality, because any HE-neutrino detector is too sparsely instrumented.
The dominant secondary particles in a hadronic shower are pions; kaons, protons or neutrons occur in variable fractions. Muons (from pions decay) can be present as well: they usually leave the shower producing long tracks. Monte Carlo simulations shows that above 1 TeV of shower energy, the largest part of the Cherenkov light is generated by EM sub-showers. For what concerns the measurement of the incoming neutrino direction, the angular difference between the shower and the neutrino falls below 2° for energies above 1 TeV. It is thus negligible with respect to the precision of the shower direction measurement.

2.2.2 Charged current reactions

At high neutrino energies the differential cross section for CC interactions (equations 2.10) is:

$$\frac{d^2\sigma_{\nu N}}{dxdy} = \frac{2G_F^2 m_N E_\nu}{\pi} \frac{M_W^4}{(Q^2 + M_W^2)^2} [xq(x, Q^2) + x(1-y)^2 \bar{q}(x, Q^2)] \quad (2.12)$$

where Q^2 is the square of the momentum transferred between the neutrino and the lepton,m_N and M_W are the masses respectively of nucleon and of the charged boson W, G_F is the Fermi coupling constant and $q(x, Q^2)$ and $\bar{q}(x, Q^2)$ are the parton function distributions for quarks and antiquarks. x and y are the so-called scale variables or Fenyman-Bjorken variables given by :

$$\begin{aligned} x &= Q^2/2m_N(E_\nu - E_l) \\ y &= (E_\nu - E_l)/E_\nu \end{aligned} \quad (2.13)$$

In figure 2.4 the Bjorken variable y as function of neutrino energy is shown. Cross section at energy below 350GeV for $\nu - N$ and $\bar{\nu} - N$

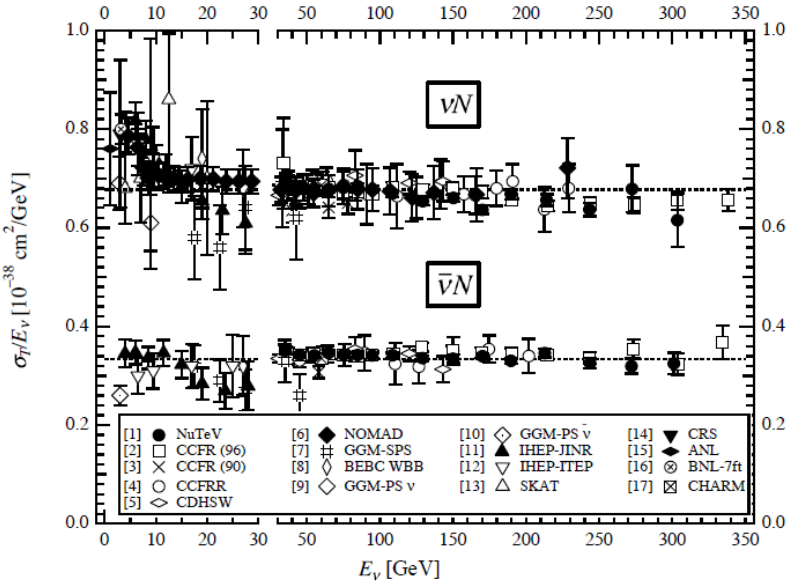

Figure 2.3: σ_T/E_ν for the muon neutrino and anti-neutrino charged-current total cross section as a function of neutrino energy. The error bars include both statistical and systematic errors. The straight lines are the isoscalar-corrected total cross-section values averaged over 30-200 GeV as measured by the experiments in Refs. [60, 61] : $\sigma^{\nu Iso}/E_\nu = (0.677 \pm 0.014) \times 10^{-38} cm^2/GeV$; $\sigma^{\bar{\nu} Iso}/E_{\bar{\nu}} = (0.334 \pm 0.008) \times 10^{-38} cm^2/GeV$. The average ratio of the anti-neutrino to neutrino cross section in the energy range 30-200 GeV is $\sigma^{\bar{\nu} Iso/\sigma^{\nu Iso}} = 0.504 \pm 0.003$ as measured by Refs [60, 61] . Note the change in the energy scale at 30 GeV. (Courtesy W. Seligman and M.H. Shaevitz, Columbia University, 2010)

is given in figure 2.3. For higher energies, the invariant mass $Q^2 = 2m_N E_\nu xy$ could be larger than the W-boson rest mass, reducing the increase of the total cross-section. Since there is no data which constrain the structure functions at very small x, outside the range measured with high precision at the HERA collider, a 10% uncertainty is estimated on the total cross-section at $E_\nu \sim 100PeV$. From 10^{16} to 10^{21} eV the total cross section can be expressed by [62] (see also figure 2.5):

$$\begin{aligned} \sigma_{\nu N} &\simeq 5.53 \times 10^{-36} \left(\frac{E_\nu}{1GeV} \right)^{0.363} cm^2 \\ \sigma_{\bar{\nu} N} &\simeq 5.52 \times 10^{-36} \left(\frac{E_{\bar{\nu}}}{1GeV} \right)^{0.363} cm^2 \end{aligned} \tag{2.14}$$

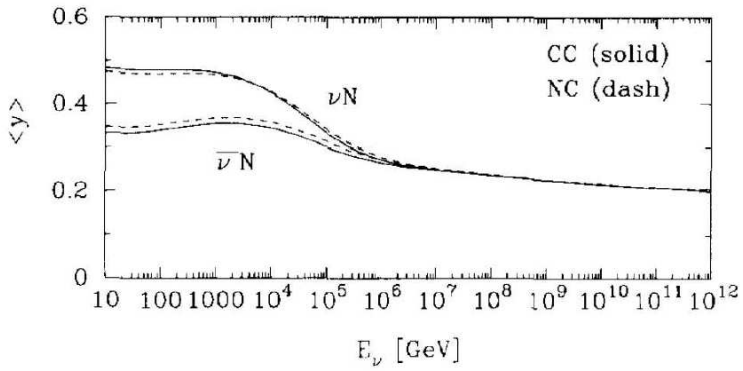

Figure 2.4: Behaviour of the mean value of Bjorken variable y as function of neutrino energy. For values up than 10^{15} eV the fraction of energy given to the hadronic component is between 20% and 25% that of the primary neutrino energy [63].

The increase of the interaction cross-section with neutrino energy makes the effective area of the detector larger at high energies.
Three kind of CC reactions came from 2.10; let's analyse them.

Electron neutrinos $\nu_e + N \longrightarrow e + X$

High energy electron neutrinos deposit 0.5-0.8% of their energy into an electromagnetic shower, initiated by the electron produced in the final state of the charged current interactions with nucleons of the medium surrounding the detector. The rest of the energy goes into the fragments of the target, that produce a second subdominant shower. The signature of electrons propagating through a neutrino telescope is that of a moving sphere-like surface, whose radius increases with the shower energy. Because the shower and its accompanying Cherenkov light are not totally symmetric, but elongated in the direction of the electron (and incident neutrino), its direction can be reconstructed. Pointing accuracy is however poorer than what can be achieved with muon neutrinos. On the other hand the energy reconstruction for ν_e induced charged current events is more accurate than ν_μ and the background of atmospheric neutrinos is significantly reduced, since at higher energies atmospheric muons reaction is less probable, reducing the content of high energy ν_e .

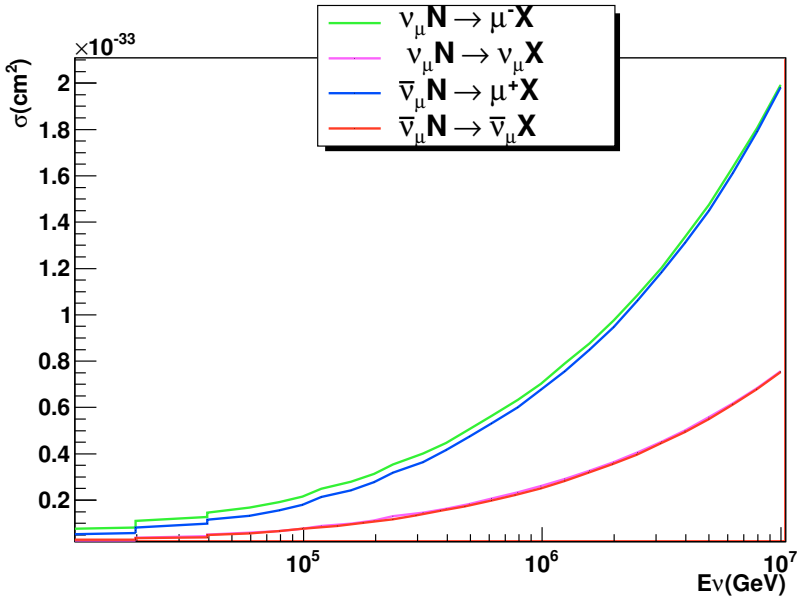

Figure 2.5: Cross sections for reactions 2.10 and 2.11

Tau neutrinos $\nu_\tau + N \longrightarrow \tau + X$

Usually tau has three kind of reactions. Two of these are like muon and electron neutrino CC reactions

$$\tau^+ \longrightarrow \mu^+ + \nu_\mu + \bar{\nu}_\tau \quad \tau^- \longrightarrow \mu^- + \nu_\tau + \bar{\nu}_\mu \text{ (BR = 17.36\%)} \tag{2.15}$$

$$\tau^+ \longrightarrow e^+ + \nu_e + \bar{\nu}_\tau \quad \tau^- \longrightarrow e^- + \nu_\tau + \bar{\nu}_e \text{ (BR = 17.85\%)} \tag{2.16}$$

or through an hadronic decay:

$$\tau^- \longrightarrow \nu_\tau + hadrons \quad \tau^+ \longrightarrow \bar{\nu}_\tau + hadrons \tag{2.17}$$

For the decays 2.16 and 2.17 and τ energies above some TeV, the showers from primary reaction and τ decay are separated in space and may be resolved ("double-bang signature"). τ neutrinos which interact producing a τ lepton generate another τ neutrino when the tau lepton decays, thus only degrading the energy of the neutrino. Below a few PeV, the Lorentz factor is such that the τ lepton travels a short distance before decaying. Than for the detection of this neutrino flavour an high resolution energy detector is needed. By the way a short path from the production to the decay point implies that the two showers cannot be distinguished. "Lollypop" events occur when only the second shower

produced in the double bang develops within the detector volume, and a τ lepton track is identified entering the shower over several hundreds meters. Below several PeV energies, τ tracks are not long enough to be identified.

Muon neutrinos $\nu_\mu + N \longrightarrow \mu + X$

This is the "golden channel" for point source searches (neutrino astronomy) and produce muon and an hadronic shower. With neutrino energies higher than $\sim 1TeV$ the interaction occur outside the detector volume, while in most cases muons are energetic enough to completely traverse the detector. This gives a clean experimental signal which allows accurate reconstruction of muon direction, closely correlated with the neutrino direction. The relation between neutrino and muon directions is essential for the concept of a neutrino telescope. Since neutrinos are not deflected by galactic magnetic fields, it is possible to trace the muon back to the neutrino source. This is equivalent to traditional astronomy where photons point back to their source. At these energies, the average angle between the incident neutrino and the outgoing muon can be approximated by:

$$\theta_{\nu\mu} \simeq \frac{0.6^\circ}{E_\nu[TeV]} \tag{2.18}$$

where E_ν is the neutrino energy in TeV. Muons loose energy in matter via several mechanism (see figure 2.6 for the differential muon energy loss per meter of water equivalent (m.w.e)[1]).

1. *ionization of matter* is the dominant process of muon energy loss at low energies (below 1 TeV) and producing atomic excitations and ionizations of matter during its transverse.

2. *pair* e^+e^- *production* is the dominant energy loss process at energies of about 1 TeV and implies the annihilation of muon interacting with medium into e^+e^-.

3. *bremsstrahlung* charged particles emit radiation in the presence of an electromagnetic field giving rise to a deceleration. Concerning muon propagation in a dense medium, this deceleration

[1] 1 m.w.e of any material (such as rock, gravel, etc.) is a thickness of that material providing shielding equivalent to one meter of water.

is produced by the electromagnetic interaction with nuclei and electrons of surrounding atoms.

4. *photo-nuclear interactions* muons exchange a virtual photon with a nucleus of surrounding medium.

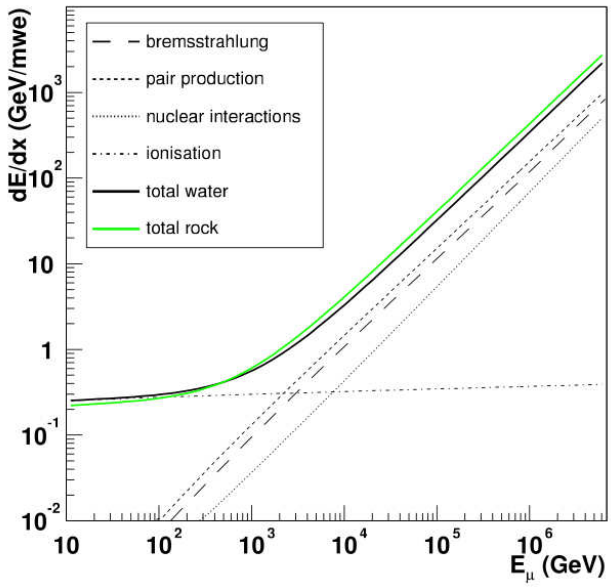

Figure 2.6: Average energy loss per m.w.e. for muons in sea water as a function of the muon energy.

The total energy loss for high energy muons is according to:

$$\frac{dE}{dx} = -\alpha(E) - \beta(E)E \tag{2.19}$$

At high energies as a first approximation, the ionisation term α and the radiative loses term β can be considered as energy independent[2]. With equation 2.19 it's possible compute the muon range R and its energy threshold E^{th} (see also figure 2.7):

$$R = \frac{1}{\beta} ln\left(1 + \frac{E_\mu \beta}{\alpha}\right) \tag{2.20}$$

[2]In water $\alpha \simeq 2.67 \times 10^{-3} GeV g^{-1} cm^{-2}$ and $\beta \simeq 3.40 \times 10^{-6} g^{-1} cm^{-2}$, for $30GeV < E_\mu < 35TeV$

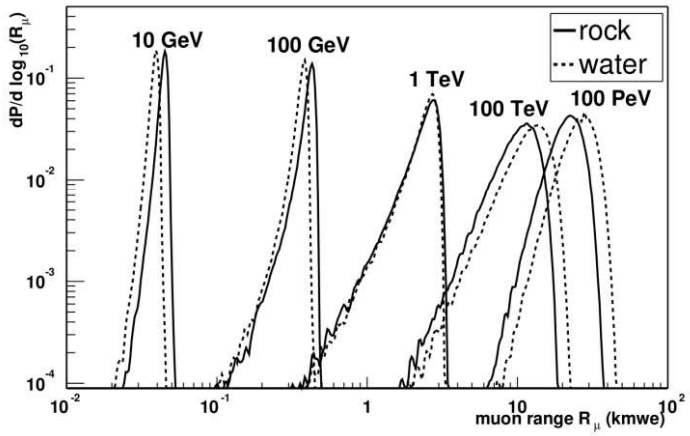

Figure 2.7: Distribution of the muon range in rock and water for different muon energies, expressed in (m.w.e.).

2.3 Muon neutrinos detection

In section 2.2.2, has been explained how muon neutrinos can interact with matter at different energies. In the range of energies up to 100 GeV the detection of muon neutrinos is the "golden channel" for neutrino astronomy so a more detailed explanation will be reported in the following subsections. What we want to measure is the direction of secondary particles (muons) from the arrival times of the Cherenkov light that they emit in the sea water.

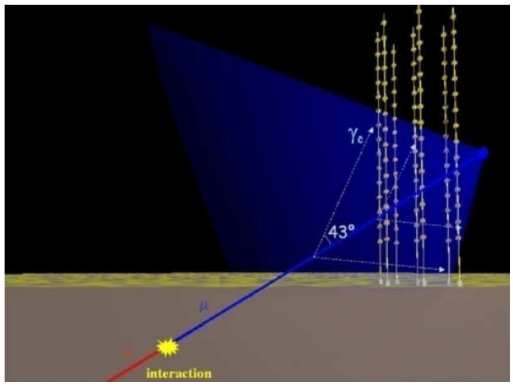

Figure 2.8: Principle of detection of an HE ν_μ in an underwater neutrino telescope. Red line is the muon that interact in yellow dot and creates a ν_μ (blue line). The Cherenkov cone has a typical angle of about 43°.

2.3.1 Cherenkov radiation

In general one of the mostly important identification methods for HE particles is based on Cherenkov effect. When a charged particle with velocity v transverse a dispersive medium of refractive index n, excited atoms in the vicinity of particle become polarized and if v is greater than the speed of light in the medium c/n, a part of the excitation energy reappears as coherent radiation emitted at a characteristic angle θ to the direction of the motion (see figure 2.8). The necessary condition is

$$v > \frac{c}{n} \tag{2.21}$$

and can be represented with the Huygen's construction of figure 2.9,

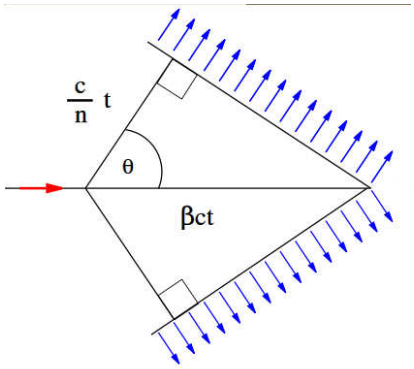

Figure 2.9: Longitudinal section of the Cherenkov light cone. Blue arrows are the wave front of photons

which also implies

$$\cos\theta = \frac{1}{\beta n} \tag{2.22}$$

with $\beta = v/c$. Cherenkov radiation appears as a continuous spectrum and may be collected on to a photosensitive detector. Its main limitation from the point of view of particle detection is that so few photons are produced. The number of Cherenkov photons, N_λ , emitted per unit wavelength interval, $d\lambda$ and unit distance travelled, dx, by a charged particle of charge e is given by:

$$\frac{d^2N}{dxd\lambda} = \frac{2\pi}{137\lambda^2}\left(1 - \frac{1}{n^2\beta^2}\right) \tag{2.23}$$

where λ is the wavelength of the radiation. From this formula it can be seen that the Cherenkov radiation gives a significant contribution at shorter wavelengths. Typically, in the wavelength range between 300-600 nm (blue-violet), the number of Cherenkov photons emitted per meter is about 3.5×10^4 in sea water.

2.3.2 Physical background

Cosmic neutrino detectors are not background free. In figure 2.10 signal neutrinos transverse the Earth and emit a secondary particle but there are two kind of background. Showers induced by interactions

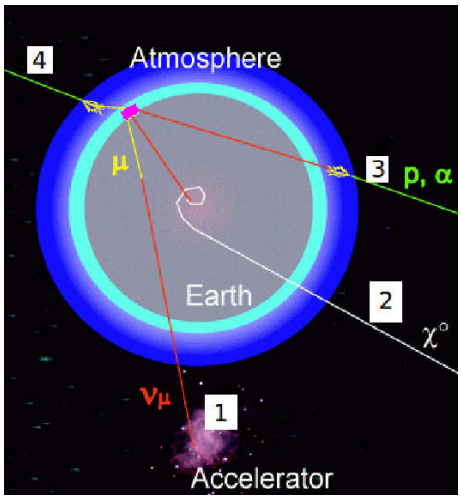

Figure 2.10: Schematic view of origin of atmospheric muons and neutrinos. Signal neutrinos (1: cosmic ν, 2: dark matter ν) transverse the Earth and emit a secondary particle that reach the detector (pink). The background is due to (3) atmospheric neutrinos and (4) atmospheric muons

of cosmic rays with the Earth's atmosphere produce the so-called atmospheric muons and atmospheric neutrinos. Atmospheric muons can penetrate the atmosphere and up to several kilometres of ice/water. Neutrino detectors must be located deeply under a large amount of shielding in order to reduce the background. The flux of down-going atmospheric muons exceeds the flux induced by atmospheric neutrino interactions by many orders of magnitude, decreasing with increasing detector depth (figure 2.11*a*). Neutrino telescopes, contrary to usual optical telescopes, look downward. Up-going muons can only

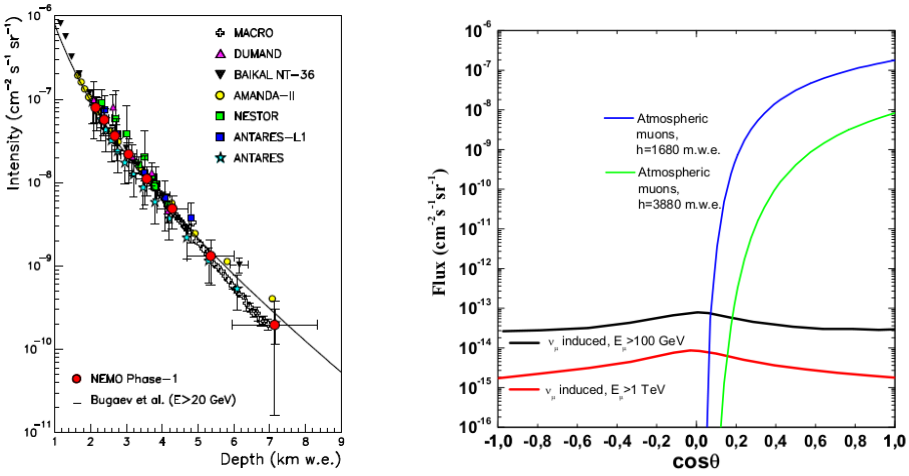

(a) (b)

Figure 2.11: *(a)*: Atmospheric muon flux as a function of slant depth measured with the NEMO Phase-1 detector [67]. *(b)*: Different contributions (as a function of the cosine of the zenith angle) of the atmospheric muons for two different depths; and of the atmospheric neutrino induced muons, for two different muon energy thresholds.

be produced by interactions of (up-going) neutrinos. From the bottom hemisphere, the neutrino signal is almost background-free (figure 2.11*b*). Only atmospheric neutrinos that have traversed the Earth, represent the irreducible background for the study of cosmic neutrinos. They come from an HE charged primary CR that interacting with atmosphere gives a neutrino and an hadronic shower, transferring the majority of its energy to neutrino (look in figure 2.10 track 3).

2.3.3 Environmental background in the telescope

Physical background in the detector has been explained but there are two other sources of background and they depend on the environment: Cherenkov light produced in the propagation of charged particles originating in the decay of radioactive elements in sea water and luminescence induced by biological organisms, the so called bioluminescence.

Radioactivity

Several radioactive elements can be found in sea water, the most abundant is the ^{40}K, that has two main decay channels:

$$^{40}\mathrm{K} \longrightarrow ^{40}\mathrm{Ca} + e^- + \bar{\nu}_e \ \mathrm{B.R} = 89.3\% \tag{2.24}$$

$$^{40}\mathrm{K} + e^- \longrightarrow ^{40}\mathrm{Ar} + \nu_e + \gamma \ \mathrm{B.R} = 10.7\% \tag{2.25}$$

The electrons produced in the first process often have sufficiently high energy to induce the Cherenkov effect, while in the electron capture process, the photon in final state is produced with an energy of 1.46 MeV, which can easily lead to the production of electrons with energies over the threshold for Cherenkov light emission. Light pulses due to ^{40}K decays have low amplitude (mostly 1 p.e.[3]) and are uncorrelated on time scale of a few nanoseconds. However radioactive decays may produce many photons within 1 ns, giving raise to higher amplitudes on a single photomultiplier tube (PMT) or narrow coincidences on neighbouring PMTs.

Bioluminescent organisms

There are two contributions to bioluminescent light, one varying on time scales of hours to days (presumably from bacteria) and one coming in "bursts" with durations of a few tenths to a few tens of seconds (assigned to larger organisms). The photomultiplier count rate from the steady component can be of similar size as that from ^{40}K and is typically homogeneous over the full detector; a burst can cause rates that are larger by orders of magnitude, but affect only a local group of optical modules. Both components thus differ significantly in their impact on data taking, filtering and analysis . The most direct assessment of bioluminescence and its impact on the neutrino telescope is by measuring the intensities of deep-sea background light over long-term periods. To investigate the occurrence of bioluminescent organisms, water samples have been retrieved from different depths at a location near the Capo Passero site. Subsequently, the density of luminescent bacteria cultivatable at atmospheric pressure has been determined. The results are if figure 2.12 indicate that such bacteria are essentially absent at depths beyond 2500 m [72].

[3] "photo-electron"

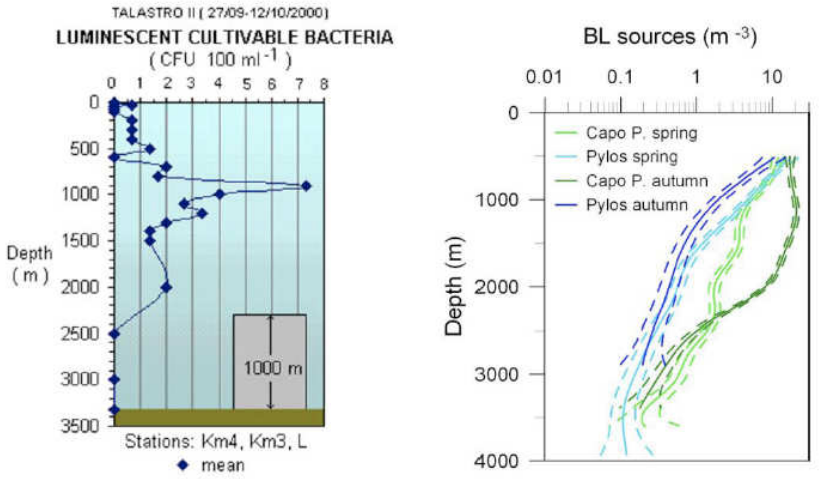

Figure 2.12: Left: Concentration of luminescent bacteria cultivatable at atmospheric pressure, as a function of depth. The data have been obtained from water samples taken at the Capo Passero site. Right: Density of bioluminescent animals at the Capo Passero and Pylos sites, in autumn 2008 and spring 2009. (Dashed lines show 95% c.l.)

2.3.4 Light transmission properties

Light absorption provides an upper limit to the distance between two sensors, which are used to search for time coincidences due to Cherenkov photons produced by the same muon track. In order to properly describe the transparency of sea water as a function of wavelength, it is necessary to measure the parameters describing absorption and scattering, such as the absorption length $\lambda_{abs}(\lambda)$ scattering length $\lambda_s(\lambda)$ and attenuation length $1/\lambda_{att}(\lambda) = 1/\lambda_{abs}(\lambda) + 1/\lambda_s(\lambda)$. Each of these lengths represents the path after which a beam of initial intensity I_0 and wavelength λ is reduced in intensity by a factor of $1/e$ through absorption, scattering or both according to

$$I_{abs,s,att}(x) = I_0 exp\left(-\frac{x}{\lambda_{abs,s,att}}\right) \tag{2.26}$$

where x is the optical path traversed by the beam. In the literature, also the coefficients of absorption,$a = 1/\lambda_{abs}(\lambda)$, and scattering, $b = 1/\lambda_s(\lambda)$, are used to characterise the light transmission through matter. The sum of scattering and absorption coefficients is called "attenuation coefficient" c. The light transmission at the Capo Passero

site has been investigated [73] using a setup including a commercial instrument (the AC9 by WETLABS) capable of measuring, in a collimated geometry, the absorption and the attenuation coefficients for nine wavelengths ranging from 410 nm to 715 nm. The values of the absorption and attenuation lengths have been determined for each measurement by averaging the data for depths greater than 2850 m [74]. The results of four sets of measurements taken in different seasons are shown in figure 2.13. For comparison, light absorption and attenuation

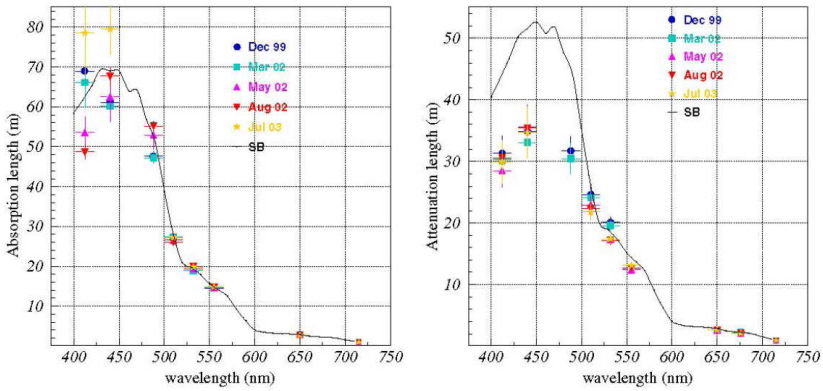

Figure 2.13: Absorption length (left panel) and attenuation length (right panel) measured at the Capo Passero site at four seasons. Also indicated are the the values for optically clean salt water (black lines). Figure taken from [73].

data for optically pure sea water are also shown in figure 2.13. At all wavelengths, deep waters at that location have an absorption length compatible with that of pure sea water. There is no evidence of a seasonal dependence of the optical parameters. The transmission length for Cherenkov photons measured at Capo Passero site is about 70 m.

2.4 Cherenkov high energy neutrino detectors

After the pioneering experience made by the DUMAND Collaboration off-shore Hawai Island [64], Baikal was the first neutrino telescope operating underwater.
The Baikal Neutrino Telescope (NT) is operated in Lake Baikal (Siberia, Russia) where the detector is moored between 1000 and 1100 m depth [65]. Baikal NT200+3 is an umbrella-like array with a 72 m height and a diam-

eter of 43 m. It is made of 8 strings, each with 24 pairs of down-looking Optical Modules (OM). Each OM contains a 37 cm quasar photomultiplier. The two OMs of a pair operate in coincidence in order to suppress the background due to bioluminescence. Baikal NT200 is a high granularity detector with an energy threshold of 15 GeV.
Beyond these first projects of neutrino detectors, we have to focus mainly on the following projects.

2.4.1 Icecube and AMANDA

On the other hemisphere, the AMANDA detector, constructed at the Amundsen-Scott South Pole Station was completed in 2001 [66]. AMANDA was a first-generation instrument that served as test bench for technologies and as prototype for the km3 size detector IceCube. AMANDA Collaboration has been the first to use ice instead of water as natural radiator, for the realization of a neutrino telescope, located 1 mile deep-ice. In AMANDA, holes have been drilled in ice, and PMTs have been deployed inside. The detector has been operated for more than 5 years in its final configuration of 680 optical modules on 19 strings.
The history of IceCube (figure 2.14) started with AMANDA, the predecessor and prototype for IceCube, but it is no longer operating. IceCube is able to detect neutrinos from 100GeV to more than 10^9 GeV. When completed in austral summer season 2010-2011, the in-ice components of IceCube, the IceCube Array, will consist of 86 strings, including 6 strings forming DeepCore. In total 5160 so called Digital Optical Modules (DOMs) are installed on these vertical stings (installed via hot water drill) at a depth of between 1450m and 2450m in the South Pole ice sheet. At one string 60 DOMs are located. The electronics to digitize, time stamp and transmit signals to the central data acquisition system is located in the IceCube laboratory on the snow surface Neutrino telescopes located at the South Pole do not cover the Southern sky, which is obscured by the large flux of cosmic ray muons, as can be seen in figure 1.4 , showing the region of the sky which is visible to a neutrino telescope in both the Northern and Southern hemispheres. This aspect provides compelling arguments for the realization of cubic-kilometer scale detectors in the Northern hemisphere. Extensive efforts have

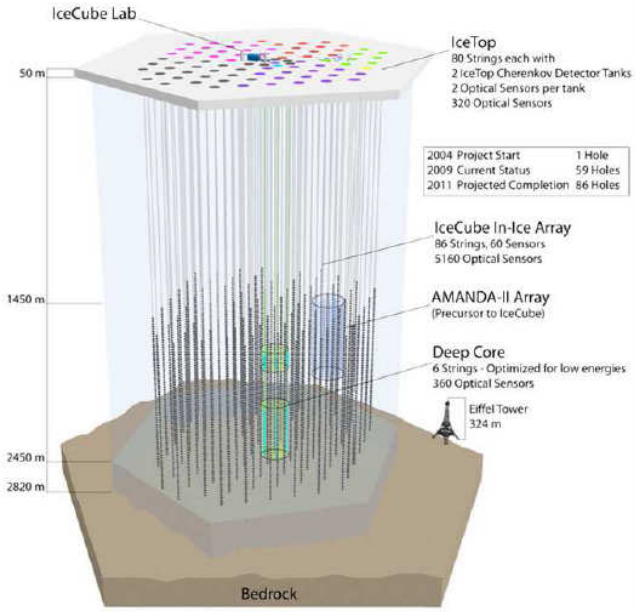

Figure 2.14: Pictorial view of the IceCube detector.

been devoted by three European Collaborations to the realization of a deep underwater cosmic neutrino detector in the Mediterranean sea.

2.4.2 NEMO

The NEMO[4] Collaboration [68] has developed ad-hoc technological solutions for the design and realization of both a dedicated mechanics and electronics, in the view of a cubic-kilometre scale experiment. The NEMO Phase-I lead to the deployment of a prototype structure in a test-site at 2000 m depth, offshore Catania, Italy. The prototype had a dedicated mechanic setup, PMTs being located on a aluminium tower (figure 2.15), together with electronics and data acquisition system.

2.4.3 The ANTARES neutrino telescope

The ANTARES[5] detector is located at a depth of 2475 m in the Mediterranean Sea, 42 km from La Seyne-sur-Mer in the South of France. A schematic view of the detector layout is shown in figure

[4]NEutrino Mediterranean Observatory
[5]Astronomy with a Neutrino Telescope and Abyss environmental RESearch

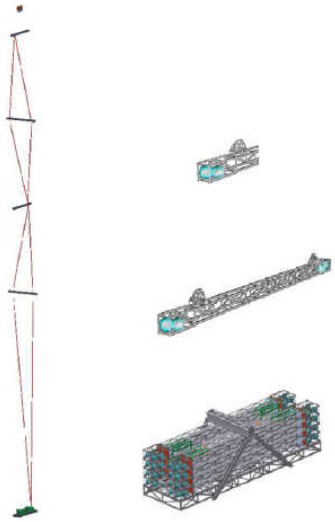

Figure 2.15: The NEMO tower. The length of each storey (floor) is 12 m and the inter-storey distance is 40 m. Thanks to the modular design of the tower, these parameters can be modified.

2.16. The infrastructure has 12 mooring lines holding light detectors designed for the measurement of neutrinos based on detection of the Cherenkov light emitted in water. Instruments for research in marine and Earth science are distributed on the 12 optical detector lines and are also located on a further 13th line specifically dedicated to monitoring of the sea environment. The elementary detection unit is the Optical Module (OM) which consists of a glass sphere housing a photomultiplier tube (PMT) [77]. The three-dimensional telescope matrix is made of groups of three OMs called storeys. Three OMs are mounted in the Optical Module Frame (OMF), a mechanical structure which also supports a titanium container, the Local Control Module (LCM), housing the offshore electronics and processors. A detector line is formed by a chain of 25 OMF linked by Electro- Mechanical Cable segments(EMC), 12.5 m long from storey to storey and 100 m long from the bottom to the first storey. The line is anchored on the sea bed with the Bottom String Socket (BSS) and is held vertical by a buoy at the top. The full neutrino telescope has 12 such lines arranged on the sea bed in an octagonal configuration.

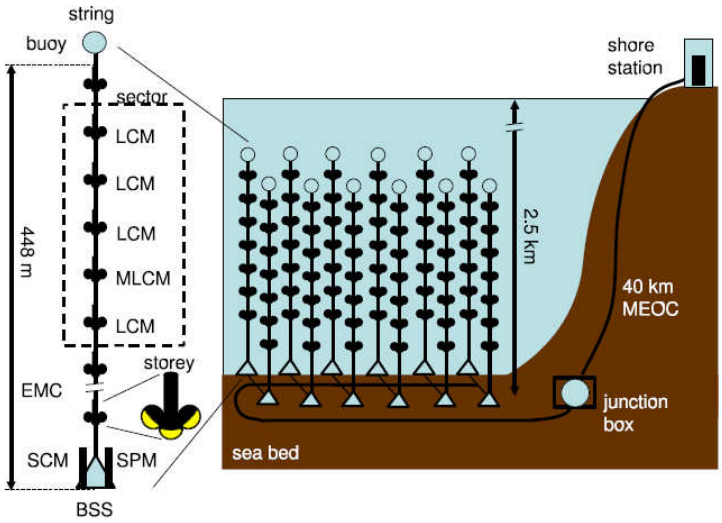

Figure 2.16: A schematic view of the ANTARES detector layout. The main elements of the ANTARES detector are outlined in the figure. The active part of the detector are the photomultiplier tubes (PMTs) grouped in triplets in each storey. Each of the 12 lines of the detector has 25 storeys.

2.4.4 Other detection techniques

The following techniques are applied to the very low energy neutrino events.

Acoustic detection

Detectable acoustic signals are expected to be produced by neutrino-induced cascades propagating in a medium. The energy cascade deposition occurs instantaneously, so that an immediate heating of the medium is produced. This increasing of temperature produce a pressure wave that can be detected by hydrophones. The typical bipolar shape as a function of time it's remarkable sign of these cascades. This kind of experiments needs of very large instrumented volume (>100 km^3) and now there are only prototypes of experiment [69].

Radio detection

Ultra high energy protons can interact with the Cosmic Microwave Background radiation (CMBR), as demonstrated by both HiRes and Auger experiments. As a consequence of these interactions, ultra high

energy neutrinos from pion decay should be produced, and their clear detection would provide a crucial input to the field. The energies of these UHE neutrinos are up to 100 PeV and are needed detectors of the order of 1 kilometre-cube scale to detect these very low fluxes. The implementation of radio and acoustic solutions for high energy neutrino detection represents the next-to-next generation of telescopes together with the Cherenkov technique. Radio detection technique can be applied to ultra high energy neutrinos, since the emitted radiation can reveal electromagnetic showers produced in charged current neutrino interactions. Radio signal induced by the Cherenkov effect has been observed for cascade-like events in sand, salt and in ice. While radio signals due to cascades are likely to be detected, the corresponding signal induced by muons is too faint. Several experiment like RICE [70], ANITA, FORTE and GLUE are exploring this new feature.

Chapter 3

The KM3NeT high energy neutrino telescope

From the three collaboration ANTARES [2], NEMO [67], NESTOR [4] have joined their strength into the KM3NeT[1] consortium [3]. KM3NeT is a deep-sea multidisciplinary observatory in the Mediterranean Sea that will provide innovative science opportunities spanning Astroparticle Physics and Earth and Sea Science. This is possible through the synergy created by the use of a common infrastructure allowing for long term continuous operation of a neutrino telescope and marine instrumentation. In figure 3.1 a pictorial view of the detector is shown togheter with the KM3NeT tower model. The consortium has been financed from European Union and involves 40 institutes of 10 different countries. The "technical design report" [3] with the whole technical description of the experiment is just published. There are three candidate sites in the Mediterranean area:

- Toulon(France)[2] at a depth of 2475 m and cable length to shore 40 km proposed by ANTARES collaboration.
- Pylos(Greece)[3] three possible sites at a depth of 5200,4500 and 3750 m in Ionian Sea proposed by NESTOR collaboration.
- Capo Passero(Italy)[4] in Ionian Sea at 3500 m of depth proposed

[1] KM3 Neutrino Telescope
[2] 42°48′N 06°10′E
[3] 36°33′N 21°08′E,36°33′N 21°29′E, 36°38′N 21°35′E
[4] 36°16′N 16°06′E

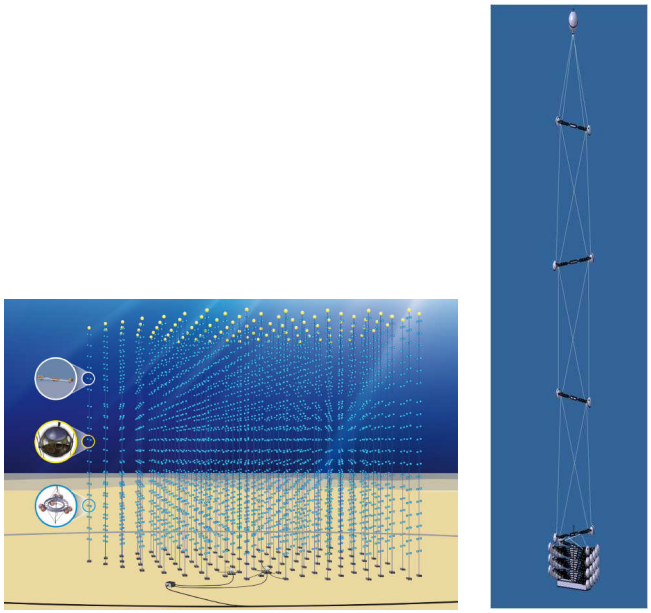

(a) *Artistic view of detector*

(b) *Deployed tower KM3NeT*

Figure 3.1: Artistic view of detector and the deployed tower KM3NeT

by NEMO collaboration.

In this chapter have been discussed the technical implementation of the generic structure of a neutrino telescope.

- *Photomultipliers (PMT)* The neutrino telescope will consist of a three-dimensional array of photo-sensors (photomultipliers) supported by vertical structures anchored on the seafloor and connected to a seabed cable network for power distribution and data transmission. To obtain the large photocathode area required for the planned sensitivity in a cost-effective way, it is optimal to arrange photomultipliers in local clusters. This objective can be achieved by using either local groups of optical modules containing one or two large photomultipliers each or groupings of smaller photomultipliers within a single multiPMT optical module.

- *Detection Unit* The reference detector for the simulations consists of two multi-PMT optical modules on a bar. The detection unit

consists of a number of storeys vertically distributed over a height of several hundreds of meters. The number of detection units (DU) in the simulations is set to 154. Each of these consists of 20 floors, and each floor consists of a bar with one optical module at each end. The distance between the centres of the optical modules can be 6 or 10 m. The distance between floors is 40 m and the position of the lowest floor is 100 m above the seabed. The bars of two neighbouring floors are orthogonal. The distribution of the positions of the detection units on the seabed (the so-called footprint) is roughly circular. The positions are irregular at the level of 20 m. The footprint has a typical density corresponding to an average distance between detection units that can lay from 130m to 180 m.

- *Storeys and Local Control Module* Simulations indicate that horizontal distances of a few meters in local optical module groups increase the reconstruction quality and thus the sensitivity. Therefore, a specific design being proposed and shown in figure 3.2 incorporates extended mechanical structures in the form of 6 meter long horizontal bars to support optical modules. One detection unit consists of 20 such horizontal bars (storeys), with a vertical separation of 40 m between storeys.

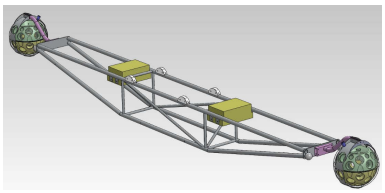

Figure 3.2: Storey

- *The Junction Box and the Main Electro-Optical Cable (MEOC)* The seafloor network will consist of a main electro-optical cable running from the shore to a main junction box in the deep sea and of a network of secondary junction boxes linked by electro-optical cables and connecting to the telescope detection units and the associated sciences nodes (see figure 3.3). Sea bottom connections between the detection units and the cable network are carried out through the use of deep-sea remotely operated vehicles (ROVs).

The overall power consumption of the telescope is approximately 125 kW and the expected data rate will be roughly 25GBytes/s. This large data stream to shore is carried on a fibre optic network which transfers all the optical module data to the shore. A backup solution to the data transmission scheme within a detection unit is a fibre-optic daisy-chain concept.

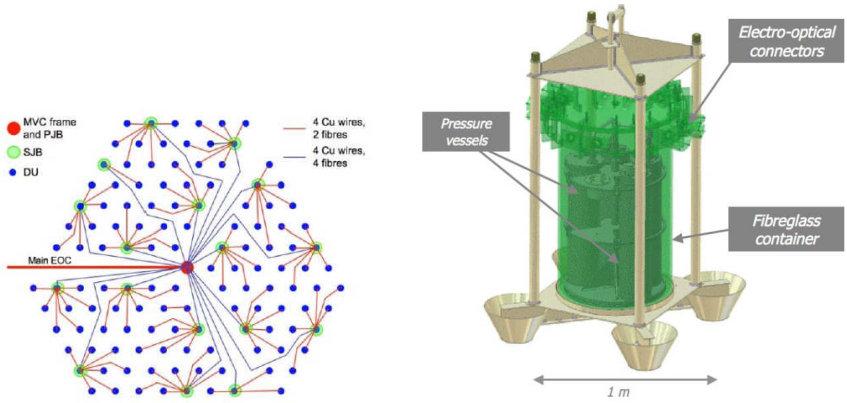

(a) *Seafloor network of the detector* (b) *Junction Box*

Figure 3.3: Seafloor network of the detector and the junction box.

3.1 Optical modules

The multiPMT optical module consists of 31 photomultipliers of 3 inch diameter housed in a 17 inch sphere. This object gives several advantages in confront of the single PMT used by ANTARES detector:

- The total photocathode surface is 1260 cm^2.
- These photomultipliers are not sensitive to the Earth's magnetic field and do not require μ-metal shielding.
- The segmentation of the detection area in the OM will aid in distinguishing single-photon from multi-photon hits.
- With the multiPMT OM two-photon hits can be unambiguously recognized if the two photons hit separate tubes, which occurs in 85% of cases for photons arriving from the same direction.

- The loss of a single photomultiplier will degrade the performance of the OM minimally. Failure rates of small photomultipliers have been determined to be of the order of 10^{-4} per year.
- The photomultipliers run at a gain of 10^6 and their individual photocathode area is small, therefore the integrated anode charge is small.

The optical module (OM) glass vessel houses the photomultiplier and associated equipment, protecting them against the hydrostatic pressure and sea water. These designs are currently being pursued, with a common solution for the front-end electronics that can be housed inside an optical module. A picture of the single OM and the multiPMT is depicted in figure 3.4. The PMT has a diameter of 76 mm, roughly

(a) *single OM* (b) *multiPMT*

Figure 3.4: Left:OM and its component. Right: multipmt

corresponding to 3 inch. The quantum efficiency (QE) is the probability that a photon generates a photoelectron inside the PMT. QE as a function of the wavelength of the photon is presented in figure 3.5. The optical transmittance of the glass sphere and the gel is usually included in the QE of the PMT; a thickness of 1.4 cm is assumed for the glass and 0.2 cm for the gel. The collection efficiency of the PMT is assumed to be 90%. The angular acceptance of the PMT, including the effect of the optical ring, is also presented figure 3.5. The photomultiplier will be

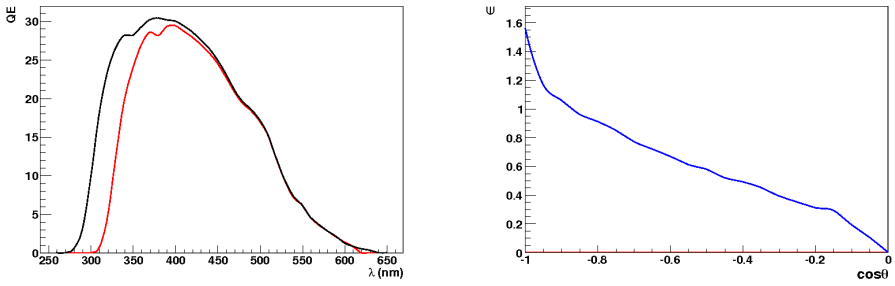

(a) (b) *Behaviour of OM*

Figure 3.5: Left: The QE (unit %) (black line) a function of the wavelength of the photon and QE that includes the optical transmittance of the glass sphere and the gel (red line) . Right: The angular acceptance of the PMT ϵ including the effect of the optical ring (θ is the angle between the incident photon and the axis of the PMT, where $\cos\theta = -1$ corresponds to a head-on angle of incidence).

surrounded by an expansion cone. This cone provides a means of reflecting photons that would normally miss the photocathode, therefore effectively increasing its size.

3.2 Data acquisition system (DAQ)

The main purpose of the readout system of KM3NeT is the conversion of the analogue outputs of the PMTs into formatted data for offline analysis. The deep sea infrastructure will also contain a large number of instruments for various scientific research activities. The operation of these instruments will be incorporated in the general readout system of the infrastructure. The preferred solution for the readout system is one where all (digitised) data are sent to shore, to be processed in real-time.

3.2.1 Trigger

To first approximation, a detectable muon signal is defined by a minimal number of time-position correlated PMT hits[5]. This is referred to as a "trigger".

[5] a hit is defined as a signal above a certain threshold, typically 0.5 p.e.

Many trigger can be defined, but those most used for KM3NeT simulations are:

- level zero (L0)
- level one (L1)

The level zero signal, L0, processing consists of a time-over-threshold discriminator, with an overall timing accuracy of $\sigma = 1.0$ ns, including transit time spread (TTS),the influence in the photon dispersion in water etc. Photon counting is based on counting the number of hits from different PMTs inside the same optical module.
The time window for the level one trigger, L1, is $\Delta t \leqslant 10$ ns (L1 is defined as a local coincidence of two (or more) hits within the same optical module). The directional sensitivity of the PMTs can be used to improve the signal-to-noise ratio of the L1 hits by considering (next-to) neighbouring PMTs only. The results should be evaluated for a simulated trigger based on five (or more) L1 hits due to the signal from a neutrino interaction or atmospheric muon bundles.

3.3 Calibration

Timing calibration is a critical requirement for a real-time readout system. The propagation delay from each storey to the shore will be different due to their unique distances from the shore and due to the fibre's wavelength specific group delay. The precision necessary for the relative timing calibration requirement is specified so as not to degrade the overall accuracy. For a large underwater neutrino telescope the chromatic dispersion of light in water is an intrinsic limitation to the timing precision. It amounts to an uncertainty of $\sigma \sim 2$ ns for light travelling a distance of 50 m. All contributions in the design from PMTs and electronics are less than 2ns and so the timing calibration system is required to have a precision of $\sigma < 1$ ns. As already mentioned, the clock system will distribute the time reference signal required to synchronize all the front end digitizing elements and the reference clock in the shore station. The delay between the arrival of the photon to the photocathode and the time stamping (i.e. the transit time of the PMT plus the one of a part of the front end electronics) will be measured

for all the PMTs before deployment during the on-shore detection unit calibration. These delays together with the clock phases (measured in situ) will enable time calibration of the data coming from different PMTs anywhere inside the detector. After deployment in-situ of the detection units, time calibrations will be performed to make corrections in the calibration constants determined on-shore. Such changes will be necessary to correct for different temperature and for any adjustments of the PMT high voltage. This off-shore time calibration will use four methods:

1. ^{40}K *coincidences*: Cherenkov light emitted in the decays of potassium in the water around the storeys gives coincident signals in nearby PMTs which can be used to determine the relative time offsets.

2. *LED light emitter: "nanobeacon"*: A nanobeacon, containing a small number of LEDs pointing upwards and pulsed by self-triggering electronic circuits, will be mounted on the inner surface of each OM.

3. *Lasers: "laser beacon"* : These laser beacons will enable the relative calibration between several OMs of different detection units. One laser beacon for every six detection units will be sufficient to ensure redundancy of coincident signals. The laser beacons will either be located on the bases of the detection units or on the junction boxes on the sea floors.

4. *upward and downward going muons*: Reconstructed muons can be used to further refine and cross-check the determination of the time constants. For downward going atmospheric muons there is a limitation in the precision achievable due the light scattering needed to reach downward looking PMTs. Upward going muons from atmospheric neutrinos or optical modules with upward looking photomultipliers can be used to avoid this limitation

All these methods are based on the experience gained from the ANTARES project and together, they constitute a redundant and robust timing system, given that each method has its own set of systematic errors.

3.4 Positioning system

The positioning system supplies information for both the installation and operation phases of the project. During the deployment of the detector, the positioning system must provide the position of the telescope's mechanical structures, in a geo-referenced coordinate system, with accuracy of the order of a few metres. This is important both for the safe deployment of the mechanical structures and for the determination of the absolute position and pointing direction of the telescope. During the operation phase, the positioning system must give the positions of the optical modules with the necessary accuracy for the muon tracking. For this requirement the optical module coordinates must be measured, in a local reference system, with accuracy better than 20 cm with a frequency of one measurement per 30 s in order to correct for the movement of the detection units due to the sea currents. The positioning system has four elements:

- acoustic transceivers, anchored on the seabed in known positions in a "Long Base-Line (LBL)" reference system ;
- acoustic receivers (hydrophones) rigidly connected to the telescope's mechanical structures holding the OMs;
- devices (compasses) to measure the orientation of each storey;
- computers on-shore for data analysis.

The KM3NeT positioning system is based on experience of the systems developed for ANTARES [75] and NEMO [76] but with better accuracy due to absolute time synchronization between transceivers and receivers. It is fully integrated with the detector electronics. The components are commercially available and have been tested to 3500 m depth by the pilot projects.

Chapter 4

Monte Carlo simulation and analysis tools

In this chapter the tools that are used to simulate the detector geometry, the neutrino interactions, the light produced by secondary charged particles and the response of the detector are described.
The whole Monte Carlo simulation chain is shown in figure 4.1. The whole simulation package was developed by the ANTARES collaboration and adapted to the km-cube detector at the LNS[1]. There are several packages that generate the primary particles and an intermediate package of programs permit them to propagate in the detector; each simulation code will be described in detail in this chapter. The codes are written in C++ or Fortran languages. The requirements for a complete detector MC simulations are

- Neutrinos and atmospheric muons must be generated with energies up to about 10^8 GeV.
- It must generate the Cherenkov light produced by the charged secondary particles.
- It must include electromagnetic showers from processes such as bremsstrahlung in the muon energy loss as localized events along the track .
- The effect of sea water on light propagation must be correctly modelled. This is important for a good timing resolution of up-

[1]Laboratori Nazionali del Sud-INFN, Catania(Italy) `www.lns.infn.it`

ward going muon tracks and also for the background downward going muons. The effect of the decay of ^{40}K is taken into account.

- For neutrinos that interact inside the can, the light produced by hadronic shower at the vertex must be included.
- The response of PMTs as function of wavelength and incident angle must be included.

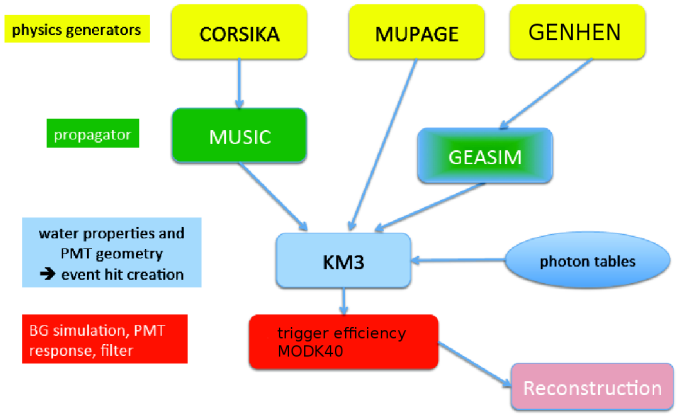

Figure 4.1: Scheme of the codes used to simulate the events in ANTARES and KM3NeT.

In the following the single steps and requirements for a complete MC simulation will be described.

4.1 The detector geometry

The code `GENDET` [78], that is the first step of the simulation, generates an ASCII file with a complete information of the detector geometry. User can specify the kind of footprint of the detector (square, hexagonal or custom defined), its geographic coordinates, the spatial coordinates of PMTs and the list of all constitutive components (buoy, tubes, OM, etc) with their main characteristics. An example of the footprint of the detector in sea-bed is shown in figure 4.2.

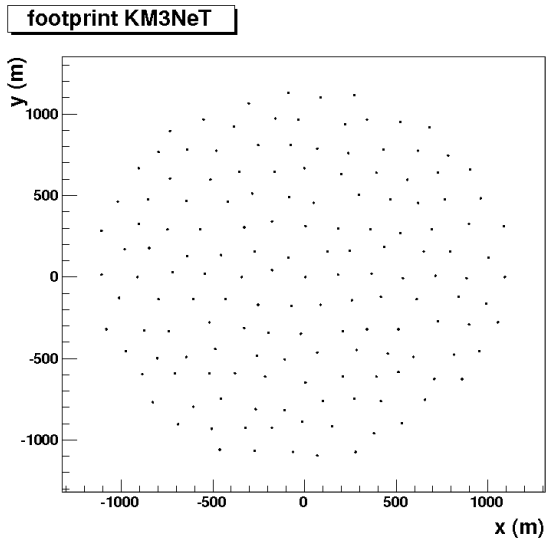

Figure 4.2: Footprint of the detector geometry with 154 detection units (see the detailed geometry characteristics in section 3.1).

4.2 Generation of neutrino events

The generator programs are the yellow ones glancing at the scheme in figure 4.1.
The atmospheric muons can be generated by two codes, `CORSIKA` [79] (and its propagator `MUSIC`) and `MUPAGE` [80] (see section 4.3). The code that generates neutrino events is `GENHEN` [81].
The `GENHEN` program generates distributions of neutrino particles both within and on the surface of the "can" corresponding to interacting neutrinos with a user input spectrum; it can simulate the three neutrino flavours $(\nu_e, \nu_\mu, \nu_\tau)$. In the code the can is defined as a cylinder that include the detector instrumented volume and in which there Cherenkov photons are simulated as illustrated in figure 4.3. It is defined as a volume around the detector at a user specified distance that is typically two or three times the absorption length λ_{abs}.
The total generation volume is defined as a large cylindrical volume. Vertically downwards and horizontally, its extent is determined by the maximum muon range $R_{max}(E_\nu^{max})$ for the largest simulated neutrino energy in the appropriate medium. Upwards its extend is the smaller value between $R_{max}(E_\nu^{max})$ in water and the sea surface in `GENHEN` code.
Neutrino interactions (described in sections 2.2.1 and 2.2.2) are simu-

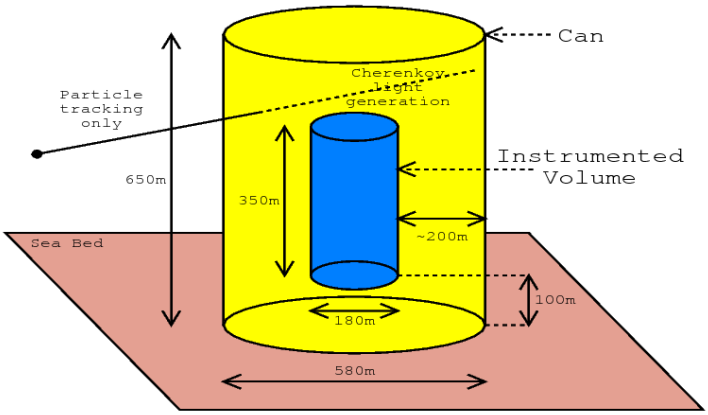

Figure 4.3: Overview of the simulation scheme: neutrino interactions are generated in a large volume (tens of kilometres). The resulting muons are propagated to the can (yellow); only inside it the Cherenkov light and the detector response are simulated.

lated with LEPTO [82] for the deep-inelastic scattering (DIS) channel and RSQ [84] for resonant and quasi-elastic (QE) events. The simulation then proceeds as follows:

- The total interacting neutrino spectrum is divided between E_{min} and E_{max} into equal bins in $\log_{10}(E_\nu)$ and the number of events, N, to generate in each bin is calculated.
- For each energy bin, a maximum range in rock and water using the maximum energy in that bin is calculated.
- A cylindrical volume around the instrumented volume of the detector is defined with a radius $R_{max}(E_\nu^{max})$.
- For each energy bin the numerical integration of the cross-section in LEPTO is performed and the generation for just this energy range is initialised.
- Looping over the number of events to generate in this scaled volume, N^i_{scaled}. At this point the energy of the interacting neutrino is sampled from the $E^{-\gamma}$ spectrum within the energy range of this bin and its position is chosen within the scaled volume. If its vertex is outside the can, the shortest distance from the neutrino vertex position to the can is calculated. If this distance is greater

than the maximum muon range at that neutrino energy, no muon produced by this neutrino will ever reach the can and the event is rejected with no further processing. The neutrino direction is sampled from an isotropic distribution. For events outside the can, it is calculated whether the distance of closest approach of the neutrino direction to the can is greater than some user specified distance. For events inside the can, all these particles are recorded (position, direction, energy, etc) for further processing; while for these outside the can, only the muons are kept. If an event is kept, the "event weights" is calculated and all the event informations written on disk.

- On completion of all the stages above, we get a record of every one of the $\sim 5 \cdot 10^8$ neutrino interactions which produced at least one particle at or inside the can.

4.2.1 Neutrino fluxes and event weights

The procedure described can generate events starting from a specific energy spectrum $E^{-\gamma}$. Anyway is possible to reweight the flux with another spectrum. To calculate the event weight, we need to define the following parameters:

- V_{gen} $[m^3]$: is the total generation volume.
- $I_\theta[sr]$ the angular phase space factor $2\pi \cdot [\cos(\theta_{max}) - \cos(\theta_{min})]$ where θ_{max} and θ_{min} are the maximum and minimum angles of generation.
- I_E the energy space factor, equal to $(E_{max}^{1-\gamma} - E_{min}^{1-\gamma})/(1-\gamma)$ (where E_{max} and E_{min} are the maximum and minimum energies of generation) and to $\ln(E_{max}/E_{min})$ for $\gamma = 1$.
- $\sigma(E)$ $[m^2]$ the total neutrino cross-section for energy E.
- $\rho \cdot N_A$[2] the number of target nucleon per m^3. The code works in unity "water equivalent" , fixing to one the density of all material and dividing the physical distances for the effective density.

[2]The Avogadro's constant is $N_A = 6.022 \times 10^{23} mol^{-1}$

- P_{Earth} is the probability for the neutrino to penetrate the Earth and vary from 0 to 1.
- t_{gen} is the generation time (arbitrary).
- N_{tot} is the total number of generated events.

Now, the generated events correspond to a rate, Φ_ν , of interacting neutrinos has the following distribution:

$$\frac{d\Phi_\nu}{dE_\nu dV dt d\Omega} = \frac{E^{-\gamma}}{I_E}\frac{1}{I_\theta}\frac{N_{total}}{V_{gen}}\frac{1}{t_{gen}} \tag{4.1}$$

Integrating this over the range of angles, energy, time and volume simulated correctly gives the total number of generated events. The rate of interacting neutrinos depends on the incoming neutrino flux (per unit area dS), the target density and the neutrino cross-section. Hence the flux of neutrinos arriving at the detector is given by the rate equation 4.1 divided by the target nucleon density and neutrino interaction cross-section:

$$\frac{d\phi_\nu}{dE_\nu dS dt d\Omega} = \frac{d\Phi_\nu}{dE_\nu dV dt d\Omega}\frac{1}{\sigma(E_\nu)\rho N_A} = \frac{E^{-\gamma}}{I_E}\frac{1}{I_\theta}\frac{N_{total}}{V_{gen}}\frac{1}{t_{gen}}\frac{1}{\sigma(E_\nu)\rho \cdot N_A} \tag{4.2}$$

While the flux of neutrinos arriving at the Earth is:

$$\frac{d\phi_\nu}{dE_\nu dS dt d\Omega} = \frac{N_{total}}{V_{gen}\cdot I_\theta \cdot I_E E^\gamma \sigma(E_\nu)\rho \cdot N_A t_{gen} P_{Earth}(E,\theta)} \tag{4.3}$$

For a flux corresponding to a particular model, the equation 4.3 corresponds to $\phi^{model}(E_\nu, \theta_\nu)$. To re-weight the events it's necessary multiply each interval $dE_\nu d\theta_\nu$ by the ratio of the two fluxes at that point. This then gives the weight, W_{event} , with a flux independent part, $W_{generation}$, associated with each individual event for a particular model:

$$W_{generation} = \frac{V_{gen}\cdot I_\theta I_E \cdot E^\gamma \sigma(E_\nu)\rho \cdot N_A t_{gen} P_{Earth}(E,\theta)}{N_{total}} \tag{4.4}$$

$$W_{event} = W_{generation} \cdot \phi^{model}(E_\nu, \theta_\nu) \tag{4.5}$$

To obtain distributions or event rates corresponding to a particular model ϕ^{model} we then just multiply each event by W_{event} when filling histograms. In figure 4.4 we have weighted with two different energy spectra the reconstructed tracks.

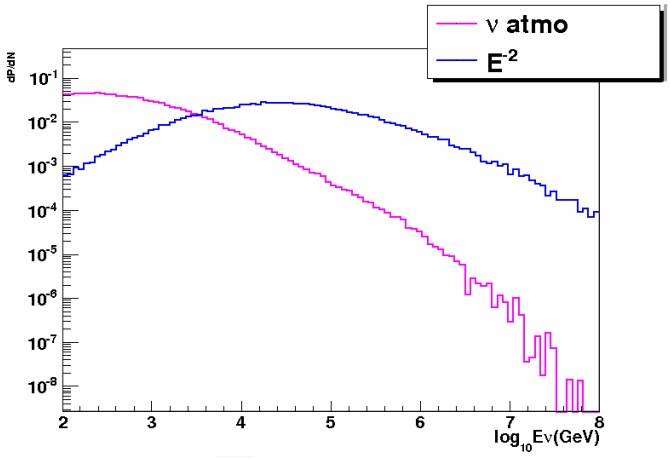

Figure 4.4: Example of reconstructed tracks weighted in different manner: with a Bartol flux (pink) and with a spectrum $\sim E^{-2}$ (blue). Both histograms are normalized to one.

The probability of neutrino absorption in the Earth

The Earth is opaque to very high energy neutrinos. The column density seen by neutrinos with $\theta > 145°$ is enhanced due to the increased density of the Earth core. The probability that the neutrino survives its journey through the Earth is given by:

$$P_{Earth}(E_\nu, \theta_\nu) = e^{-N_A \sigma(E_\nu) \rho_\theta} \tag{4.6}$$

in which ρ_θ is the amount of matter that the neutrino encounters. For vertically tracks, absorption in the Earth starts to be significant for neutrino energies above 10 TeV while for energies above 1 PeV, only neutrinos close to the horizontal remain unattenuated. The probability as function of energy and direction of neutrinos is shown in figure 4.5.

Atmospheric neutrino flux

The events in the code are all generated with a "default" weight that simulates the flux of atmospheric neutrinos. There are several calculations of the atmospheric neutrino flux depending on measurements of the primary cosmic ray flux and different interaction models in the atmosphere; two of the main models of interest are Honda (HKKM) [89] and Bartol [88] and, in this thesis, the last one was chosen. The close agreement evidenced in figure 4.6 between the HKKM and Bartol calculations is a result of a cancellation between the differences in the

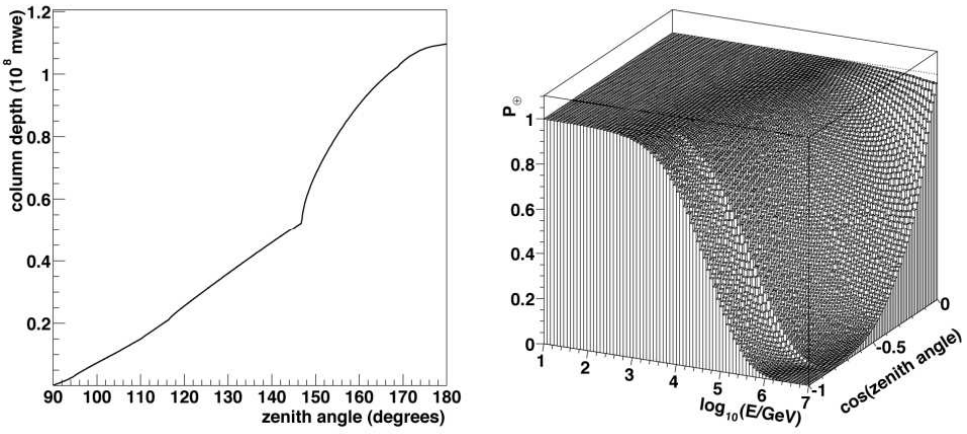

Figure 4.5: Left: The density of the Earth, integrated over the path of the neutrino as a function of the direction of the neutrino expressed in meters of water equivalent. The kink in the figure is caused by the density discontinuity associated with the boundary of the Earth's core. Right: The probability of a neutrino to traverse the Earth without undergoing an interaction as a function of its direction (zenith angle) and its energy [87].

primary cosmic ray spectrum used and the hadronic interaction models and that the actual uncertainty is much larger than the difference between these two models suggests.

4.3 Generation of atmospheric muons

As hinted, there are two generators of atmospheric muons that can be used: MUPAGE [80] and CORSIKA [79]. CORSIKA is a program for detailed simulation of extensive air showers initiated by high energy cosmic ray particles. Protons, light nuclei up to iron, photons, and many other particles may be treated as primaries. The secondary particles produced in the atmospheric shower are simulated taking in consideration their energy loss, the decay of unstable particles, the electromagnetic and hadronic interactions and the deviation of the trajectory of electrical charged particles in the Earth's magnetic field.
In order to save computing time, a fast MC generator is essential especially when the simulation is for a very large detector. The software used is the MUPAGE package that reduce at minimum the time of calculations. The program was developed from parametric formulas derived in [80], that describe the flux, the angular distribution and the

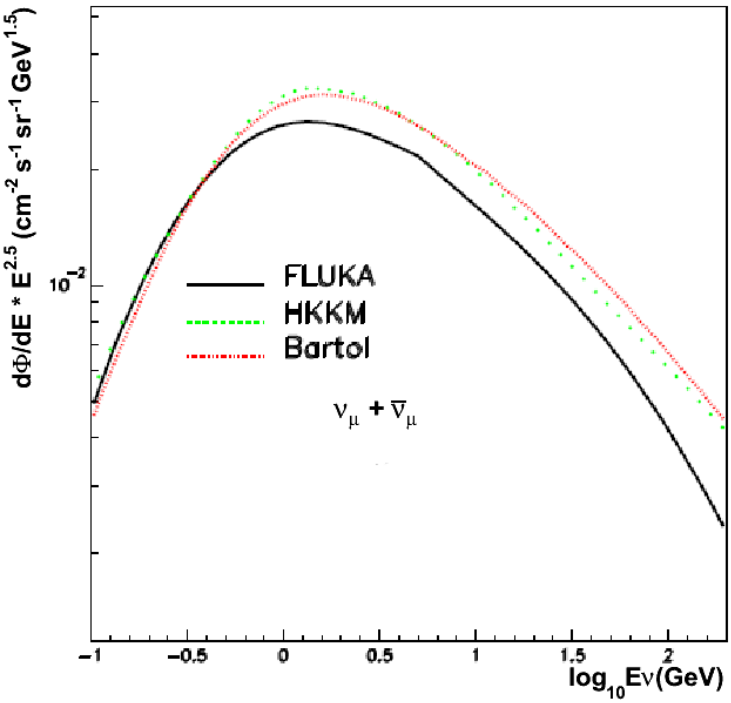

Figure 4.6: Atmospheric neutrino flux for three different models: HKKM [89], FLUKA [90] [91], Bartol [88].

energy spectrum of underwater muon bundles with maximum depth from 1.5 to 5 km w.e. and with zenith angles from 0° to 85°. The parametrization of the interaction of cosmic rays and the propagation in the atmosphere up to the sea leve is based on HEMAS [83] code, while the propagation of muons until 5 km under the level of the sea was performed by MUSIC [94]. MUPAGE generates muons directly on a cylindrical surface with an high, radius and position defined by users (but usually it is used the same surface of the can in GENHEN). It's assumed that all the muon bundles are parallel to the axis of the shower and that they arrive at the same time into a plane perpendicular at the axis. For every N simulated events a "livetime" is estimated. The livetime is the interval of time in which the flux correspondent to N muons is produced in nature.

4.4 Propagation of particles and light production

Once that particles are generated they must be propagated through the volume. In order to take into account the light produced in water, we have three types of particles inside the can:

- Muons that are characterized by long, approximately straight tracks continuously losing energy and emitting Cherenkov photons. They also suffer stochastic losses which produce independent electromagnetic (EM) showers.
- EM showers that are either produced by bremsstrahlung photons from muons or by electrons at the neutrino interaction vertex. All their energy is deposited in a short distance (on the scale of the detector) and can generally be considered point-like . They contain a large number of electrons and hence , statistically, showers of a similar energy all have similar properties.
- Hadrons at the neutrino interaction vertex, that have complex decay chains and the amount of light they produce depends on the primary particle and its particular set of decays. In addition, they may produce muons in the final state which may travel a significant distance. Hence, they are not amenable to parametrization in the same way electrons and muons are.

The codes that propagate and simulate light are :

- `KM3` [85] In which "photon tables" are generated. In these tables the amount and the arrival times of Cherenkov light detect by individual PMTs at different positions and orientations with respect to short muon track segments and EM showers are parametrised. These tables are used to simulate individual muons with bremsstrahlung showers and to include the effect of photon scattering and absorption in the water. KM3 can be used only for the muon neutrinos and not for the other flavour.
- `GEASIM` [86] Performs a full tracking simulation of all particles except Cherenkov photons as they pass through the detector. It

uses an analytical function to calculate the number of photons detected. In principle, this is a full GEANT simulation and can propagate electrons, tau-meson and muons also.

In the order to speed up the simulation and because in this analysis only the ν_μ interaction channel is taken into account; the propagator chosen was KM3 package. More informations about the differences between the two packages are well explained in reference [93]. KM3 package is divided into three subpackages:

1. `GEN`: Generates "photon fields" at various radii from a muon track segment or an electromagnetic shower;
2. `HIT`: Transform the photon fields from GEN into "hit probability distributions" in a photomultiplier tube;
3. `KM3MC`: A detector simulation program which uses the hit probability distributions generated in HIT along with a geometrical description of the detector to simulate events in it.

4.4.1 Photon table generation

GEN simulates the generation of Cherenkov light by a particle in a given medium (in this case water) ,including light from any secondary particles. A complete GEANT [92] simulation is used at this step. GEN tracks the Cherenkov photons through space with wavelength-dependent absorption and scattering taken into account, recording the position, direction and arrival time of photons at spherical shells of various radii centred at the origin. Its output consist of:

- A table containing all the photons recorded in each spherical shell.
- An ASCII file containing the information relevant to the simulation (particle type, energy, number of processed events, track length, medium type, number of events stored in each shell, water model used, etc.)

The original particle can be a GEANT particle. For the muons GEN will stop tracking after 1 metre of length travelled while for electrons the

track length varies with the momentum and the medium density. After this, the particle is propagated through the medium . All the secondary particles produced by the main particle are also processed. The number of Cherenkov photons produced by track segment is computed and for each of them a position , an energy and a direction are given.
Finally each photon is propagated through the volume, recording its parameters at the boundaries region until it is absorbed or leaves the volume (see figure 4.7). Absorption spectra and the scattering length (see section 2.3.4) are read from an external file. For a given water model GEN would propagate particles up to a distance of 200 metres with about 15 shells each containing about 60000 photons.

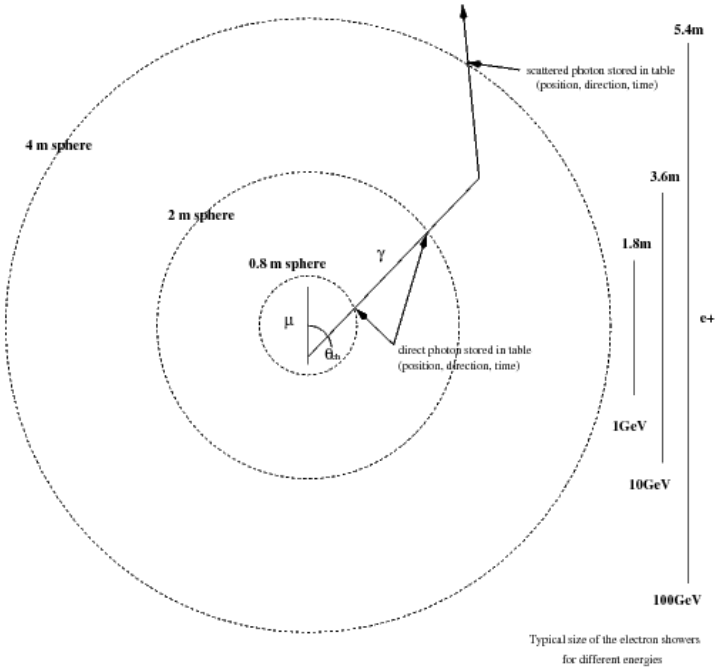

Figure 4.7: GEN program: Muons and electrons are propagated through the medium and Cherenkov photons stored in spheres at different distances.

4.4.2 Optical Module hit distributions

Using the photon fields created by GEN, HIT creates the Optical Module hit distributions for muon track segments and EM showers.
For each case four OM hit distributions are produced: probability of a direct hit (no scattering), inverse cumulative time distribution of direct

hits, probability of scattered hit and inverse cumulative time distribution of scattered hits. Each photon shell is divided into 20 bands, except for direct hits coming form muons in which only one band is considered.
The user inputs which define the scattered and direct bands and the OM orientation bins are read first. The time dimension is divided into 50 bins for both, direct and scattered hits. When processing muons, events with an energy loss greater than a given threshold are removed. The hit position, direction, energy and time are read shell by shell and stored. Then, hits in a given band and shell are processed and converted into arrays of hit probabilities (N_{det}) and time distributions (t_{dist}) both functions of θ_{OM} and ϕ_{OM}. The muon track is oriented along the vertical inside the shells which are segmented in bands. The generic OM si placed on each shell and band. The relationship between the different elements employed by the HIT routines is illustrated in figure 4.8. For each photon hit on the band, the array of OM orientation is found by calling of specified routines.
The weight of each hit for each OM direction is computed by dividing the effective area of the PMT by the geometrical area of the band $A_{geom}(\theta_{OM})$ and normalizing to the total number of hits. The OM effective area is given by:

$$A_{eff}^{OM} = A_{geom}(\theta_{OM}) \times QE(\lambda) \times CE \times P_{trans}^{glass}(\lambda, \theta_{OM}) \times P_{trans}^{gel}(\lambda, \theta_{OM}) \tag{4.7}$$

where λ is the photon wavelength,$QE(\lambda)$ the probability that a photon generates a photoelectron inside the PMT, CE the probability that an electron into the PMT be accelerated until the first photocathod and finally P_{trans}^{glass} and P_{trans}^{gel} are the transmissions probability for the glass and the gel that constitutes the OM. Once the individual weight of each hit and the total weight for each OM orientation are known, the time distributions for each (θ_{OM},ϕ_{OM}) bin is computed.

4.4.3 KM3MC

Finally KM3MC first reads the users inputs and the output of HIT. Muons are than propagated through the can volume with the MUSIC package, generating segment of track (of the same dimension of those used by GEN) until the muon stops or leave the detector. If the energy

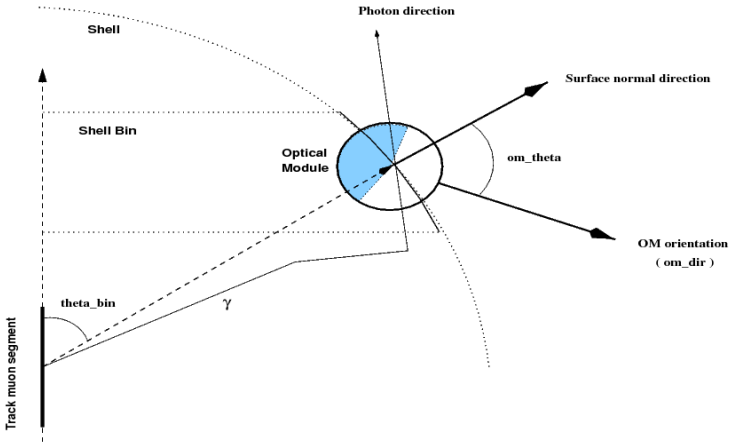

Figure 4.8: View of inter-relationship of elements in the HIT program.

loss is greater than a threshold value, an EM shower is generated in a random position of the segment track.
From tracks parameter and showers (initial and final position, direction, time of occurrence) and from photon tables are obtained the signal "hits". Every hit is characterized by the identification of PMT involved , by the number of deposited photoelectrons (p.e.) and by the photon arrival tim.

4.5 Generation of optical background: MODK40

As explained in section 2.3.3 the ^{40}K is an environmental submarine optical background. MODK40 permits to generate random hit with a frequency defined by users in an interval of time $\Delta t = (t_f - t_l) + 2t_O$, where t_f and t_l are the arrival times of the first and the last hit of the event respectively and t_O the delay to add before and after the simulated event. MODK40 can also simulate the digitalization of the detector. It can transform the light simulated (Cherenkov photons with optical background) into a electronic signal with the appropriate gain factors and electronic noise. A random background rate of 5 kHz is assumed for each PMT, including dark current, ^{40}K decays, and bioluminescence. In addition to random coincidences, an L1 rate of 500 Hz is assumed, due to genuine coincidences from potassium decays. The probabilities for each pair of PMTs inside a multiPMT to produce

such a coincidence is shown in figure 4.9. The level threshold for the ^{40}K is 1 p.e.

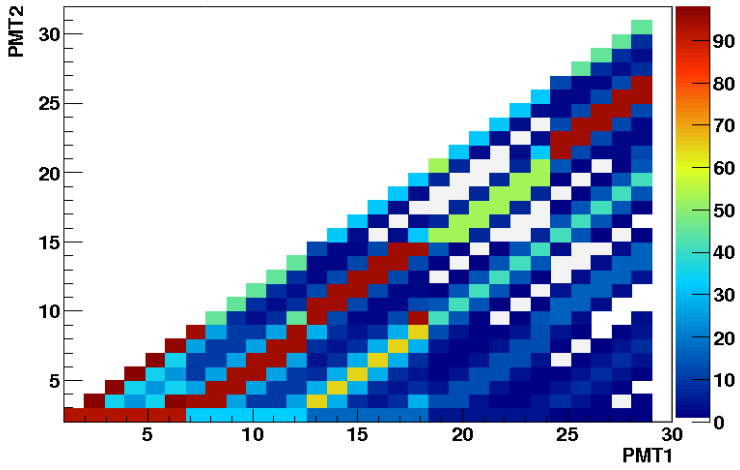

Figure 4.9: Probabilities (unit 10^{-4}) of a genuine coincidences due to potassium decays as a function of the PMT number in a multiPMT optical module.

4.6 Track reconstruction: RECO

The RECO package should estimate direction, position and energy of muon starting from hit amplitudes, photon arrival times and spacial position of PMTs. The reconstruction algorithm, starting from the so-called "Aart strategy" [87], has been modified in order to adapt it for the new features of the KM3NeT detector.
The original strategy consists of four consecutive fitting procedures. The muon trajectory can be characterised by the direction $\vec{d} \equiv (d_x, d_y, d_z)$ and the position $\vec{p} \equiv (p_x, p_y, p_z)$ of the muon at some fixed time t_0. At energies above the detection threshold (about 10 GeV) the muon is relativistic. Hence, the speed of the muon is taken to be equal to the speed of light in vacuum. The direction can be parametrised in terms of the azimuth and zenith angles: $\vec{d} = (sin\theta cos\phi, sin\theta sin\phi, cos\theta)$. There are thus five independent parameters that are estimated by the reconstruction algorithm. For a given track and an OM position $\vec{q}$ (in which $\vec{w}$ is the orientation of field of view) the relevant properties of a Cherenkov photon emitted from the muon are: t^{th} (the expected arrival time), b (the expected path length), a (the expected cosin of angle

of incidence of photon on the OM). From figure 4.10 $\vec{v} = \vec{q} - \vec{p}$ and

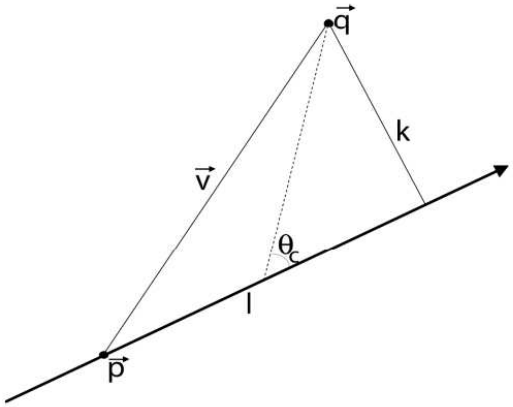

Figure 4.10: Description of the geometry of the detection of the Cherenkov light. The muon goes through point $\vec{p}$ in the direction $\vec{d}$. The Cherenkov light is emitted at an angle θ_C with respect to the muon track and is detected by an OM located in point q. The dashed line indicates the path of the light.

the components of this vector parallel and perpendicular to the muon direction are $l = \vec{v} \cdot \vec{d}$ and $k = \sqrt{\vec{v}^2 - l^2}$. The arrival time is :

$$t^{th} = t_0 + \frac{1}{c}\left(l - \frac{k}{tan\theta_C}\right) + \frac{1}{v_g} \cdot \frac{k}{sin\theta_C} \tag{4.8}$$

The length of photon path is :

$$b = \frac{k}{sin\theta_C} \tag{4.9}$$

and the cosine of incident angle of the photon on OM is:

$$a = \left[\vec{v} - \vec{d}\left(l - \frac{k}{tan\theta_C}\right) \cdot \vec{w}\right] \tag{4.10}$$

4.6.1 Pre-selection of hits

The first step is the selection of the hits.
The hits of background have a low amplitude and they should be reduced; the threshold is setted by user usually at 0.5 p.e. That selection identify the so-called "L1-hits", but an event will be accepted only if there are almost five L1-hits and almost one OM contains three hits in

the same time window of 10 ns. In order to remove the un-correlated hits, due to optical background of ^{40}K, a filtering based on a space-time correlation is applied. In the hit-sample, the hit with the highest amplitude is chosen and a causality filter in comparison of the other hits it's applied. This means that are accepted only the hits that satisfy the following relationship (causality filter):

$$|\Delta t| - \frac{\Delta r}{c/n} < 20\ ns \text{ and } \left|\,|\Delta t| - \frac{\Delta r}{c}\right| < 500\ ns \qquad (4.11)$$

where Δt and Δr are the time and spatial distances of the analysed hit respect to the referred hit and c/n is the group velocity of light in water. The first equation of 4.11 asks that the hit time delay $|\Delta t|$ is compatible (within a time window of 20 ns) with the time that needs the Cherenkov wavefront to cross the distance Δr (see figure 4.11a). From the second

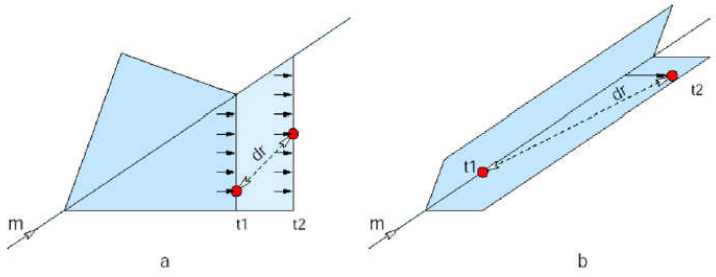

Figure 4.11: Scheme of Cherenkov light propagation to explain reco causality filter. In the case *a*, hits are close and belong to the same wave front. On the contrary, in the case *b*, distant hits can be correlated to the muon track.

equation in 4.11 came that different hits stored at high distances can't be generated from photons of the same wavefront (for a wavelength of 440 nm, λ_{abs} =67.5 m) but can be correlated with the same muon track (see figure 4.11b). In this case, Δt is compared with the time employed by the muon (for hypothesis with velocity *c*) to cross the space Δr. Hits that satisfy the 4.11 are called "selhit" .

4.6.2 Prefit

After the pre-selection a "linear prefit" procedure is applied.
To selected hits a linear fit is applied in order to have a first roughly estimate of the track. This is a geometrical fit through the positions of

the hits with the time as an independent variable. Although not very accurate, it has the advantage that it requires no starting point. It is therefore suited as a first step. In the latest version of the code, the prefit is repeated twice changing the hits used.

- In the first linear fot only L1-hits among the selhit are considered.
- In the second linear prefit all hits with $\cos\theta > -0.5$ are rejected (θ is the angle between the incident photon from the starting track and the axis of PMT).

To obtain a linear relationship between hits positions and track parameters, hits are assumed to be collocated in points that lie on the track itself. This is reasonable if the track length is bigger than the attenuation length and if the distance of hit from the track is very little.

4.6.3 PDF

The next fit procedures are based on the method of "likelihood maximization". Generally if is given a set of n measurement $(x_1, x_2, \ldots, x_n)$ that follow the function f dependent from a parameter a; the likelihood is defined as the probability density function (PDF) that the set would be produced starting from a particular value of a :

$$L(x_1, x_2, \ldots, x_n|a) = \prod_i f(x_i|a) \tag{4.12}$$

From a measurements one can maximize the likelihood respect to a.
In the simulation code the likelihood is the probability that an event will be produced with a set of parameters of track of the muon. So equation 4.12 can be re-written as :

$$P(event|track) \equiv P(hit|\vec{p}, \vec{d}) = \prod_i P(t_i|t_i^{th}, a_i, b_i, A_i) \tag{4.13}$$

where t_i is the time of the i-hit with an amplitude A_i and the other parameters are defined in the first part of this section. This likelihood function remain equal to the original Aart strategy, except for the amplitude dependence which has been neglected. Usually to maximize the likelihood is preferred minimize the value *-log(likelihood)*.

4.6.4 M-estimator

After the linear prefit, a second fit is necessary. It estimates the best track parameters through the minimization of function G depending on them. Hits used in this phase of RECO are called "mest-hit", and are chosen starting on the selhits resulting from the linear prefit. For each selhit it's estimated the time delay respect to t^{th}, estimated from the track parameters in the prefit. It's requested that r lays between -150 ns and 150 ns and that the distance from muon track be less than 100 m. In addition are chosen the hits with amplitudes greater than 2.3 photoelectrons. The function G is given by:

$$G = \sum_i -2\sqrt{1 + r_i^2/2} \tag{4.14}$$

where r_i is the time delay ($r_i = t_i - t_i^{th}$). This quantity is often called "residual"; his shape is shown in figure 4.12. Equation of G in 4.14 differs from the one used in the original Aart Startegy because we don't have considered the dependences on the hit amplitude and on the angular response function of the optical module. The parameters that are obtained from the minimization of function in 4.14 are five : (θ, ϕ, x, y, z) (parameters of *mest-track*).

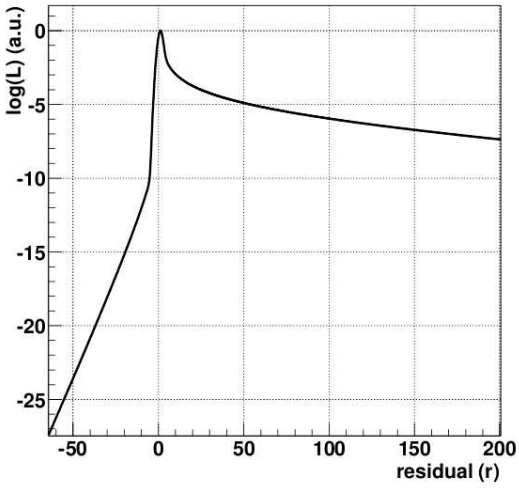

Figure 4.12: PDF used in the M-estimator

4.6.5 Maximum likelihood fit with original PDF

The next step is the maximum likelihood (ML) fit with the original PDF. This fit is performed with hits that are selected based on results of the M-estimator fit. This time, hits are selected with residuals between $-0.5 \times R$ and R, where$R$ is the root mean square of the M-estimator hits residual distribution and if their distance from the M-estimator track is less than 300 m. Hits that are part of a coincidence (5L1 trigger) are also selected and the angular selection is performed.

Repetition of last two RECO-steps with different starting points

It was found that the efficiency of the algorithm is improved by repeating the M-estimator and the PDF fit with a number of starting points that differ from the prefit. The result with the best likelihood per degree of freedom, as obtained in the last step, is kept. The original starting points are obtained by rotating the prefit track until an angle of 30° with rotations by steps of 5°. The origin of the rotation is the point on the track that is closest to the centre of gravity of the hits. In total, the repetition of two procedures is done nine times. Some additional information about the procedure is kept. The number of starting points that result in track estimates which are compatible with the preferred result, will be used in the event selection. This number is called N_{comp} . In case the likelihood of one of the results is very good, the remaining starting points are skipped for execution speed.

4.6.6 Maximum likelihood with improved PDF

Finally, the preferred result obtained in previous step is used as a starting point for the ML fit with the improved PDF. Are calculated the time residual r_i and the distances d_i of the so-called "pdf-hits" respect to the track of the previous fit and are selected those in which $-250ns < r_i < 250ns$ and $d_i < 100m$. Even in this case, the angular selection described in previous steps is applied. Are chosen all the hits with $-T/2 < r_i < T/2$ because the background hits are uniformly distributed in time so to normalize the probability density function $P(r_i|a_i, b_i, A_i)$ the duration of event T needs to be specified. T should contain all the hits of signal so it should be quite big. The PDF is given

by the sum of contributions of signal terms and those of background.

$$P(r_i|a_i, b_i, A_i) = \frac{P^{sig}(r_i|A_i)N^{sig}(a_i, b_i, A_i) + P^{bkg}(r_i|A_i)N^{bkg}(A_i)}{N^T(a_i, b_i, A_i)} \tag{4.15}$$

with $N^T(a_i, b_i, A_i|A_i)$ that is the total number of events expected summing signal and background. Assuming that $P^{bkg}(r_i|A_i) = 1/T$, equation 4.15 can be written as:

$$P(r_i|a_i, b_i, A_i) = \frac{P^{sig}(r_i|A_i)N^{sig}(a_i, b_i, A_i) + N^{bkg}(A_i)}{N^T(a_i, b_i, A_i)} \tag{4.16}$$

Is assuming that for a certain amplitude , the dependence of a and b in the number of hits can be factorized as :

$$N^{sig}(a_i, b_i) = N^{sig}(b_i) \times f(a_i) \tag{4.17}$$

This parametrization of functions in the second member of equation above is obtained by simulations. At level of tracks reconstruction, the

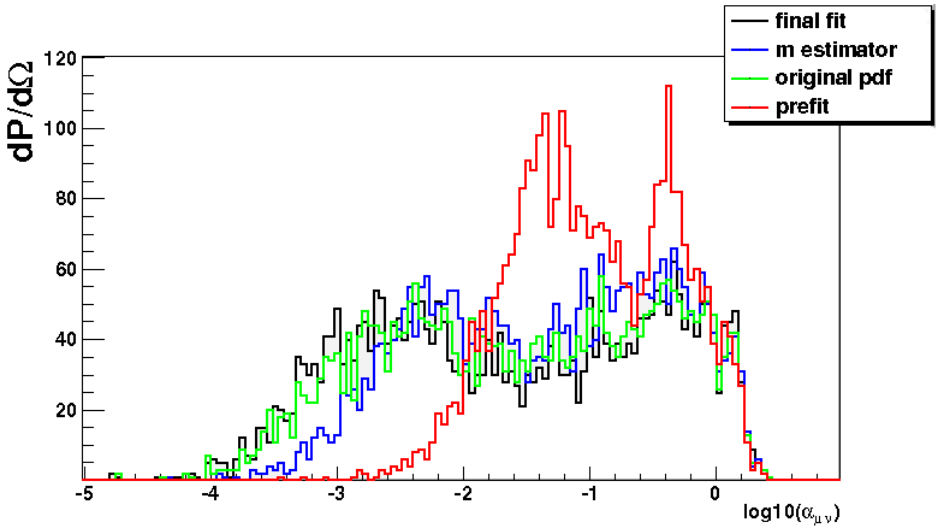

Figure 4.13: Logarithm of the angle, in radiants, between generated and reconstructed muons for the different reconstruction stages described in the text. A full simulation of atmospheric neutrinos has been used. Only tracks reconstructed as up-going are shown.

ratio signal-background is very little also if we want to analyse only the up-going tracks; this is due to the high number of atmospheric muons bad reconstructed. Is necessary to apply cuts on all the reconstructed

events in order to reduce the atmospheric background and extract a better signal-background ratio. For this it's used the parameter of goodness of track reconstruction Λ defined as:

$$\Lambda \equiv -\frac{\log(L)}{N_{DOF}} + 0.1(N_{comp} - 1) \tag{4.18}$$

where $\log(L)/N_{DOF}$ is the reconstruction likelihood logarithm divided by the number of degree of freedom of the fit and N_{comp} is the number of compatible solutions (in 1°) funded in the code of reconstruction [87]. The algorithm's performance is showed in figure 4.13 obtained using a detector configuration described in reference [95].

Chapter 5

Statistical methods in the search of cosmic neutrino sources

In this chapter the two main statistical methods applied to the search of cosmic neutrino sources will be presented. In section 5.1 is introduced the concept of *effective area* for the neutrino. This is a quantity that is proportional the ratio between the reconstructed events and the generated events by the simulation.
In section 5.2 the binned and unbinned methods for the calculation of sensitivity and discovery potential are explained. The unbinned method will be treated in more detail in the last section, the 5.3.

5.1 Effective areas

The neutrino effective area is one of the most relevant quantities for an high energy neutrino telescope. We can list some of the most relevant quantities for the detector performance:

- *Effective Volumes* The volume of a 100% efficient detector for observing neutrinos that interact within that volume which would obtain the same event rate as a detector for a given neutrino interaction rate.

- *Effective Areas for Neutrinos* The area of a 100% efficient surface for detecting throughgoing neutrinos which would observe the same event rate as a detector for a given neutrino flux.

- *Effective Areas for Muons* The area of a 100% efficient flat surface for detecting muons which would observe the same event rate as the detector for a given muon flux (through a flat surface at the centre of the detector).

The relative number of events which arrive as muons on the surface of the detector depends on both the neutrino spectrum and the observed muon energy. The mean number of signal events $\langle N_{sig} \rangle$ into a time window is related to the hypothetical neutrino flux form the source $\Phi_0 E^{-\gamma}$ by the following relation:

$$\langle N_{sig} \rangle = \Phi_0 \int\int A^{\gamma}_{eff}(E, \theta_0(t, \alpha_{RA}, \delta), \phi_0(t, \alpha_{RA}, \delta)) E^{-\gamma} dE dt \qquad (5.1)$$

where (α_{RA}, δ) is the position of the source.

5.1.1 Effective volumes

Before the direct calculation of the effective area, we have to introduce the effective volume.
This quantity includes the efficiency of the reconstruction algorithm described in section 4.6. The aim is to calculate a quantity which, when multiplied by a neutrino interaction rate per unit volume, gives an event rate. The generation of events (described in section 4.2) is done with a power law index, -X, therefore the number of generated events in simulation, $N_{generated}$, in the energy bin E_1 to E_2 and angular bin $\cos\theta_1$ to $\cos\theta_2$ (angle and energy bins are chosen by the user) is :

$$N_{generated}(E_1 < E_\nu < E_2, \cos\theta_1 < \cos\theta_\nu < \cos\theta_2) = \frac{\cos\theta_2 - \cos\theta_1}{\cos\theta_{max} - \cos\theta_{min}} \times \frac{\int_{E_1}^{E_2} E^{-X} dE}{\int_{E_{min}}^{E_{max}} E^{-X} dE} \times N_{total} \qquad (5.2)$$

with E_{min} and E_{max} the minimum and maximum neutrino energies in the event generation, $\cos\theta_{min}$ and $\cos\theta_{max}$ are the smallest and largest values of $\cos\theta_\nu$ in the event generation and N_{total} is the number of simulated neutrino interaction. These quantities are all setted by user as input of the generation program `GENHEN` (see section 4.2).
The generation volume, $V_{generated}$, is identical for all neutrino energies and zenith angles and is calculated as part of event generation in water

equivalent units. The generated number of neutrinos interactions per unit volume is $N_{generation}$ divided by $V_{generation}$; so the effective volume is the ratio between the number of selected events (in the same energy and angular bins) and this density:

$$V_{eff}(E_\nu, \theta_\nu) = \frac{N_{selected}(E_\nu, \theta_\nu)}{N_{generated}(E_\nu, \theta_\nu)} \times V_{generation} \tag{5.3}$$

As in the calculation of the number of generated events above, E_ν refers to neutrino energies in the range $E_1 < E_\nu < E_2$ and in the range in $\theta_1 < \theta_\nu < \theta_2$.

5.1.2 Neutrino effective areas

Is possible to combine the effective volume with the target nucleon density and the energy dependent cross section to produce a quantity which , when multiplied by a differential neutrino flux and integrated gives a rate of observed event. This quantity is an effective area corresponding to neutrino fluxes detectable by the telescope:

$$A_{eff}^{\nu(detector)} = V_{eff} \times (\rho N_A) \times \sigma(E_\nu) \tag{5.4}$$

Multiplying the above effective area by $P_{Earth}(E_\nu, \theta_\nu)$, the absorption of neutrinos in the Earth as described in section 4.2.1, an effective area for neutrinos arriving at the opposite surface of the Earth it's obtained:

$$A_{eff}^{\nu}(E_\nu, \theta_\nu) = V_{eff}(E_\nu, \theta_\nu) \times (\rho N_A) \times \sigma(E_\nu) \times P_{Earth}(E_\nu, \theta_\nu) \tag{5.5}$$

In figure 5.1 it's shown the effective area for upward-going neutrino fluxes arriving at the surface of the Earth for an isotropic flux at the reconstruction level without any quality cuts for different neutrino direction.

5.1.3 Muon effective areas

The muon effective area is defined in the same way as the neutrino effective area, considering now the muon flux that crosses a flat, totally efficient ideal surface. The muon effective area is given by

$$A_{eff}^{\mu}(E_\nu, \theta_\nu, \phi_{nu}) = \frac{N_{selected}(E_\nu, \theta_\nu, \phi_{nu})}{N_{generated}(E_\nu, \theta_\nu, \phi_{nu})} \times \frac{V_{generation}}{\left\langle R_\mu^{eff}(E_\nu) \right\rangle} \tag{5.6}$$

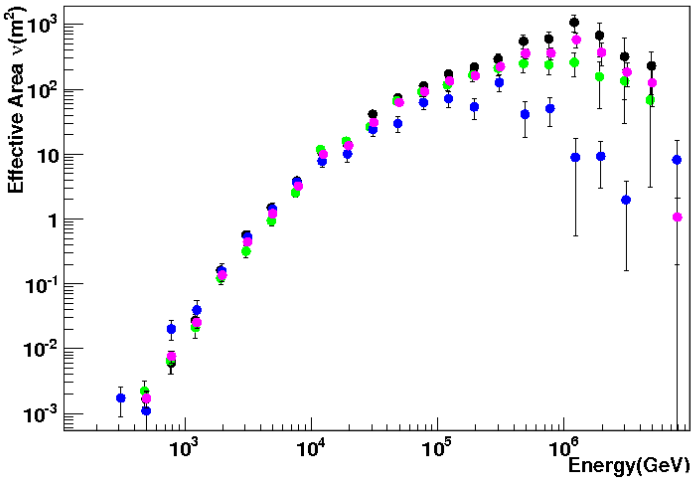

Figure 5.1: Neutrino effective area as a function of the neutrino energy. Different nadir angles have been selected which evidences the Earth opacity at high energies: pink $0° < \theta < 90°$, black $0° < \theta < 30°$, green $30° < \theta < 60°$, blue $60° < \theta < 90°$.

where $\left\langle R_\mu^{eff}(E_\nu)\right\rangle$ is the average muon range defined as

$$\left\langle R_\mu^{eff}(E_\nu)\right\rangle = \int \frac{dP_\mu}{dE_\mu} R_{eff}(E_\mu) dE_\mu \tag{5.7}$$

being dP_μ/dE_μ the probability of a neutrino to produce a muon in the interval dE_μ, and $R_{eff}(E_\mu)$ is the effective range, that is, the average distance travelled by muons with a given starting energy up to the point where their energy goes below a given threshold. Although it is a muon effective area, it is commonly expressed as a function of the neutrino energy, being the muon energy not a suitable magnitude due to the continuous energy loss during the muon flight.

5.2 Sensitivity studies

The principal scientific objective of the KM3NeT neutrino telescope is neutrino astronomy, discovering neutrino sources that, as discussed in chapter 1, are hidden in space but we can argue their position by HE-gamma rays emission.
In the order to obtain the detector sensitivity to a such sources MC simulations, as described in chapter 4, have been used. In particular in

this chapter the main statistical methods used for the search of neutrino from known source among the background events are described. In the following paragraphs the two main statistical methods are explained.

5.2.1 Binned Methods

The data in high energy astronomy consist of a set of events distributed throughout a region of the sky, and can be modelled by two hypothesis: either the data consist solely of background events, i.e. the null hypothesis, or the data additionally contains a signal from an astrophysical source.
The signal and background event distributions are governed by PDFs, describing the event angular distribution, energy spectrum, time distribution, etc. Any difference between the signal and background PDFs provides an opportunity to differentiate events produced by an astrophysical source from the background. Binned and unbinned methods use these PDFs in different ways.
Binned methods are based on the idea to section the sky into a grid with several bins in which search an excess of events on the background. When using binned methods to evaluate whether a source is present at a given location x_{source} in an event sky map, N events can be selected within an angular bin comparable in size to the detector angular resolution and centred on x_{source}, and N is then compared to the expected background using Poisson or binomial statistics. If the probability of obtaining N or more events from background alone is less than a given confidence level threshold, e.g. 5σ ($P = 5.73 \cdot 10^{-7}$), we reject the null hypothesis and decide that a source is present in the data. The mean number of signal events necessary to reject the null hypothesis in a given fraction of trials (e.g. 50%) at the given CL is the discovery potential, a figure of merit for the search.
Binned methods are easy to implement and computationally fast. Criticisms of binned methods and other methods incorporating an event selection are generally the following:

- All of the event information is reduced to a binary classification; either the event passes the selection and is counted, or it does not. A fraction of potential signal events is always lost. Additionally, information contained within the event distribution is lost that

alternatively could indicate the relative agreement of each event with signal or background. For example, events at the edge of a search bin are not as indicative of a point source as events near the center, but are counted the same.

- The selection which optimizes sensitivity [97] (i.e. set the best limits) generally does not maximize discovery potential, and therefore usually one or the other is sacrificed.

5.2.2 Model Rejection Factor (MRF)

The model rejection potential technique [97] (MRP) has seen widespread use in the high-energy neutrino telescope community as a method of unbiased sensitivity (best limit) optimisation of an analysis. For this analysis the approach of Feldman and Cousins [96] is currently used; indeed this method was historically built in order to apply it to analysis of experiments searching for neutrino oscillations.
In contrast with the usual classical construction for upper limits, this construction avoids non-physical confidence intervals as deeply explained in reference [96]. If it's given a model of the signal flux Φ_s which gives a mean number of signal events $\langle n_s \rangle$ and the number of background events is $\langle n_b \rangle$ the sensitivity flux is given by:

$$\Phi_{90} = \Phi_s \times \frac{\bar{\mu}_{90}(\langle n_b \rangle)}{\langle n_s \rangle} \tag{5.8}$$

where $\bar{\mu}_{90}(\langle n_b \rangle)$ is the average maximum limit of background fluctuation at 90% of confidence level observed after hypothetical repetition of an experiment with an expected background and no true signal [96] . $\langle n_s \rangle$ is the number of signal events given by 5.1. The sensitivity flux in equation 5.8 is calculated at 90% of confidence level, is possible to compute it at other level of confidence simply computing the average maximum limits at other level of confidence. As is illustrated in figure 5.2 $\bar{\mu}_{90}$ has a parabolic behaviour with the background. In equation 5.8 the quantity $\bar{\mu}_{90}(\langle n_b \rangle)/\langle n_s \rangle$ is the so-called MRF, the optimal choice of cut would be one that minimises the MRF, however it depends on the experimentally observed number of events n_{obs}.

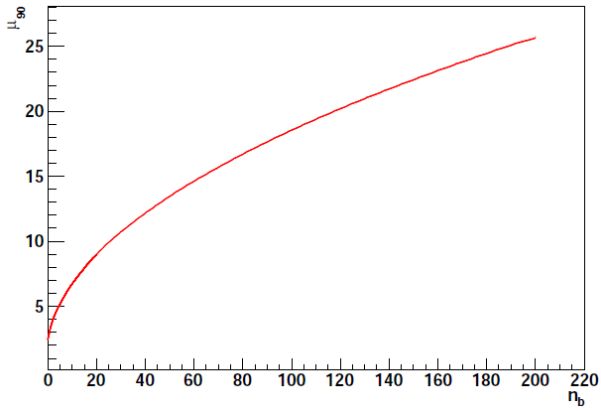

Figure 5.2: $\bar{\mu}_{90}$ (90% of confidence level), as a function of the mean number of background events.

5.2.3 Model Discovery Potential (MDP)

How is a discovery defined? If we are using frequentest statistics, then we usually say we have "discovered" a real effect when the fluctuations on the probability of the observations, are bigger than a certain number of deviations of the only background probability or simply saying that the background only hypothesis is very small[1]. If the background follows a Gaussian distribution a phenomenon is considered "discovered" when an excess of $\alpha = 5\sigma$ over background is found. The numerical value of α (p-value) is given in equation above:

$$\alpha = \int_{x_0=5\sigma}^{+\infty} \frac{1}{\sqrt{2\pi}} e^{-\frac{x^2}{2}} dx = 5.73 \cdot 10^{-7} \tag{5.9}$$

In our counting experiment we calculate the p-value and if it is very small (i.e value in 5.9) we might claim to have seen something of interesting. If $\langle n_b \rangle$ is the average background found, from equation 5.10 we can obtain the critical value of observed events n_{obs} that are

[1]Of course, a small probability of the observation of signal exceeds of a certain under one hypothesis does not imply the truth of some alternative explanation. This commonly used definition of discovery is not consistent with Bayesian decision making and this should be reminded when interpreting results that use frequentest statistic.

necessary to make 5.10 lower than 5 sigmas :

$$\sum_{n_{obs} \equiv n_0}^{\infty} P(n_{obs} | \langle n_b \rangle) \leqslant 2.85 \cdot 10^{-7} \tag{5.10}$$

with $n_0 = \langle n_b \rangle + \langle n_s \rangle$. If a signal source with an average strength $\Phi_{5\sigma}$ is present, the probability that signal and background can produce an observation at a required confidence level (or "statistical power") is given by:

$$P_{5\sigma} = \sum_{n_{obs} \equiv n_0}^{\infty} P(n_{obs} | \langle n_b \rangle + \langle n_s \rangle) \tag{5.11}$$

When the quantity in equation 5.11 reaches the desired confidence level X ($P_{5\sigma} \leqslant X$) we extract the value of events of discovery at that power $n_{5\sigma}^{X\%CL} \equiv \langle n_s \rangle$. Brefly we can say that, given a known mean background $\langle n_b \rangle$ are needed $n_{5\sigma}^{X\%CL}$ events to conclamate the discovery at X CL[2]. Like the average upper limit, also the $n_{x\sigma}^{X\%CL}$ is function of mean background only, as seen in figure 5.3. Now, if we replace

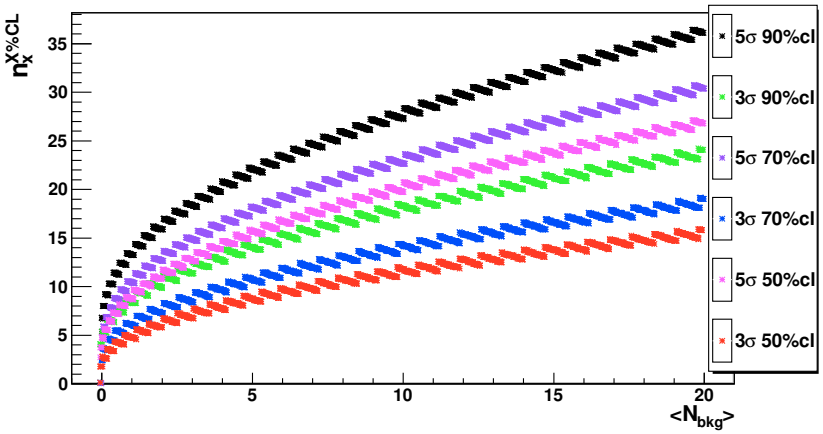

Figure 5.3: The number of events requested for the discovery or the evidence of a signal source are reported as function of the mean of background events at various level of confidence.

the average upper limit in the model rejection factor calculation with

[2]In the same way is possible to calculate the number of events for the "evidence" at $3\sigma = 2.77 \cdot 10^{-3}$ or at other level of goodness 4σ, 2.5σ simply recalculate the value of α in 5.9

the least detectable signal, we can minimize the "model discovery potential" (MDP) of the experiment.

$$\Phi_{x\sigma}^{X\%CL} = \Phi_s \times \frac{n_{x\sigma}^{X\%CL}(\langle n_b \rangle)}{\langle n_s \rangle} \tag{5.12}$$

Multiplying the minimum MDP for the model signal flux, the model discovery potential flux (equation 5.12) required to obtain an observation at significance level x with probability X is obtained. As for the model rejection potential case, the minimised discovery potential flux in 5.12 is independent of any original assumption of the signal scale.

5.2.4 MDP and MRF optimization

In order to reduce the large amount of misreconstructed down-going muons and atmospheric neutrinos and to select the best reconstructed events in our data sample, some quality cuts have to be applied to reconstructed events. In the case of the present analysis, since we have used the"Full Likelihood" algorithm to reconstruct the events, we have optimized the cut in the quality reconstruction parameter Λ, defined in section 4.6.6 and also in the number of hits in the last part of reconstruction, the "final-fit hits" *NHits*. An example of the differences for these reconstruction quantities ,Λ and *NHits*, between atmospheric neutrinos and signal neutrinos is given in figures 5.4 where only the up-going tracks are taken into account without any other cut. The behaviour of Λ for atmospheric muons in figure 5.4a is quite different compared to neutrinos (atmospheric and cosmic). Indeed Λ can discriminate between the goodness of the reconstructed tracks and can be used as a first level of cut for reject the majority of atmospheric muons that still pass the cut on the horizon. From figure 5.4a we can say that good values are those with $\Lambda \gtrsim -6$.
Instead looking at the number of hits in figure 5.4b where only neutrinos are shown, it leaps out that different spectra index have a really different behaviour. Hence the quantity "Nhit" is a good discriminator in energy, so with a reasonable cut like $\mathrm{Nhit} \gtrsim 30$ can be neglected a good portion of neutrino background events. Furthermore looking at figure 5.4 when the up-going reconstructed muons are shown for two variation of the Λ-cut, is clear that if we combine reasonable cuts on

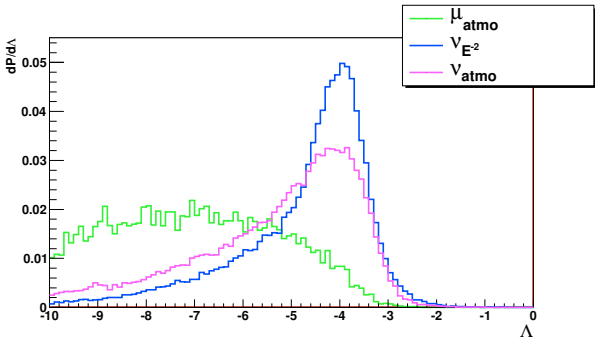

(a) *Lambda*

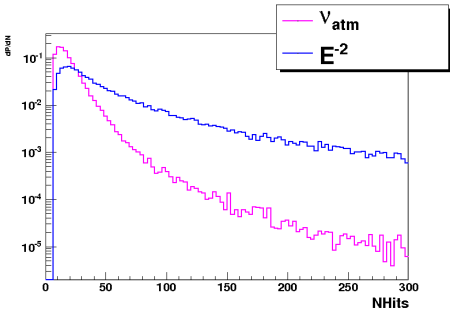

(b) *Number of hits for neutrinos*

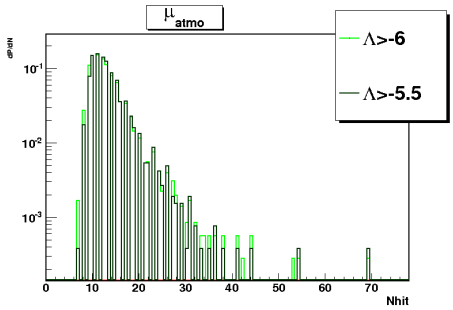

(c) *Number of hits for muons*

Figure 5.4: *a*: Lambda distribution of reconstructed up-going tracks for a signal spectrum E^{-2} ,for the atmospheric neutrinos and for the atmospheric muons. *b*: Distribution of the number of hits of final fit for a signal spectrum E^{-2} and the atmospheric neutrinos of background. *c*: Number of hits for the background of atmospheric muons with cuts on Λ. Histograms are all normalized to one and only a primary cut on the horizon is done.

Λ and the number of hits, we can reject the majority muons (i.e for $Nhith \gtrsim 30$).

The minimization of MRF and MDP for the point-like source is done applying cuts also on these two quantities and varying the opening angle of a cone centred at the declination of the source. The behaviour of MDP with Λ is shown in figure 5.5 where *NHit* is set as a parameter. In this plot the case with no cut on hits have the worst value of MDP. This is a good demonstration of the importance of this quality parameter and justifies the application of it as a secondary cut on the sensitivity studies. Moreover the best value in figure 5.5 is obtained for $Nhit \geqslant 30$ (decrease of atmospheric muons in figure 5.4b) with a minimum value for Λ greater than -5.4 (decrease of bad reconstructed tracks 5.4a).

An example of a 2-dimensional minimization of the MDP analogue

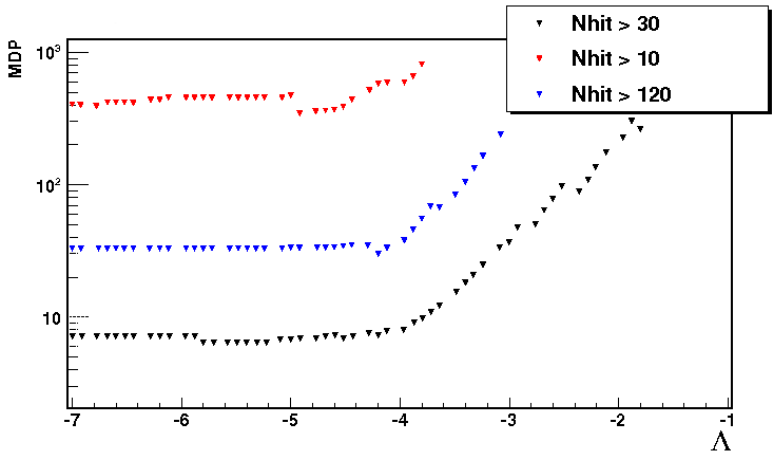

Figure 5.5: MDP minima for a point-source with a detector geometry of reference [95] for one year of data taking and only at the varying of Λ and choosing like a parameter the number of hit. The minimum is for $\mathrm{Nhit} \gtrsim 30$ and $\Lambda \gtrsim -5.5$.

to that of figure 5.5 is shown in figure 5.6.

5.3 Unbinned methods for the discovery of cosmic neutrino sources

The unbinned method models the events as a two component mixture of signal and background and fit them to determine the relative contribution of each component.
With unbinned methods there are mainly two different procedures for the point-like source analysis: the fixed-sky search and the full-sky search.
The main difference between the two methods relies on the fact that in the full sky search the source may lie anywhere in the visible sky and there are no assumption on spectral index while in the fixed-sky search the position and spectral index are known parameters reducing the degrees of freedom of the algorithm. We have investigated only an analysis with fixed-point like source[3].
This method is more sensitive and powerful than the binned approach.

[3]Has been demonstrated that the fixed-point like search is more performant that the full-sky search [**?**].

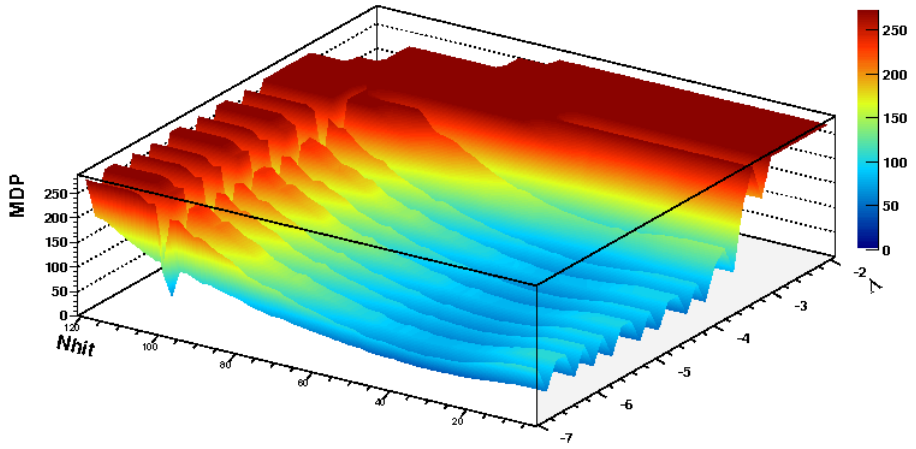

Figure 5.6: MDP minima in 2-dimensions with the detector geometry of reference [95] for one year of data taking in function of Λ an Nhits.

It relies on the maximization of the likelihood derived from a *probability density function* (PDF) assigned to the signal events and background. The signal PDF can be drawn from the point spread function parametrized via Monte Carlo [87] or using a simple Gaussian-shape density [99]. The maximization procedure is also different depending on the algorithm. Contrary to the binned algorithm, now we have an analytical probability distribution associated to our problem. This means that there is no knowledge about the test distribution which is specially important when trying to obtain results at the 5σ confidence level and therefore, the tail behaviour of the likelihood distribution has to be extrapolated in order to overcome this difficulty. Atmospheric muons can be excluded in the Monte Carlo sampling. This is due to the fact that putting constrains on Λ and the number of hits, only few muon background events pass the cuts, as shown in figure 5.4c.
Information on energy, that can be included in the estimate of the test statistic, is now excluded for the analysis.

5.3.1 Monte Carlo samples

The unbinned algorithm method uses a set of reconstructed events as input for the searching process. KM3NeT is currently in the prepara-

tory phase, and therefore, no real data are still available. For that reason, in this work we have built a set of Monte Carlo samples to be used as real data. However, it is important to point out that Monte Carlo samples will be used uniquely as data input and no further information or detector performance will be extracted from the simulation, apart from the signal distribution as it will be explained later.
The track direction is provided by the track reconstruction algorithm in local coordinates. In the samples right ascension and declination (α_{RA},δ) for each event are written. In figure 5.7 an example of background sample corresponding to one year of data-taking in KM3NeT plotted on galactic and equatorial coordinates is shown. The natural

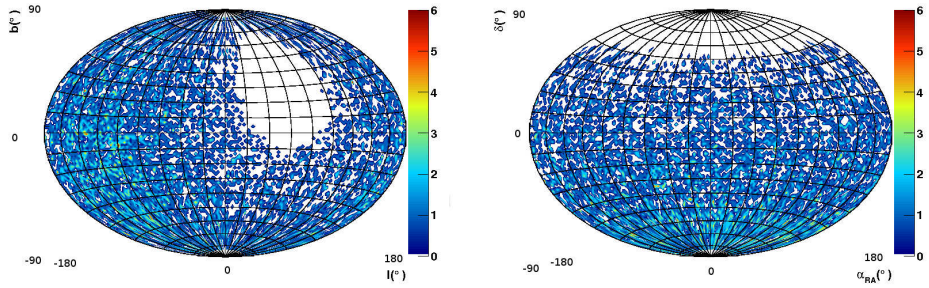

(a) *Galactic coordinates* (b) *Equatorial coordinates*

Figure 5.7: Monte Carlo sample for the background atmospheric neutrinos (in two different coordinates systems) with a geometry of 154 towers for one year of data taking. Only up-going events $\theta_{rec} \leqslant 90°$ are shown.

time scale of cosmic neutrinos expected fluxes is in terms of years; one year data samples are commonly used although more than a year analysis will be also presented. A good estimate of the background is mandatory since most of the events are due to background and only a small fraction of signal events are added to the sample. The main contribution to the background comes from atmospheric neutrinos. As already mentioned, these neutrinos are produced in the upper layers of the Earth's atmosphere in the decays of particles produced by high energy CR interactions and, therefore, these atmospheric neutrinos (and anti-neutrinos) are indistinguishable from cosmic neutrinos (see section 2.3.2).

Background simulation

We need to simulate a considerable number of neutrino and antineutrino events. Using the Monte Carlo production tools described in chapter 4, we produced a total of 100 neutrino files and 100 antineutrino files. Neutrinos and anti-neutrinos were simulated with a 2π isotropic angular distribution and only up-going events were considered. The generation flux follows a power law $E^{-1.4}$ spectrum although a proper weight that takes into account the atmospheric flux is also provided by the generation package.
After the reconstruction of the events a cut is chosen via a binned analysis. Through the minimization of the MDP we can argue the best values for Λ and Nhit. We choose to apply these cuts also to the unbinned method. Usually these cuts have values with ranges of $-6 \lesssim \Lambda \lesssim -4$ and $\mathrm{Nhit} \gtrsim 30$. In order to select the number of background events contributing to the sample, an event rate corresponding to the Bartol model [88] was taken. After selecting the reconstructed track event with direction (θ, ϕ), the arrival time was randomized within a time window of one year and local coordinates were translated by means of the positional astronomy library `slalib` [101], into equatorial coordinates.
The average number of expected events in one year was $\sim 136500\ \nu$ and $\sim 51140\ \bar{\nu}$, which amounts to a total number of about 187640 neutrino events per year. A second contribution to the physical background comes from atmospheric muons (see section 2.3.2) but as previously said, the number of atmospheric muon events (that might be present in the data) sample will be negligible compared to the main background contribution coming from atmospheric neutrinos and therefore they are not included in the sample.

Signal simulation

In an ideal detector, all neutrinos coming from the source will almost point back directly to the source location except for the unavoidable angle between the neutrino track and the muon coming out from the neutrino-nucleon interaction point.
In a real detector, a contribution coming from the angular error due to the track reconstruction process is also present. This angular error

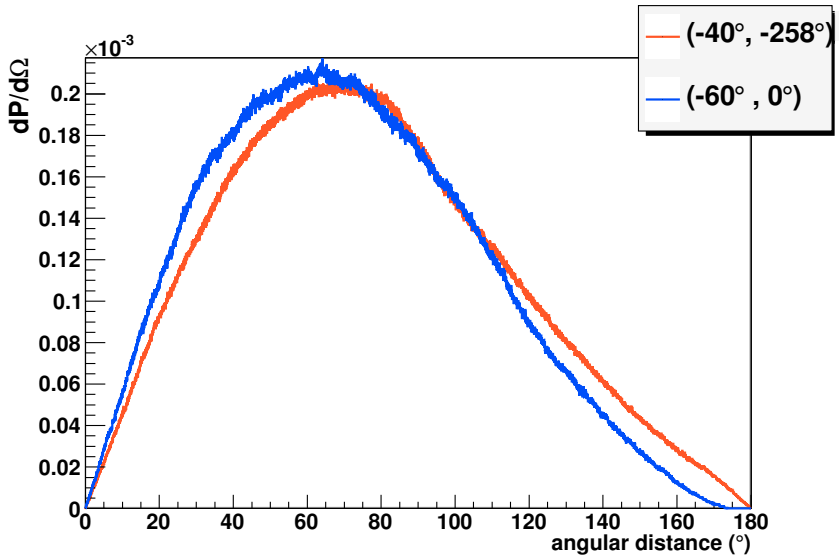

Figure 5.8: Angular distances of background $\nu + \bar{\nu}$ with respect to two different point in the sky: $(\delta, \alpha_{RA}) = (-40°, -258°)$ in orange (coordinates of RXJ1713.3946) and $(\delta, \alpha_{RA}) = (-60°, -0°)$ in blue. Histograms are normalized to one and only the up-going reconstructed tracks are shown.

smears the arrival direction of the neutrinos around the true source location. The angular distribution is known as the Point Spread Function of the telescope and is related to the angular resolution of the detector. Figure 5.9 shows the error distribution of the angle between the true neutrino direction and the reconstructed muon track for each declination band. In order to obtain the angular error distribution as a function of declination, it is necessary to weigh by a given neutrino spectrum.

Signal events are more difficult to simulate since there is no predictive model for point-like sources. However, an educated assumption is to characterize this neutrino flux as a power law of the form $\frac{d\Phi}{dE} \propto E^{-2}$ (see section 1.3). We have simulated also the extended source RXJ1713.3946 that is not properly "point-like" but is simulated into an angular cone of angular width 0.6° for which is estimated a flux of [98]:

$$\Phi(E) = 16.8 \cdot 10^{-15} \left[\frac{E}{TeV}\right]^{-1.72} e^{-\sqrt{\frac{E}{2.1TeV}}} GeV^{-1}s^{-1}cm^{-2} \qquad (5.13)$$

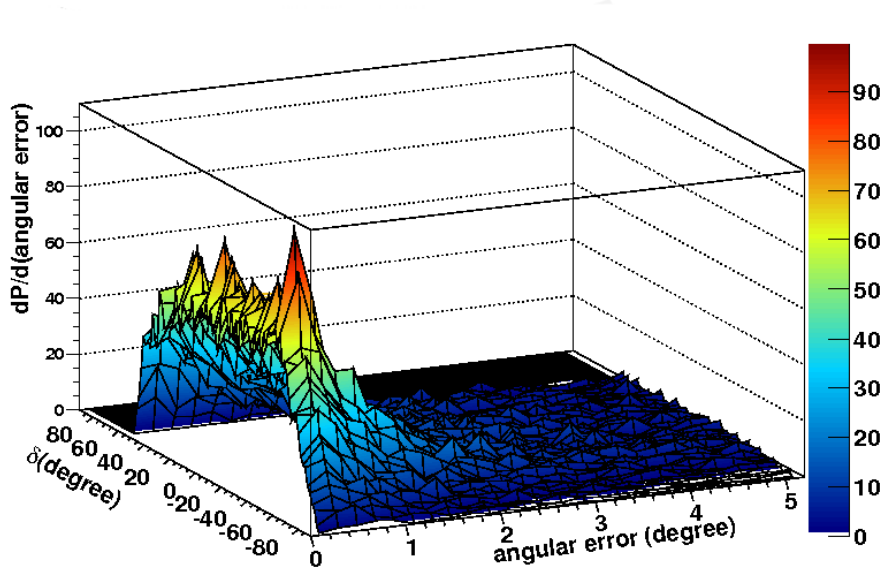

Figure 5.9: Neutrino angular error distribution for different declination bands.

The differences for the two normalized PDFs (point-like with E^{-2} spectrum and extended with a spectrum 5.13) are given in figure 5.10.

5.3.2 The unbinned algorithm

In statistics, a likelihood ratio test is a statistical test used to compare the fit of two models, one of which (the null model) is a special case of the other (the alternative model). The test is based on the likelihood ratio, which expresses how many times more likely the data are under one model than the other. This likelihood ratio, or equivalently its logarithm, can then be used to compute a p-value, or compared to a critical value to decide whether to reject the null model in favour of the alternative model. When the logarithm of the likelihood ratio is used, the statistic is known as a log-likelihood ratio statistic, and the probability distribution of this test statistic, assuming that the null model is true, can be approximated using Wilks' theorem [100]. In the case of distinguishing between two models, each of which has no unknown parameters, use of the likelihood ratio test can be justified by the Neyman-Pearson lemma [102], which demonstrates that such a test has the highest power among all competitors. The goal is to test, at

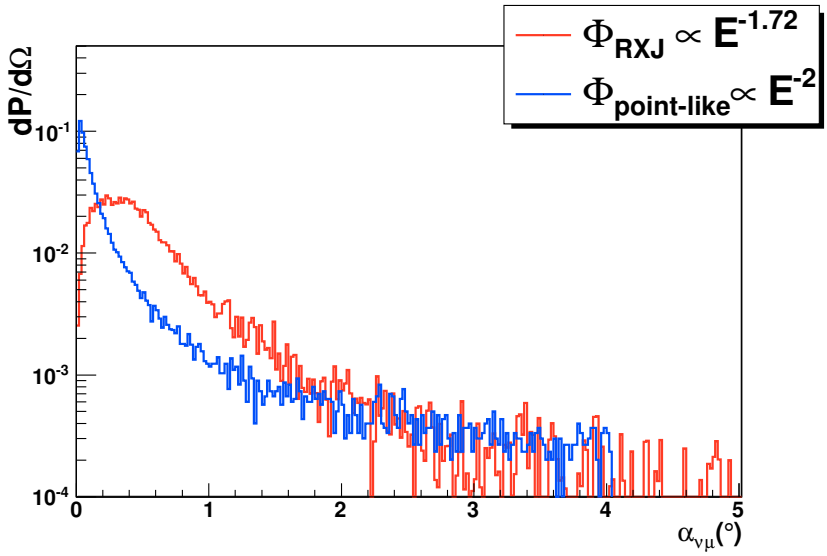

Figure 5.10: Signal PDFs for point-like source (blue) and an extended source (red) weighted with their spectra. Histograms are normalized to one.

a given point (defined as the search point in following), the probability to have a signal for a given background model. The Probability Density Function (PDF) of signal and background are one-dimensional PDFs extracted from the Monte-Carlo simulations. This method is robust, rapid and has a single free parameter. As the calculations are performed in spherical space (equatorial coordinates) there are no singularities. The first step is to calculate the angular distance $\alpha \in [0°, 180°]$ between the search point and the location of all the selected events in the sky. The second step is to fit this distribution with the signal and background PDFs using the likelihood ratio maximization technique (is also possible insert directly the histograms with a properly binning in the algorithm in order to skip this step and make the calculation faster). The likelihood ratio (LR or λ), defined in equation 5.14, is the ratio of probability to have $H_{sig+bkg}$ (the hypothesis of mixed signal and background model) over the H_{bkg} probability (the hypothesis of

only background model)[4].

$$LR = \log \frac{\prod_{i=1}^{n} P(x_i|H_{sig+bkg})}{\prod_{i=1}^{n} P(x_i|H_{sig})} = \sum_{i=1}^{n} \log \frac{P(x_i|H_{sig+bkg})}{P(x_i|H_{sig})} \tag{5.14}$$

where n the total number of events in the sky. $H_{sig+bkg}$ and H_{bkg} are given by:

$$\begin{aligned} H_{sig+bkg} &= \frac{n_{sig}}{n} \times P_{sig}(\alpha_i) + \left(1 - \frac{n_{sig}}{n}\right) \times P_{bkg}(\alpha_i) \\ H_{bkg} &= P_{bkg}(\alpha_i) \end{aligned} \tag{5.15}$$

where:

- n_{sig} is the number of signal events, therefore $\frac{n_{sig}}{n}$ and $1 - \frac{n_{sig}}{n}$ are the fractions of signal and background events respectively.
- $P_{sig}(\alpha_i)$ and $P_{bkg}(\alpha_i)$ are the PDFs of signal and background respectively (see figures 5.10 and 5.8). They are a function of the angular distance α_i of the track and the point-source in the sky.

Replacing expressions 5.15 in equation 5.14 yields:

$$LR = \sum_{i=1}^{n} \log \frac{\frac{n_{sig}}{n} \times P_{sig}(\alpha_i) + \left(1 - \frac{n_{sig}}{n}\right) \times P_{bkg}(\alpha_i)}{P_{bkg}(\alpha_i)} \tag{5.16}$$

The only unknown parameter is n_{sig} which is estimated maximizing LR in 5.16. The output of the algorithm at a given search-point is the maximized LR value and the corresponding fitted n_{sig} value. The likelihood ratio is used in this framework as a discriminator whose sampling distribution can be obtained from Monte Carlo experiments or by data scrambling and tested by the hypothesis testing theory. In our case, the two models to test H_{bkg} and $H_{sig+bkg}$ are the only-background and background plus source model respectively. Once the LR distribution for the only-background case is computed, we can

[4]The unbinned method is in principle applicable also for more than two hypothesis ($g > 2$) with a more complex equation for the statistic test. In this case LR becomes $LR(\Psi) = \prod_{i=1}^{n} \sum_{j=1}^{g} \pi_j p(\mathbf{x_i}, \theta_j)$ where Ψ stands for the set of parameters $\{\pi_1 \cdots \pi_g; \theta_1 \cdots \theta_g\}$ and $\sum_{j=1}^{g} \pi_j = 1$.

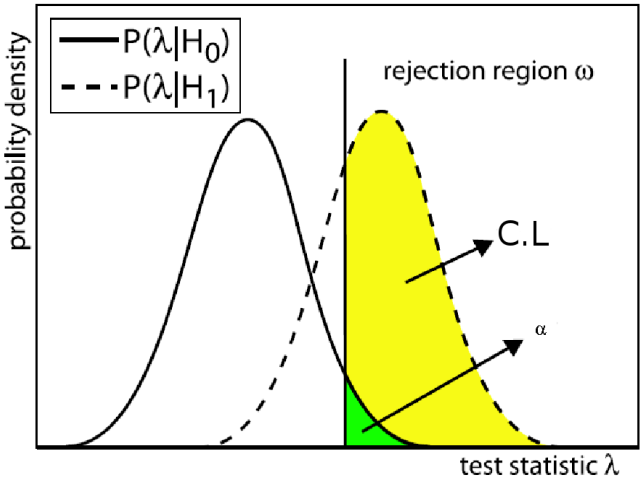

Figure 5.11: With two hypothesis H_0 (only background) and H_1 (background with signal events) the two shapes of likelihood ratio are drawn. Two region are evidenced: the green that represents the level of significance for H_0 and the yellow that represents the "power" region (the confidence level that the hypothesis H_1 is true).

make a decision about the acceptance or rejection of a model over the background hypothesis by the usual way used in model testing theory as illustrated in figure 5.11. The green area is the probability of rejecting H_{bkg} if H_{bkg} is true. It is called the level of significance α and it's value was just computed in equation 5.9. From this region the critical value of LR at the desired α, LR_α, is then extrapolated. The area in yellow represents the power region identified by the critical value of LR for the hypothesis of signal plus background; it is in few words the confidence level. The goal of the algorithm is to find the best estimate of the free parameters in equation 5.16 that maximize the likelihood. In our case, the number of signal events n_{sig} is the only free parameter in fact source position and spectra are fixed. In figure 5.12 there is a schematic explanation of the entire maximization algorithm.

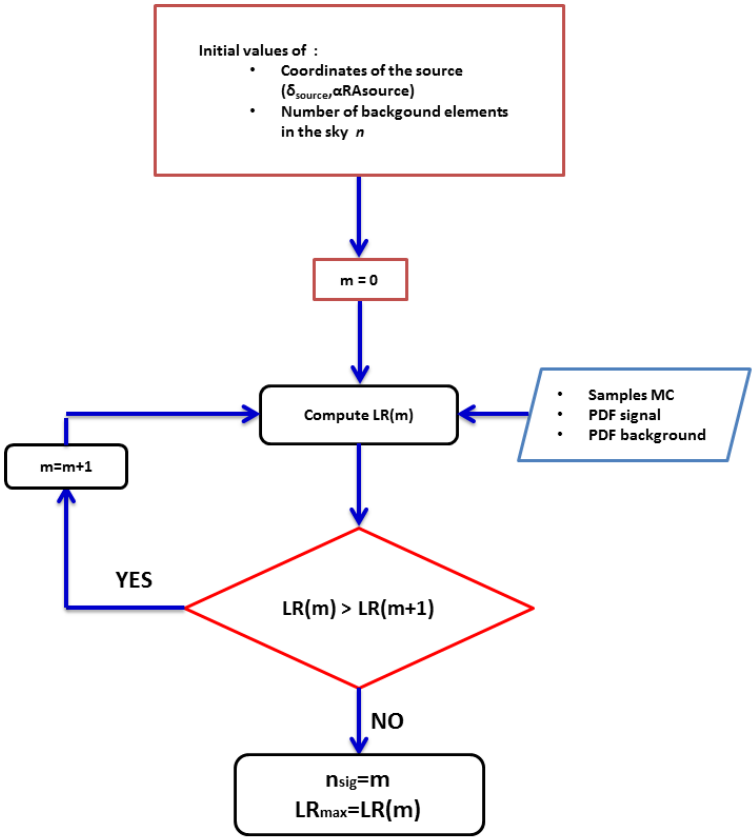

Figure 5.12: Flowchart of the LR maximization algorithm for the fixed-source searching analysis.

Chapter 6

Fixed point-like and extended sources searches

In this chapter the main results on statistical methods (binned and unbinned) described in chapter 5 will be shown .
In section 6.1 are analysed the following sources :

- a generic point-like source at $(\delta, \alpha_{RA}) = (-60°, 0°)$ with energy spectrum E^{-2} that has a full visibility for a detector located in the Mediterranean Sea.
- the RXJ1713.3946 at $(\delta, \alpha_{RA}) = (-40°, -258°)$ with energy spectrum in equation 5.13. This is a SNR with a rather complex morphology in HE gamma emission. For this simulation neutrinos are generated with an uniform distribution into a cone of angular extension of a flat disk with 0.6°.

The fluxes for discovery potential and sensitivity have been evaluated for three different possible KM3NeT detector geometries:

1. 154 detection unit (DU), distance with DU = 180 m , bar length = 6 m
2. 154 detection unit (DU), distance with DU = 130 m , bar length = 6 m

The effective areas for the two geometries at the reconstruction level with a $\theta_{rec} \leqslant 90°$ and a cut on Λ ($\Lambda > -6$) are shown of figure 6.1 while in figure 6.2 are shown the median angles of the distribution of

the angle $\Delta\Omega$ between the neutrino and the reconstructed muon track for the same cuts and geometries of figure 6.1.

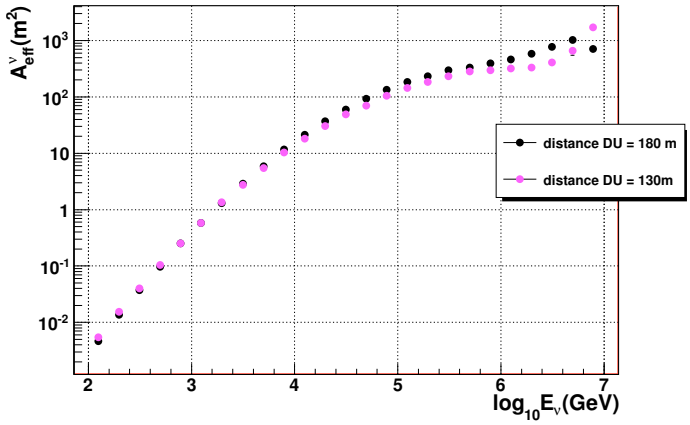

Figure 6.1: Effective neutrino areas for up-going events reconstructed with $\Lambda > -6$ for a geometry with a distance between the detection units of 180m (black) and another with a mean distance between DU of 130 m (pink).

Moreover, an analysis of an extended source, the Fermi Bubbles, has been done in section 6.2 for the ANTARES detector. This analysis has been developed during a period of stage in the ANTARES group at the CPPM[1]. This analysis paves the way to the comparison between data and Monte Carlo simulation.

6.1 Point-like sources analysed with KM3NeT telescope

6.1.1 Likelihood-ratio distributions

For the unbinned analysis of the fixed point-like source search, we have simulated for one year of data taking in KM3NeT, 20000 pseudo-experiments by means of Monte Carlo simulation.
Only one value of likelihood ratio (LR) per sample is produced in the fixed point-like search, contrary to the full-sky search algorithm in

[1]Centre de Physique des Particules de Marseille-CNRS, Marseille (France) `http://marwww.in2p3.fr/`

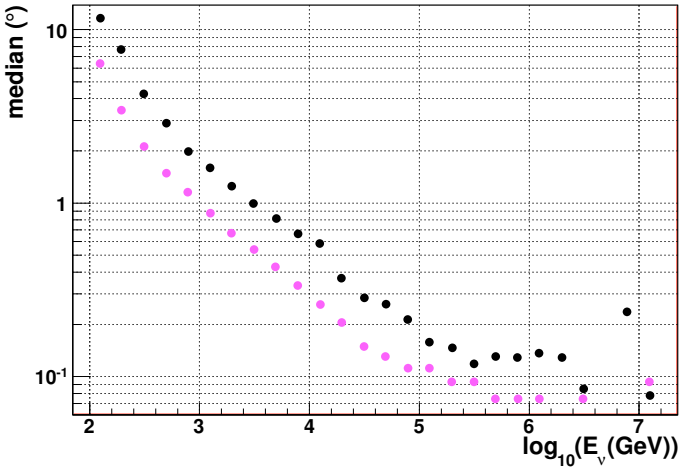

Figure 6.2: Median of the distribution of the angle $\Delta\Omega$ between the neutrino and the reconstructed muon track for up-going events reconstructed with $\Lambda > -6$ for a geometry with a distance between the detection units of 180m (black) and another with a mean distance between DU of 130 m (pink).

which the highest LR value is selected among all the LR values of the candidate clusters [103].

The LR distribution depends on spectral index, declination of the source and years of data taking. Appling the unbinned algorithm described in section 5.3.2, for the only background case we maximize the likelihood ratio LR, in equation 5.16, and we obtain the LR distribution shown in figure 6.3.

The high counts in the first histogram bin of only-background LR in figure 6.3, is due to a mean number of signal events equal to zero as expected with a right maximization algorithm. In fact in equation 5.16 for zero signal events maximized, the relation leads to a maximum LR equal to zero.

The LR distribution computed for an high number of samples can be asymptotically expressed by a $\chi^2_{2n_{dof}}$ distribution with n_{dof} degrees of freedom [100], as shown in figure 6.3 (fit in black line). The integrated probability of $\frac{dP}{dLR}$ is shown in figure 6.4. The tail of distribution is well fitted by $f(x) = e^{(-a\cdot x+b)}$ that is an approximation of the analytical integration of the tail of the $\chi^2_{2n_{dof}}$ distribution.

From the integrated probability the critical values of LR are estimated, those that delimited the region of power and the region of

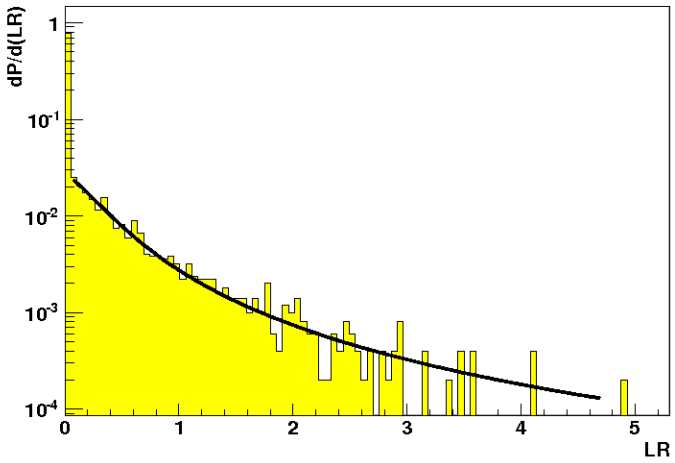

Figure 6.3: $\frac{dP}{dLR}$ probability for the only-background case for 2 years of data taking. The black line is the fit with a $\chi^2_{2n_{dof}}$ distribution. The geometry has a distance between the DU of 180 m.

rejection. The LR critical value at $3\sigma = 2.77 \cdot 10^{-3}$ can be extracted directly from the histogram of figure 6.4 and is 3, while the p-value $\alpha = 5.73 \cdot 10^{-7}$, due to the low statistic, can be extrapolated from the exponential fit and from the fit is ~ 9. Once that the critical values are found we can proceed with the extrapolation of the number of events for the discovery.

6.1.2 Discovery Potential

When a given number of signal events is added to each sample is modified, becoming ever more positive as shown in figure 6.5. Also the distribution of n_{sig} which is the number of signal events can be extracted from the maximization of LR. For example given 4 events of signal per sample the algorithm finds a mean number of 4.1 with a gaussian distribution (see figure 6.7). We use the critical values at 5σ or 3σ obtained in the only background case in order to calculate the probability of discovery in the case of signal n_{sig} plus background. The probability in the case of signal plus background to have a LR larger than $LR_{5\sigma}$ or $LR_{3\sigma}$ is given by:

$$p(LR > LR_{x\sigma}|n_{sig}) = \int_{LR_{x\sigma}}^{+\infty} \frac{dP(LR|n_{sig})}{dLR} dLR \tag{6.1}$$

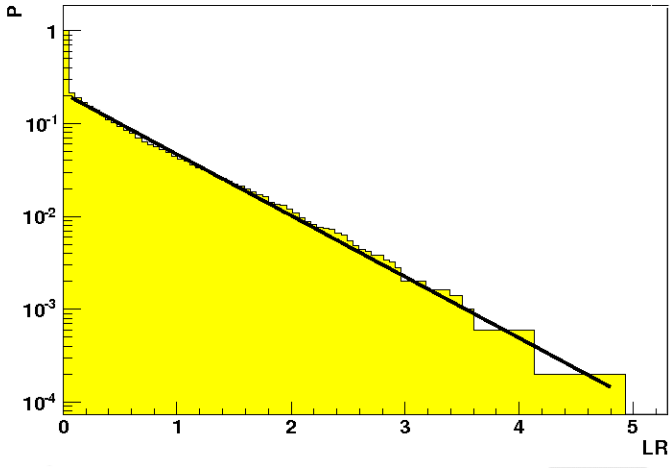

Figure 6.4: Integrated probability for the only-background case for LR distribution on figure 6.5. The black line is the fit with an exponential function.

This is shown in figure 6.6 where the integrated probabilities for the likelihood ratio in the only background (yellow area) and in the background with signal events (coloured lines) are reproduced.
Figure 6.9 shows an example of the probability on the number of signal events fitted from the algorithm. The two plots are deduced for the evidence 3σ (pink) and the discovery 5σ (blue) of the source analysed and the dashed lines are the fitted point with a cumulative gaussian distribution. The discovery potential flux, for a source at declination δ is calculated by:

$$E^2 \frac{d\Phi}{dE} = \frac{\langle N_{sig} \rangle (\delta)}{A_{eff}(\delta) \cdot T \cdot \int_{E_{min}}^{E_{max}} E^{-\gamma} dE} \tag{6.2}$$

where:

- $\langle N_{sig} \rangle$ is the number of expected signal events deduced from the probabilities plot like those on figure 6.9.
- $A_{eff}(\delta)$ is the mean effective neutrino area as a function of the declination of the source.
- T is the time window for the analysis expressed in seconds.
- γ is the spectral index of the source.

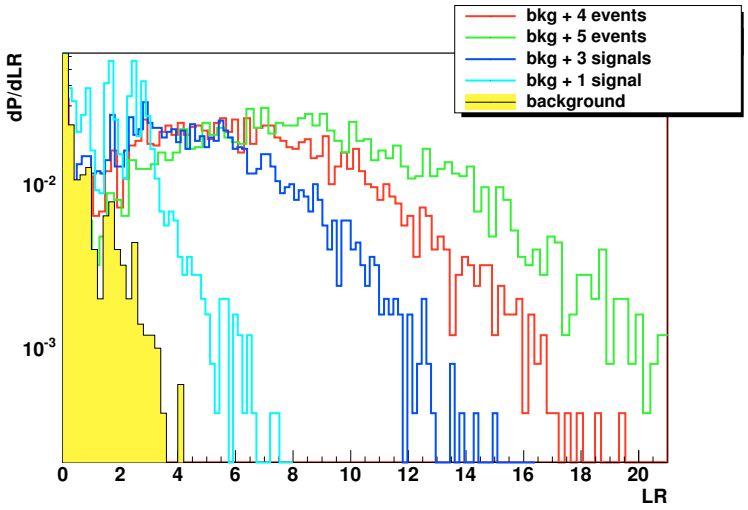

Figure 6.5: LR distributions for the only-background case for a source at declination -60° 2 years of data taking for the only-background (yellow area) and when 1 (light blue), 3 (blue), 4 (red) or 5 (green) events are added to the sample. Geometry 1.

- $[E_{min}, E_{max}]$ is the simulated events energy range that in this analysis is $[10^2 GeV, 10^8 GeV]$.

6.1.3 Analysis for a point-like source at $\delta = -60°$

The unbinned analysis has been applied to a point-like source at a declination $\delta = -60°$ and an energy spectrum E^{-2} for the detector geometry 1. The results are compared with those obtained with the binned method search.

The first cut applied to binned and unbinned analysis is only on reconstructed direction of the tracks, choosing only the up-going reconstructed tracks $\theta_{rec} \geqslant 90°$.

The two probability density function for background and signal are reported in figure 6.8 , where the resolution of the detector is very good as the 50% of events are above 1°. The background has a linear behaviour in the region of angles lower than 5° and decreases at an angular distance of above 60°; this effect is due to the fact that we take into account only up-going tracks and that the sky is finite. In the binned method we minimize, through a cone centred on a source, our MDP (see section 5.2.4). Values for the minimum discovery flux as function

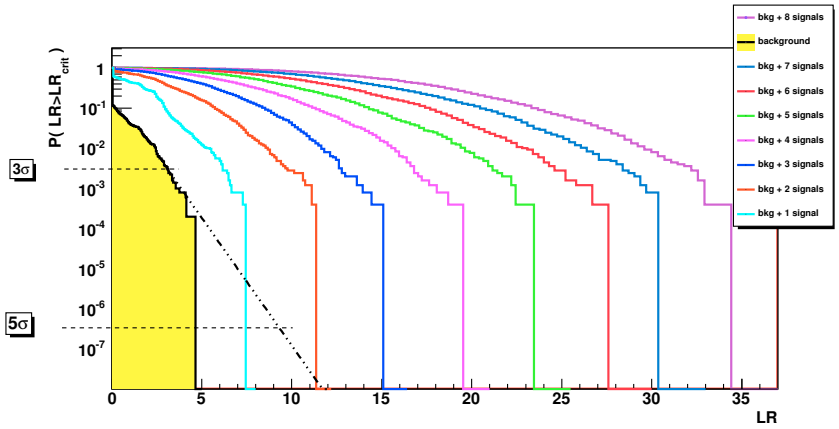

Figure 6.6: Integrated LR for the only-background case (yellow area) and for background + signal events (colored lines). Fitting the yellow histogram can be deduced the critical value at 5σ, $LR_{5\sigma}$, and then the probability value for the case signal+background. Geometry 1.

year	Λ	Nhit	$R_{bin}(^\circ)$	n_{sig}	n_{bkg}	$\Phi[GeVcm^{-2}s^{-1}]$
1	-5.5	47	0.140	81.30	0.015	$3.26 \cdot 10^{-9}$
2	-5.9	55	0.120	142.56	0.015	$1.88 \cdot 10^{-9}$
3	-7.9	56	0.100	195.39	0.015	$1.37 \cdot 10^{-9}$

Table 6.1: Discovery potential minimum flux at 50%CL for a point-like source at $\delta = -60^\circ$ with a model flux $10^{-7}E^{-2}GeVcm^{-2}s^{-1}sr^{-1}$.

of Λ , Nhits and the angle of opening of the cone R_{bin} for the point-like source and several years of data taking are shown in table 6.1 and in figure 6.10. For the unbinned analysis, we first fix the best choice of cuts as that we found from the binned minimization of MDP. The final result of the unbinned method is the mean number of events for the discovery (at 3σ or 5σ) as function of the total probability shown in figure 6.9. The geometry used is that with 180 m of distance between the DU in which the mean effective area for declination $\delta = -60^\circ$ with the appropriate quality cuts, is 0.56 m^2.
The unbinned flux at 50%CL, calculated through the equation 6.2, is reported in table 6.2 and compared with the flux found for binned method. The unbinned method in this case has been more perfomant since for both power, 5σ and 3σ, we have a decreasing on flux for this source of about 17%.

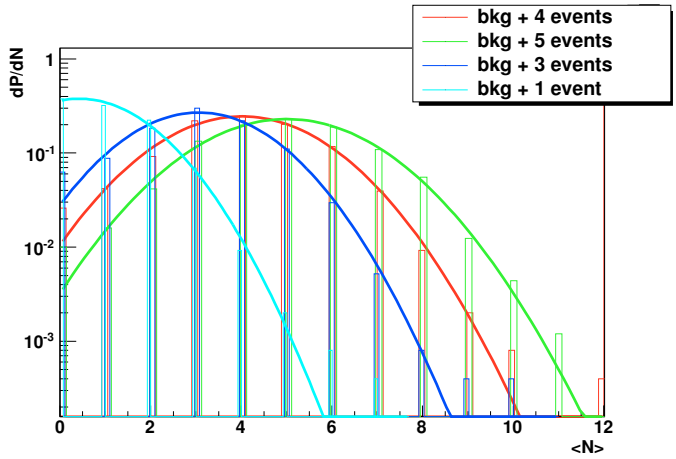

Figure 6.7: Number of signal events found by maximization of LRs of signal+background case in figure 6.5 for a number of 1(light blue), 3(blue), 4(red), 5 (green) signal events added for each sample. Histograms are fitted by gaussian distributions.

$\delta = -60°, \gamma = 2$	Φ_{binned}	Φ_{unbinned}
5σ 50%CL	$1.88 \cdot 10^{-9}$	$1.56 \cdot 10^{-9}$
3σ 50%CL	$9.0 \cdot 10^{-10}$	$7.1 \cdot 10^{-10}$

Table 6.2: Discovery flux for the source with $\delta = -60°$ and spectral index $\gamma = 2$ for 2 years of data taking. Fluxes are in unit of $[GeV\ cm^{-2}s^{-1}]$

6.1.4 Analysis for RXJ1713.3946

The two statistical methods have been applied also in the case of the SNR RXJ1713.3946 source. This source has been described in details in section 1.4.1.
In order to evaluate the discovery flux for this source the following assumptions have been made:

- neutrinos generated with an uniform distribution into a cone of angular extension of 0.6°
- an energy spectra $\propto E^{-1.72} \cdot exp(-\sqrt{E/2.1TeV})$ in equation 5.13. This energy spectra has been obtained from theoretical calculation based on the HESS gamma-rays data (see section 1.4.1).

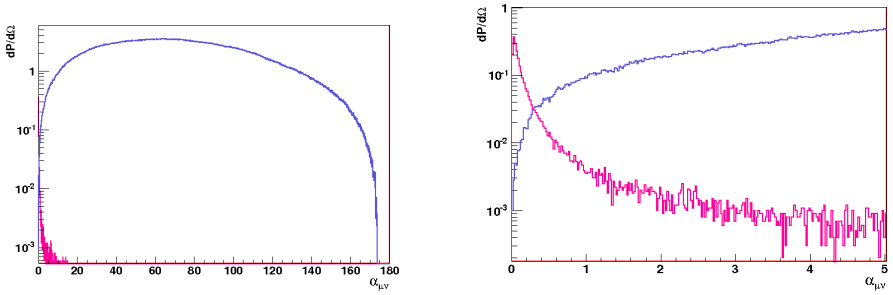

(a) *PFDs for background and signal* (b) *PFDs for background and signal in* 5°

Figure 6.8: PDFs for background (blue) and signal (pink) for $\delta = -60°$ for a geometry with a distance of DU =180m. Histograms are normalized to the number of events attended for 1 year of data taking.

year	Λ	Nhit	$R_{bin}(°)$	n_{sig}	n_{bkg}	$\Phi[GeVcm^{-2}s^{-1}]$
1	-6.1	25	0.760	1.49	2.41	$1.27 \cdot 10^{-13}$
2	-5.3	32	0.740	2.29	2.41	$8.24 \cdot 10^{-13}$
3	-5.3	31	0.700	3.44	3.59	$6.38 \cdot 10^{-13}$

Table 6.3: Discovery potential minimum flux at 5σ and 50%CL for RXJ1713 with a model flux $16.8^{-15}E^{-1.72}\exp(-\sqrt{E/2.1TeV})GeV^{-1}cm^{-2}s^{-1}sr^{-1}$ for a geometry with a distance between towers of 180 m.

The values and the results with the binned values are reported in table 6.3 with the best cut of minimization of the discovery flux. The lower discovery value for one year of data taking is obtained for an angular bin of 0.76° . This cone minimization is bigger than that obtained for the same geometry in table 6.1 for a point-like source of 0.14°. This is due to the difference of the source morphology.
As explained in section 5.3.1 the unbinned analysis needs a cut on Λ and NHit. These values are assumed to be the same of those that minimize the MDP for the binned analysis. The flux values at 1 and 2 years of data taking, for the geometry with a distance between the detection units of 180 m, are reported in table 6.4.
In figure 6.11 the mean number of events for the discovery for one and two years are reported. Unbinned analysis is more performant than the binned analysis for both the two periods of data taking. The gain respect to the binned method is of about 46% for one year and of 40%

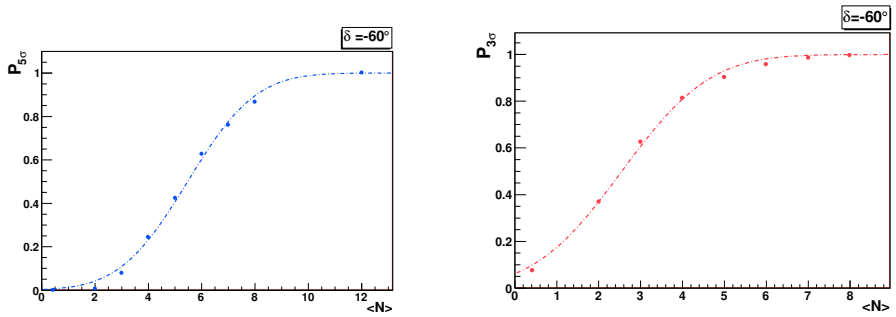

(a) 5σ (b) 3σ

Figure 6.9: Discovery power for two years of data taking for the point-like source located at declination 60° with an energy spectrum $\propto E^{-2}$. On the left is plotted the discovery for 3σ and on the right for 5σ as function of mean number of event signal $\langle N \rangle$. Geometry [95] with distances between DU = 180m and bar length = 6m. The experimental points are fitted by a cumulative gaussian distribution (dashed lines).

for two years of data taking at 5σ of power. The minima discovery fluxes for one year of data taking compared to a geometry with a distance between the detection units of 130 m, are are reported in table 6.5. From these values we find that for RXJ1713 the best configuration for the detector is that with a mean distance from the detection unit equal to 130 m. This is true both for binned and unbinned analysis.

6.2 The Fermi Bubbles analysed with the ANTARES telescope

The detection of two giant gamma ray structures with sharp edges appearing below and above the Galactic center has recently been reported from an analysis of the Fermi-LAT data [45] . These giant bubbles show no significant spatial nor intensity variation. Moreover, an unusually hard energy spectrum, consistent with E^{-2} has been measured. The origin of these giant bubbles is still not clear, however if their origin is related to a population of cosmic rays protons, a production of cosmic neutrinos could be attended as a consequence of the interaction of cosmic rays with inter-stellar matter [48].
An energy The present section describes an analysis that has been performed for the ANTARES detector over a data set and Monte Carlo

5σ	Φ_{binned}	$\Phi_{unbinned}$
1 year	$1.27 \cdot 10^{-13}$	$7.6 \cdot 10^{-14}$
2 years	$8.2 \cdot 10^{-14}$	$4.4 \cdot 10^{-14}$
3σ	Φ_{binned}	$\Phi_{unbinned}$
1 year	$6.7 \cdot 10^{-14}$	$4.0 \cdot 10^{-14}$
2 years	$4.4 \cdot 10^{-14}$	$2.4 \cdot 10^{-14}$

Table 6.4: Discovery flux at 50% CL for RXJ1713 with an energy spectrum $16.8^{-15} E^{-1.72} exp(-\sqrt{E/2.1TeV}) GeV^{-1} cm^{-2} s^{-1} sr^{-1}$. Fluxes are in unit of $[GeV^{-1} cm^{-2} s^{-1} sr^{-1}]$ for a geometry with a distance between the detection unit of 180 m.

$\delta = -40°$	$\Phi^{\gamma=1.72}_{binned}$	$\Phi^{\gamma=1.72}_{unbinned}$
Geometry 1	$1.27 \cdot 10^{-13}$	$7.6 \cdot 10^{-14}$
Geometry 2	$9.8 \cdot 10^{-14}$	$4.5 \cdot 10^{-14}$

Table 6.5: Discovery Flux at 50%CL for 1 year of data taking for the studied geometries. Fluxes are in unit of $[GeV^{-1} cm^{-2} s^{-1}]$.

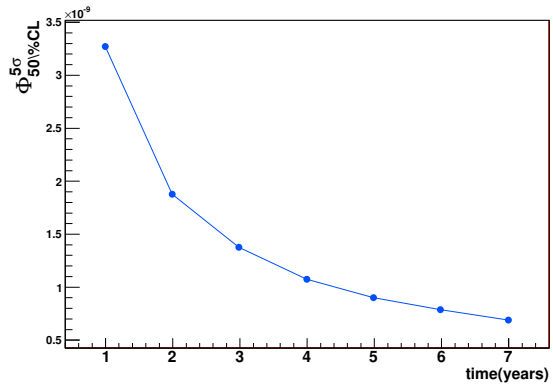

Figure 6.10: Discovery flux at 50%CL for a point-like source using the geometry 1 as function of number of data taking.

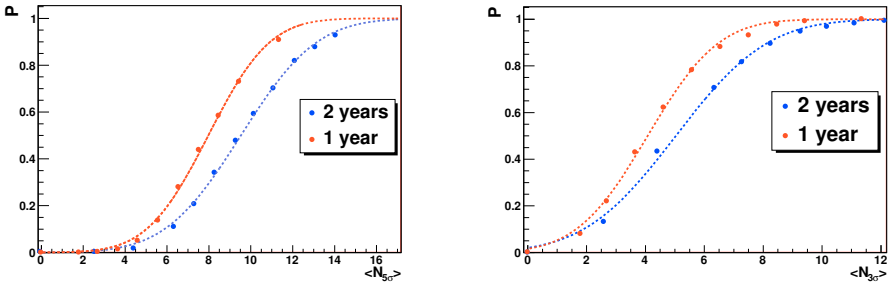

(a) 5σ (b) 3σ

Figure 6.11: Discovery power for RXJ1713 and an energy spectrum 5.13,for 1 and 2 years of data taking at 3σ and 5σ as function of mean number of event signal ⟨N⟩. Geometry [95] with distances between DU = 180m and bar length = 6m.

sample corresponding to about one month of lifetime. The aim of this analysis of a reduced data set was to optimize the strategy and selection criteria to search for neutrinos from Fermi bubbles in order to request an unblinding of data.

6.2.1 Selection of Runs

In order to build a Monte Carlo sample that can be as much as possible compatible with data, runs are selected as follows.
Each run in ANTARES is classified by a *Quality Basic* (or QB) flag introduced mainly to perform a first selection of the non-pathological

runs that can be used for the analysis. It essentially concerns low-level data quality (DQ) criteria. It can have the following values with reconstruction quality:

QB = 1 basic selection, minimum requirement for a run to be included in the analysis.

QB = 2 at least 80% of the OMs expected to work at the time of the run are effectively working

QB = 3 Baseline < 120 kHz and Burst Fraction < 40%

QB = 4 Baseline < 120 kHz and Burst Fraction < 20%

The "baseline" is the mean distribution of rate in each PMT for full run collected (kHz). Each distribution is fitted with a gaussian function and then its mean value averaged for all PMTs is set as baseline.
For each PMT the percent of time slices, with rate higher than the mean value of a gaussian distribution + 20%, is calculated; this value averaged for all PMTs is the *Burst Fraction*.
We have calculated for the whole ANTARES production 2008-2011 the percentage of each QB in order to report this same percentage on our sample. Apart from this, the choice of runs to form our sample has been totally random in the selected period 2008-2010. Simulated events have been generated according to the "Run-by-Run method" , consisting in reproducing for each run, realistic conditions of optical background and detector configuration and detector settings [104]. The final sample of runs consists of 269 Run-by-Run MC-data runs with a lifetime of 25 days ($\sim$ 0.069 years). The events are reconstructed via Aart strategy (AAfit) [87].
The particles simulated are the following:

- **Atmospheric neutrinos** The atmospheric neutrinos were simulated with GENHEN (see section 4.2) and weighted with a Bartol flux [88] in an energy range from 10 to 10^7 GeV.

- **Atmospheric muons** Muons are simulated with MUPAGE package (see section 4.3). The MUPAGE events do not have any weight, because the livetime is computed directly by the software. In this case for each muon track is assigned a weight equal to 10.

- **Neutrinos from the bubbles** Are weighted with an energy spectrum E^{-2} [48] on the Fermi-Bubbles region of the sky.

6.2.2 Data-MonteCarlo comparison

The atmospheric muon rejection is an important requirement of the analysis.
There are two steps of selection; a first level cut to reject the majority of downgoing muon events and a second level cut to select events classified as upgoing with very high confidence. The Aart algorithm

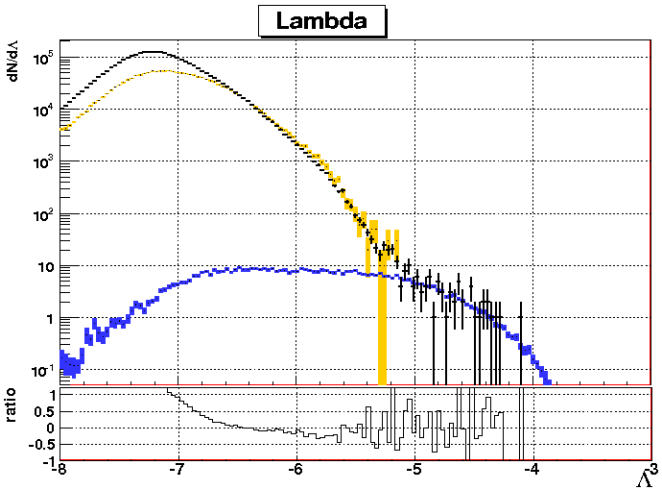

Figure 6.12: Upper panel: Λ distribution for up-going tracks reconstructed by AAFit strategy for the sample chosen for data (black), atmospheric muons (yellow) and atmospheric neutrinos (blue). Lower panel: $(Data-MC)/MC$ ratio.

has been optimized to give a good angular resolution by cutting in the Λ variable (see equation 4.18). Four simple conditions define the first level of cuts. We take all the events that have:

- $\theta_{rec} \leqslant 90°$ The zenith angle of the reconstructed event must be upgoing between 0° and 90°.
- $\Lambda > -6$ Tracks reconstructed with a very bad quality parameter are rejected.

- $L_{prefit} > 1$ where L_{prefit} is the number of detector lines used in the linear prefit. The vertical tracks reconstructed with only one line suffer from geometrical problems [105]

- $Nhit > 60$ is the number of hits selected in the last step of the reconstruction algorithm. These hits have time residuals between -250 and +250 ns. This selection ensures the rejection of low energy events.

In figure 6.12 the distribution of Λ for data and Monte Carlo for the chosen sample of runs looking at only up-going tracks reconstructed is shown.

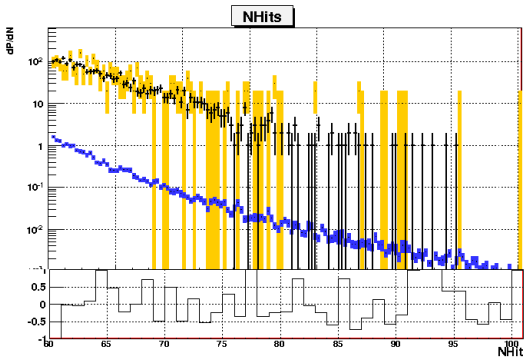

Figure 6.13: Upper panel:Distribution of the number of hits for the sample with the first level cuts applied (see text) for data (black), atmospheric muons (yellow) and atmospheric neutrinos (blue). Lower panel: $(Data-MC)/MC$ ratio.

In the lower panel of figure 6.12 the $(Data - MC/MC)$ ratio as function on Λ is plotted. A good agreement data-MC will arrange the $(Data-MC/MC)$ ratio in proximity to zero while in the Λ distribution without cuts, it seems to have big fluctuations. When we apply the first level cut, the according data-MC becomes better, this is shown in the distribution of the number of hits *NHits* in figure 6.13 and in that of the angular error of the reconstruction fit in figure 6.14.
As shown in these two plots, the first level cuts seem to reduce the discrepancy between data and Monte Carlo, but an higher level of cut could be applied to select better the good reconstructed tracks. We can obtain this by a selection on the tracks reconstructed that have an angular error of fit lower than 1°. In order to select the region in the sky

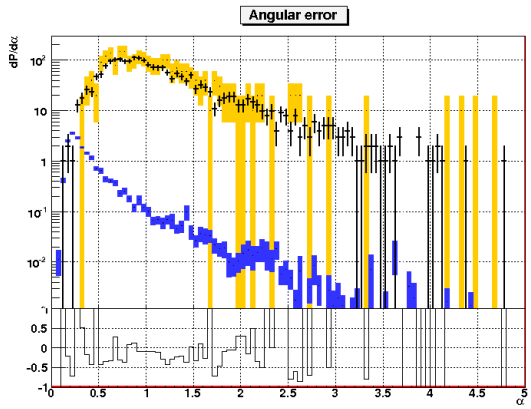

Figure 6.14: Upper panel: Distribution of angular error for the sample with the first level cuts applied (see text)for data (black), atmospheric muons (yellow) and atmospheric neutrinos (blue). Lower panel: $(\mathrm{Data} - \mathrm{MC})/\mathrm{MC}$ ratio.

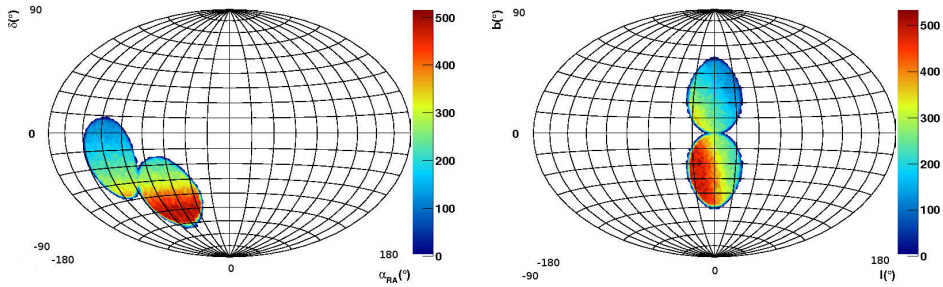

(a) *Equatorial coordinates* (b) *Galactic coordinates*

Figure 6.15: Visibility of ANTARES for the two Bubbles. A geometrical cut was applied at data sample with a first level cut.

occupied by the Fermi Bubbles[2] we do a last cut on galactic latitude and galactic longitude of the tracks. The acceptance of ANTARES to the two Fermi-Bubbles is shown in figures 6.15 both in equatorial and galactic coordinates for the data-sample at the only first level cut.
In galactic coordinates the source, as shown in figure 6.15b, has one bubble that lies only on the northern hemisphere (b>0°) and another that lies only on the southern (b<0°). Moreover, ANTARES is more sensitive to the southern hemisphere and hence to the south bubble (figure 6.15b).

[2]The galactic coordinates can be found in reference [45]. These two regions can be fitted by circles of radius 25° with $b = \pm 25°$.

	$\theta_{rec} \leqslant 90°$ and $\Lambda > -8$	First Level Cuts	First Level Cuts + angular error<1°	First Level Cuts + angular error<1° + Cut on Bubbles
DATA	$2.95 \cdot 10^6$	2072	1078	90
MC μ_{atmo}	$2.49 \cdot 10^6$	2480	1250	180
MC ν_{atmo}	$4.42 \cdot 10^2$	18.77	17.65	2.22
MC signal $\nu_{sig}^{E^{-2}}$	–	2.95	2.80	0.31
(DATA-MC)/MC	0.18	-0.17	-0.15	-0.51

Table 6.6: Ratio data-Mc for various cuts for the total run duration of the sample of 0.069 years.

Λ	Nhit	n_{sig}^{E-2}	n_{bkg}	MRF	$\Phi[GeVcm^{-2}s^{-1}]$
-5.7	86	1.84	3.94	2.06	$2.06 \cdot 10^{-7}$

Table 6.7: Sensitivity and MRF minimum computed for 1 year with 90%CL for the ANTARES detector to the Fermi Bubbles

Data-MC ratio as function of different level cuts is shown on table 6.6. The data-MC ratio becomes better when the first level set of cuts is applied as shown also in distribution of the number of hits and of angular error. However the last cut on galactic longitude and latitude has a worse ratio data-MC (see table 6.6). This can be due to statistical uncertainties due to the very low lifetime of the sample and for this reason is not so dramatically to begin with a first exploration of the performances of the ANTARES telescope to the bubbles in order to improve the statistic for an higher step of analysis in the next months.

6.2.3 Results

With the monthly-like sample we have calculated an upper limit on sensitivity and a discovery potential flux for ANTARES detector, performing a binned analysis.

Unlike the binned analysis applied for point-like sources in KM3NeT detector,we don't optimize the opening angle of a cone centred on the source because the source extension is too large and we treat it more likely to a diffuse flux. We have optimised the quality parameter Λ and NHit on varying the number of years of data taking. A calculation

years	Λ	Nhit	n_{sig}^{E-2}	n_{bkg}	MRF	$\Phi[GeVcm^{-2}s^{-1}]$
1	-5.7	86	1.84	3.94	10.7	$1.0 \cdot 10^{-6}$
1.5	-5.7	100	3.07	3.59	6.15	$6.15 \cdot 10^{-7}$
2	-5.7	102	5.23	5.88	4.26	$4.26 \cdot 10^{-7}$
2.5	-5.7	100	8.53	9.97	3.19	$3.19 \cdot 10^{-7}$
3	-5.7	101	12.05	14.02	2.57	$2.57 \cdot 10^{-7}$
6.8	-5.9	131	36.01	19.62	0.98	$9.8 \cdot 10^{-8}$

Table 6.8: Discovery potential flux minimum at 90%CL and 5σ as function of years of data taking for the ANTARES detector to the Fermi Bubbles. For a $\Phi_0 = 10^{-7} GeVcm^{-2}s^{-1}$ the discovery is at 6.8 years of data taking.

years	Λ	Nhit	n_{sig}^{E-2}	n_{bkg}	MRF	$\Phi[GeVcm^{-2}s^{-1}]$
1	-5.6	96	1.45	2.03	7.33	$7.33 \cdot 10^{-7}$
2	-5.7	102	5.23	5.88	3.02	$3.02 \cdot 10^{-7}$
3	-5.7	101	12.05	14.02	1.88	$1.88 \cdot 10^{-7}$
4	-5.7	130	12.53	6.84	1.34	$1.34 \cdot 10^{-7}$
5	-5.7	131	19.47	10.61	1.03	$1.03 \cdot 10^{-7}$
5.5	-5.7	128	24.54	14.03	0.92	$9.2 \cdot 10^{-8}$

Table 6.9: Discovery potential flux minimum at 50%CL and 5σ as function of years of data taking for the ANTARES detector to the Fermi Bubbles. For a $\Phi_0 = 10^{-7} GeVcm^{-2}s^{-1}$ the discovery is at 5.5 years of data taking.

on discovery potential flux at 90%CL and 50%CL at 5σ is reported in tables 6.8 and 6.9 while the sensitivity for one year of lifetime is shown in table 6.7. For an expected flux of $E^{-2} \cdot 10^{-7} GeVcm^{-2}s^{-1}$ [48] the years for discovery for ANTARES detector are of 6.8 years of lifetime at 90%CL and 5.5 years at 50%CL with 5σ of power.

6.2.4 Unbinned calculations

A preliminary analysis with an unbinned method, performed only on Monte Carlo events and not on data, will be presented.
We build 10000 MC samples starting from the monthly-like sample used in the binnned analysis with the following cuts :

- $\theta_{rec} \leqslant 90°$

- $\alpha \leqslant 1^\circ$ is the angular error of the fit algorithm
- $L_{prefit} > 1$
- $Nhit > 60$
- $\Lambda > -5.3$: with this choice we have removed all the atmospheric muons from our sample

With these cuts, for each MC sample we have an amount of ~ 200 neutrino and antineutrino events per year. The same choice of cuts is done for the selection of signal events, weighted with an energy spectrum E^{-2}. So for one year of data taking we expect a mean number of signal events from the two bubbles with a model flux $E^{-2} \cdot 10^{-7} GeV\, cm^{-2} s^{-1}$ of about 4.53.
Then we put in each pseudo-experiment sample the reconstructed galactic latitude and longitude. We divide the sky into two regions: the northern hemisphere and the southern hemisphere. Each of these hemispheres can incorporate at least only one of the two bubbles[3]. So we have two background PDFs; one for the northern hemisphere as function of angular distance from the centre of northern bubble and another for the southern hemisphere as function of angular distance from the centre of southern bubble. The two PDFs of signal as function of angular distance from the centre of the bubble are almost the same for north and south sky, except for their integral due to the ANTARES visibility of the sky ($\sim$ 22% of events from north bubble and $\sim$ 77% from the south bubble). PDFs for background are shown in figure 6.16a, while PDF of signal for the south bubble is shown in 6.16b.
Then we apply the algorithm described in section 5.3.2 and we try to maximize the likelihood ratio value. The likelihood ratio for the only background case and its integration are shown on figures 6.17. For the *bubbles-search*, LR for the only-backgrounf hypothesis has lower counting at zero in confront with that of point-like sources (see figure 6.3). This is due to the shapes of the PDFs for signal and background that have a similar behaviour for angular distances below 25°; hence the unbinned algorithm (in the only-background case) maximize LR for more non-null values of n_{sig} (see equation 5.16) than the case of the

[3]With this hypothesis the northern hemisphere cannot incorporate signal events of the southern bubble

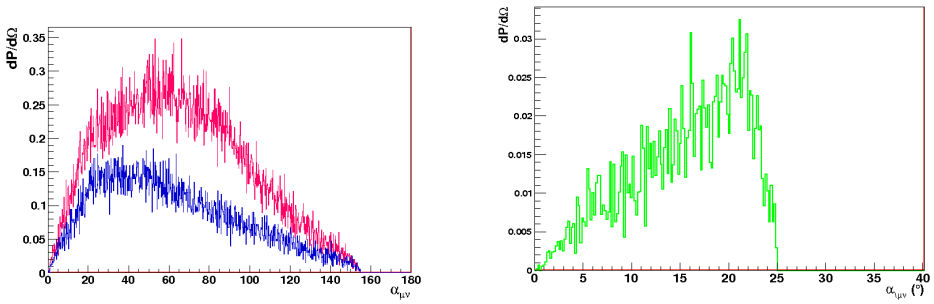

(a) *background PDFs* (b) *signal PDF of the south bubble*

Figure 6.16: a: PDFs of background of the northern sky hemisphere (blue) as function of angular distance from the centre of northern bubble (l,b)=(0°,25°) and of background of the southern sky hemisphere (magenta) as function of angular distance from the centre of southern bubble (l,b)=(0°,−25°). b: PDF of signal from the southern bubble as function of angular distance from the centre of the bubble. Histograms are all normalized to the attended value of signal and background in 1 year for the chosen cuts.

Fermi-Bubbles	Φ_{binned}	Φ_{unbinned}
5σ 50%CL	$7.33 \cdot 10^{-7}$	$3.25 \cdot 10^{-7}$

Table 6.10: Discovery flux for the Fermi-Bubbles for 1 year of data taking both for binned and unbinned methods. Fluxes are in unit of $[\text{GeV cm}^{-2}\text{s}^{-1}]$.

point-like source.
Adding at the samples a certain number of events from the two bubbles in a random way, LR becomes more positive as shown in figure 6.18. We calculate the critical values of LR ($5\sigma = 8$ in this case), as explained in detail in sections 6.1.1-6.1.2 and then the mean number of events for the discovery, plotted in figure 6.19 as function of the discovery probability at 5σ.
For one year of data taking 16 signal events of excess are needed to have the discovery at 50%CL. From the comparison binned-unbinned for the discovery flux in table 6.10 merges a gain of about 50% with the unbinned analysis. This will reduce the amount of year for the discovery of the two bubbles. However this is only a first preliminary calculation and subsequent investigations should be carried out.

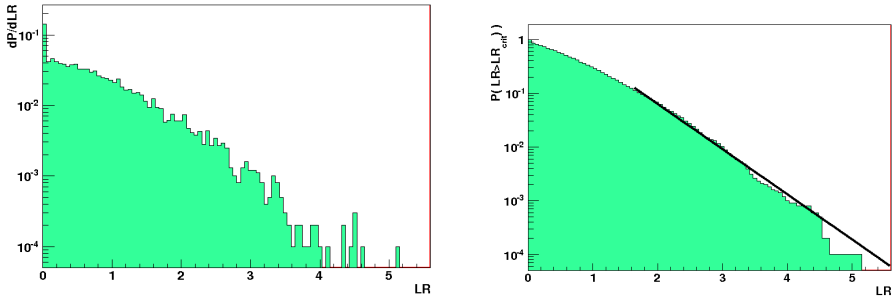

(a) *LR for the only-background case* (b) *Integrated LR for the only-background case*

Figure 6.17: a: Likelihood ratio for the only-background case for the Fermi-Bubbles source. b: Integrated likelihood ratio.

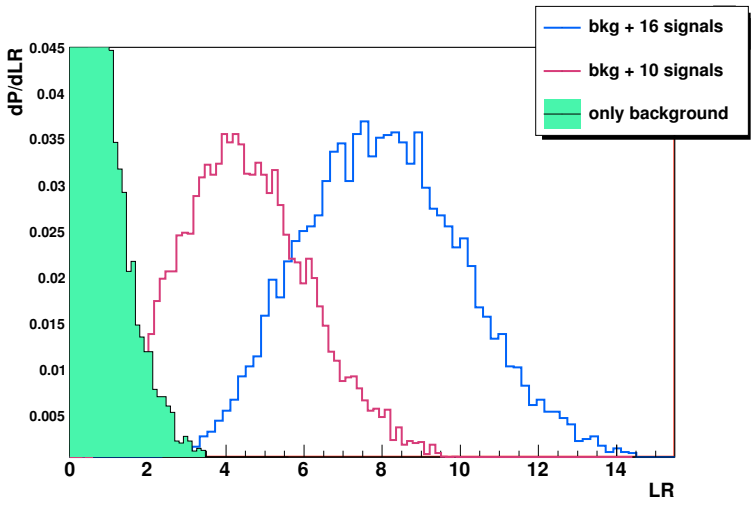

Figure 6.18: Likelihood ratio for the only-background case (green area) and for background + 10 (magenta) and 16 (blue) signal events from the Fermi-Bubbles.

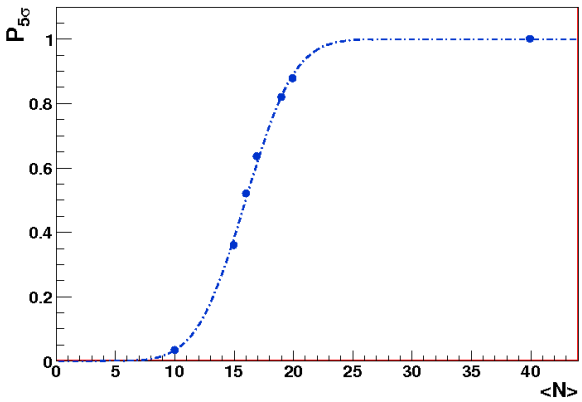

Figure 6.19: Mean number of events for the discovery at 5σ of the two Fermi-Bubbles for 1 year of data taking of the ANTARES telescope. The dashed line is a fit of the experimental points found from analysis with a cumulative gaussian.

Chapter 7

Conclusions

Neutrino astronomy is a very young branch of astroparticle physics. More generally, at very high energies, astronomy with photons becomes useless because they are absorbed on the low energy photons from the cosmic background radiation. This limits the path length of a 10 TeV photon, for example, to roughly the distance of the nearest active galaxy. In contrast, neutrinos offer a means to study the universe at very high energies or large distances. Very high energy gamma-ray sources are good candidate as neutrino sources if their emissions are originated from an hadronic-model decay; on the contrary a purely leptonic processes will not have any neutrino emission.
The main goal of this thesis is the comparison of results in terms of discovery potential flux from different statistical methods applied to the search of point-like and extended sources with the KM3NeT telescope which will be build in the Mediterranean Sea with the efforts of an international collaboration [3] and with the ANTARES telescope located at a depth of 2475 m in the South of France.
In the analysis with the ANTARES telescope we have the real data and the Monte Carlo simulation so a comparison data-Monte Carlo has been done before the analysis. In order to detect very small number of events from cosmic sources amongst large backgrounds, statistical methods are needed. The two main methods used are the binned and unbinned methods.
Binned methods are easy to implement and computationally fast. The binned method is based on the minimization of the Model Discovery Potential, related to the background-signal ratio, on a search-cone

centred on the source and on two quality parameter of reconstruction algorithm, the likelihood of the fit Λ and the number of hits of the fit *NHits* related to the muon energy.
The unbinned algorithm is more complex and slow. It is based on the maximization of a test statistic called *likelihood ratio* (LR). The likelihood ratio is a function of measured variables that permits to investigate the measure of agreement between the observed data and two given hypothesis: the presence of only background and the presence of background plus a source of events.
These two methods have been applied for the KM3NeT detector for two sources. The first was a generic point-like source with an energy spectrum

$$10^{-7}E^{-2}GeVcm^{-2}s^{-1}sr^{-1}$$

and the second source was the SNR RXJ1713.3946 with an energy spectrum

$$16.8 \cdot 10^{-15}E^{-1.72}exp(-\sqrt{E/2.1TeV})GeV^{-1}cm^{-2}s^{-1}sr^{-1}$$

. The results for both the two sources show a decreasing on discovery potential flux when we pass from binned to the unbinned method both for 3σ and 5σ of power.
For the point like source and a geometry of 154 detection units with a mean distance between each unit of 180m this decreasing for 2 years of data taking is of 17% , while for the RXJ1713 the gain is of 46% for one year and of 40% for 2 years of data taking at a power of 5σ. For the source RXJ1713 we have also analysed a second geometry with a mean distance between the units of 130m. Results for this geometry show a decreasing on discovery potential flux both on binned and unbinned methods for one year of data taking in confront to the previous detector geometry chosen. An gain on discovery flux of about 40% will reduce in a consistent way the number of years for the discovery of the RXJ1713 that with binned methods is at best of about $5 \div 6$ years.
During a period of stage with the ANTARES group of CPPM in Marseille, we have estimated the sensitivity and the discovery potential for the ANTARES detector for the Fermi Bubbles. After a data-Monte Carlo comparison we have selected a certain number of runs of the ANTARES production 2008-2010 in order to reproduce a sample of runs with a lifetime of about one month. We have used this sample

of runs to calculate with binned and a preliminary analysis unbinned, the discovery potential fluxes. Binned results show that we can reach the discovery at 5σ and 50% of CL for the two bubbles in the hypothesis that their neutrino energy spectrum is $E^{-2} \cdot 10^{-7} GeV cm^{-2} s^{-1}$ with about 5.5 years of data taking. In addition the preliminary unbinned analysis has shown a decreasing very high on discovery flux in confront to the binned method. This analysis has been done in order to request an unblinding of ANTARES data as soon as possible and needs of further checks.

Bibliography

[1] IceCube web-page http://icecube.wisc.edu

[2] ANTARES web-page http://antares.in2p3.fr/

[3] KM3NeT web-page http://www.km3net.org/KM3NeT-TDR.pdf

[4] G. Aggouras et al., Nucl.Phys., B(Proc. Suppl.)151(2006)279.

[5] T. K. Gaisser, Cosmic rays and particle physics., Cambridge, UK Univ. Pr. ,(1990).

[6] M. Nagano and A. A. Watson, Observations and implications of the ultrahigh-energy cosmic rays, *Rev. Mod. Phys.* ,72, 689 (2000).

[7] V.F. Hess. *Phys. Zeit.*, 13-1084, (1912).

[8] E. Fermi, On the origin of cosmic rays., Phys. Rev., 75-1169, (1949).

[9] E. Fermi, Galactic magnetic fields and the origin of cosmic radiation, *Astroph. J.*, 119:1, (1954).

[10] J.R. Horandel, Models of the knee in the energy spectrum of cosmic rays, *Astrop. Phys.*, 21:241-265, (2004).

[11] A.M. Hillas, *Ann. Rev. Astron. Astrophys.*, 22:425, 1984.

[12] G.T. Zatsepin and V.A. Kuzmin,. *JETP Lett.*, 4:78, 1966.

[13] The HIRES collaboration, *Phys. Rev. Lett.*, 100:101101, 2008.

[14] J. Abraham for the Auger coll, Phys. Rev. Lett., 101:06110, 2008.

[15] M. Takeda et al., Phys. Rev. Lett., 81:1163, 1998.

[16] R. J. Protheroe, Origin and propagation of the highest energy cosmic rays (1996), astro-ph/9612212.

[17] J. G. Learned and K. Mannheim, High-energy neutrino astrophysics. Ann. Rev. Nucl. Part. Sci. 50, 679 (2000).

[18] J. N. Bahcall and E. Waxman, High energy astrophysical neutrinos: The upper bound is robust. *Phys. Rev. D*, 64:023002, 2001.

[19] C. E. Fichtel and J. I. Trombka. *Gamma-ray astrophysics: New insight into the Universe. Technical report*, 1997. NASA-RP-1386.

[20] Villante F.L.,and Vissani F., Phys. Rev., D78-10 (2008) 103007.

[21] Morlino G., Blasi P. and Amato E., ApP, 31-5 (2009) 376.

[22] Berezhko E.G.,and Volk H.J., A & A, 492-3 (2008) 695;

[23] T. C. Weekes et al. , Observation of TeV gamma rays from the Crab nebula using the atmospheric cerenkov imaging technique. *Astrophys. J.*, 342:379-395, 1989.

[24] R. Mirzoyan et al., The first telescope of the HEGRA air cherenkov imaging telescope array., *Nucl. Instr. and Meth. Phys. Res. A*, 351:51-526, 1994.

[25] HESS web-page `http://www.mpi-hd.mpg.de/hfm/hess/`.

[26] M. P. for the HESS Collaboration, Results from observations of agns with the hess telescope system and future plans, arXiv:astro-ph/0501155v1.

[27] P. f. t. F.-L. C. Saz Parkinson, Fermi: Gamma-ray space telescope observations of gamma-ray pulsars, arXiv:0901.3405v1.

[28] J. Knodlseder, Studies of gamma ray sources with the fermi large area telescope, (2010), arXiv:1006.2635v1

[29] R. Enomoto et al. Design study of CANGAROO-III, stereoscopic imaging atmospheric Cherenkov telescopes for sub-TeV gamma-ray. Astrop. Phys., 16:235-244, 2002.

[30] F. Piron (CAT coll.). Observation of the gamma-Ray Emission Above 250 GeV from the Blazars Markarian 501 and Markarian 421 by the CAT Cherenkov Atmospheric Imaging Telescope. *In Proceedings of the XIth rencontres de Blois*, 1999.

[31] T.C. Weekes et al. VERITAS: the Very Energetic Radiation Imaging Telescope Array System. *Astrop. Phys.*, 17:221-243, 2002.

[32] Aharonian. F. and al., Nature, 432 (2004) **75**;

[33] Tibolla O. for the HESS Collaboration., *Proceedings of the 31th Int. Conf. on Cosmic Rays, Lodz - Poland 2009*, `arXiv:0907.0574v1` ;

[34] Aharonian. F. and al.,*Rep. Prog. Phys.*,**71** (2008) 096901.

[35] Meszaros P.,*Rep. Prog. Phys.*,69 (2006), 2259.

[36] Hjorth J. and al., Nature, 423-6942 (2003) 847;

[37] Meszaros P., *Nature*, 423-6942 (2003) 809;

[38] Sakamoto T. and al., *The Astrophysical Journal Supplement*, **175** (2009) 179 ;

[39] T. Piran. Gamma-Ray Bursts and the Fireball Model. *Phys. Rept.*, 314:575- 667, 1999, `astro-ph/9810256`.

[40] A. Kappes, J. Hinton, C. Stegmann, and F. A. Aharonian. Potential Neutrino Signals from Galactic Gamma-Ray Sources. *Astrophys. J.*, 656:870-896, 2007, `astro-ph/0607286`.

[41] F. Aharonian et al. (HESS coll.). Very high energy gamma rays from the direction of Sagittarius A . *Astron. and Astroph.*, **425(L13)**, 2004.

[42] Pfeffermann, E. , Aschenbach, B. (1996), in Roentgenstrahlung from the Universe, 267-268

[43] Koyama, K., et al. 1997, PASJ, 49, L7

[44] Slane P, Gaensler B M, Dame T M, Hughes J P, Plucinsky P P and Green A 1999 Astrophys. J. 525 357

[45] Meng Su, Tracy R. Slatyer, Douglas P. Finkbeiner *GIANT GAMMA-RAY BUBBLES FROM Fermi -LAT: AGN ACTIVITY OR BIPOLAR GALACTIC WIND?* arXiv:1005.5480v3

[46] Fermi-Bubbles web-page http://www.nasa.gov/mission_pages/GLAST/news/new-structure.html

[47] NASA-Fermi-Telescope web-page http://fermi.gsfc.nasa.gov/ssc/data/

[48] M. Crocker and F.Aharonian . The Fermi Bubbles: Giant, Multi-Billion-Year-Old Reservoirs of Galactic Center Cosmic Rays *Phys. Rev. Lett*. **106** (2011) 101102.

[49] Snowden, S. L., et al. 1997, Astrophysics Journal, 485, 125

[50] Finkbeiner, D. P. 2004a, Astrophys. J., 614, 186-. 2004b

[51] Aharonian, F., et al. 2009, A& A, 508, 561.

[52] Haslam, C. G. T., Salter, C. J., Stoffel, H., Wilson, W. E. 1982, A& AS, 47, 1

[53] B. Kayser. Neutrino Oscillation Phenomenology. 2008, arXiv:0804.1121.

[54] J. N. Bahcall. Neutrino Astrophysics. Cambridge University Press, Cambridge, U.K., 1989.

[55] B. T. Cleveland et al ., Measurement of the solar electron neutrino flux with the Homestake chlorine detector. *Astrophys. J.*, 496:505-526, 1998.

[56] Q. R. Ahamad et al . Direct evidence for neutrino flavor transformation from neutral-current interactions in the Sudbury Neutrino Observatory. *Phys. Rev. Lett.*, 89:011301, 2002, nucl-ex/0204008.

[57] Y. Fukuda et al . Evidence for oscillation of atmospheric neutrinos. *Phys. Rev. Lett.*, 81:1562-1567, 1998, hep-ex/9807003.

[58] J. Hosaka et al., *Phys. Rev.* D73, 112001 (2006).

[59] A.M. Markov. *In Proceeding of the Rochester Conference*, New York, 1960.

[60] P.S. Auchincloss et al., *Z. Phys.* C48, 411 (1990);

[61] P. Berge et al., *Z. Phys.* C35, 443 (1987);

[62] M.H. Reno, R. Gandhi, C. Quigg, and I. Sarcevic.*Phys. Rev. D*,58:093009, 1998.

[63] R. Gandhi et al., Astropart. Phys. 5, 81 (1996).

[64] Roberts A. et al., *Rev Mod. Phys.*, 64 (1992) 259.

[65] Wischnewski R. for the BAIKAL collaboration, *Int. J. Mod. Phys. A*,20 (2005).

[66] Andres E. et al., *Astropart. Phys.* 13 (2000) 1.

[67] Migneco E. et al.,Nucl Instrum Methods A, 588 (2008) 111.

[68] A. Capone et al . Recent results and perspectives of the NEMO project. N.I.M. A, 602:47-53, 2009.

[69] J. Vandenbroucke, G. Gratta, and N. Lehtinen. Experimental study of acoustic ultra-high-energy neutrino detection. Astrophys. J., 621:301-312, 2005, `astro-ph/0406105`.

[70] I. Kravchenko et al. E*vent Reconstruction and Data Acquisition for the RICE Experiment at the South Pole*. 2007, `arXiv:0705.4491`.

[71] J. Bluemer for the Pierre Auger Collaboration. *The Pierre Auger Observatory: Results on Ultra-High Energy Cosmic Rays*. 2008, `arXiv:0807.4871`.

[72] NEMO collaboration. (2002) `http://nemoweb.lns.infn.it/upload/file/Nemo%20publication/2003/NEMO-Site-Report.pdf`

[73] G. Riccobene et al., *Astroparticle Physics*, 27(2007)1.

[74] A. Capone et al., *Nucl. Instr. Meth.*, A487(2002)423.

[75] M. Ardid et al., *Nucl.Instr. and Meth.*, A602(2009)174.

[76] E. Migneco et al., *Nucl. Instr. and Meth.*, A508(2008)111.

[77] P. Amram et al. (ANTARES coll.). "The ANTARES optical module." Nucl. Instr. and Meth. A, 484:369, 2002.

[78] F. Cassol, `ANTARES-Software/2000-008` (2000).

[79] CORSIKA code web-page `http://www-ik.fzk.de/corsika/`.

[80] Y.Becherini et al., Astropart. Phys. 25,1 (2006).

[81] D. Bailey, `ANTARES-Software/2002-004` (2002).

[82] G. Ingelman, A.Edin, J. Rathsman. *Comput. Phys. Commun.* 101 (1997) 108-134. `http://www3.tsl.uu.se/thep/lepto`.

[83] A. Margiotta. Simulation of muons from atmospheric showers in the ANTARES detector using HEMAS. ANTARES Internal note, 2004. `ANTARES-Soft/2004- 002`.

[84] G. Barr "The separation of signal and background in a nucleon decay experiment", Ph.D. thesis, Keble Collede, University of Oxford (1987).

[85] S.Navas, L. Thompson `ANTARES-Software/1999-011` (1999).

[86] J. Brunner "Geasim: User manual" `http://antares.in2p3.fr/internal/software/geasim.html`

[87] A. Heijboer. "Track Reconstruction and Point Source Searches with ANTARES" PhD thesis, NIKHEF, Amsterdam, 2004.

[88] G.D. Barr, T.K. Gaisser, P. Lipari, S. Robbins, and T. Stanev. *Phys. Rev. D*, 70:023006, 2004.

[89] M. Honda et al. *Phys. Rev. D*, 52:4985-5005, 1995.

[90] FLUKA code web-page `http://www.fluka.org/fluka.php`.

[91] G. Battistoni, A. Ferrari , T. Montaruli , P.R. Sala "The FLUKA atmospheric neutrino flux calculation" (2003)

[92] GEANT web-page `http://wwwasd.web.cern.ch/wwwasd/geant/`.

[93] S. Navas, ANTARES-Software/1999-002 (1999).

[94] P. Antonioli et al. A three-dimensional code for muon propagation through the rock: MUSIC. *Astrop. Phys.*, 7:357, 1997.

[95] Work Package D,*Detector simulations for KM3NeT*, http://www.km3net.org/internal.php

[96] G. Feldman & R. Cousins, *Phys. Rev.* **D57** (1998) 3873.

[97] G.C. Hill & K. Rawlins, *Astrop. Phys.*, 19,393 (2003).

[98] S.R. Kelner, F.A. Aharonian and V.V. Bugayev *Phys. Rev* D 74, 034018 (2006)

[99] The High Resolution Fly's Eye Collaboration and G. R. Farrar. "Search for point sources of ultra-high energy cosmic rays above 40 EeV using a maximum likelihood ratio test." *Astrophys. J.*, 623:164, 2005. astro-ph/0412617.

[100] S. S. Wilk "The Large-Sample Distribution of the Likelihood Ratio for Testing Composite Hypotheses". *The Annals of Mathematical Statistics 9*, 60-62 (1938).

[101] SLALIB-Positional Astronomy Library http://www.starlink.rl.ac.uk/star/docs/sun67.htx/sun67.html

[102] Jerzy Neyman, Egon Pearson "On the Problem of the Most Efficient Tests of Statistical Hypotheses". *Philosophical Transactions of the Royal Society of London. Series A,* 289-337 (1933).

[103] J.A Aguilar. "Analysis of the Optical Beacon system and search for point-like sources in the ANTARES neutrino telescope" PhD thesis, IFIC, Valencia, 2008.

[104] Run-by-Run Method web-page http://antares.in2p3.fr/internal/dokuwiki/doku.php?id=run%20by%20run

[105] N. Cottini and T. Stolarczyk. Atmospheric neutrinos with 5 lines.ANTARES-PHYS-2008-003.